

Development of a Steam Generating Dynamometer for Gas Powered Turboshaft Engines

by

Edward John Ognibene

B.E.M.E., SUNY at Stony Brook (1989)

M.S.M.E., Massachusetts Institute of Technology (1991)

Submitted to the Department of Mechanical
Engineering in partial fulfillment of the
requirements for the degree of

DOCTOR OF PHILOSOPHY

at the

MASSACHUSETTS INSTITUTE of TECHNOLOGY

May 1995

© Massachusetts Institute of Technology, 1995
All rights reserved


Signature of Author _____


Department of Mechanical Engineering
May 22, 1995

Certified by _____


Professor Joseph L. Smith, Jr.
Thesis Supervisor

Accepted by _____


Professor Ain A. Sonin
Chairman, Graduate Committee
Department of Mechanical Engineering

MASSACHUSETTS INSTITUTE
OF TECHNOLOGY

FEB 06 1997
~~MAY 22 1995~~

LIBRARIES

ARCHIVES

Development of a Steam Generating Dynamometer for Gas Powered Turboshaft Engines

by Edward John Ognibene

B.E.M.E., SUNY at Stony Brook (1989)
M.S.M.E., Massachusetts Institute of Technology (1991)

Submitted to the Department of Mechanical
Engineering in partial fulfillment of the
requirements for the degree of

DOCTOR OF PHILOSOPHY

Abstract

Many types of dynamometers are available that operate according to various physical principles, ranging from cavitation to incidence or shock. Some examples are, electric eddy-current generators, perforated disc evaporators, and Froude type water brakes. However, these machines generally suffer from low-power-density, short mechanical life, or a small performance envelope.

To overcome these problems a new type of hydraulic dynamometer has been developed that operates by generating an organized high-speed free-surface liquid flow that helically recirculates on the inside surface of a torus. The liquid is accelerated by a rotor to a speed at which shaft-power input is absorbed by primarily frictional dissipation in the liquid. Power absorption (P) is a function of both rotor speed (ω) and liquid level in the working compartment. As power is absorbed a portion of the recirculating liquid is vaporized. There is a large radial pressure gradient across the liquid sheet due to streamline curvature that confines boiling to a thin layer near the free surface. Furthermore, phase separation occurs, resulting in the evolution of a vapor core surrounded by a liquid sheet. This is a significant design advantage because nearly pure vapor can be vented (to atmosphere) by tapping into the core region. This minimizes feed-water requirements and eliminates the need for bulky support apparatus. These features result in a portable, high-power-density dynamometer, with a long-life and wide operational envelope.

A rigorous method is presented for the design of these new dynamometers based on a flow model, blading algorithm, numerical programs, and empirical data. The numerical programs are useful for predicting P as a function of ω and liquid level, investigating the effect of parameter variations, and making off-design performance estimates. Furthermore, scaling laws are presented that are useful for making rough performance extrapolations. For example, P scales with size (D) to the fifth power.

To substantiate predictions, a blade cascade experiment and a low-speed prototype were developed and tested. The results confirmed theories about the basic nature of the flow and verified the blading algorithm. Finally, control scenarios are presented that aid in the application of this new dynamometer.

Thesis Supervisor: Dr. Joseph L. Smith, Jr.
Title: Professor of Mechanical Engineering

For my family

Acknowledgments

I would like to thank many people for their support during my doctoral experience at MIT. First, I am particularly grateful to Professor Joseph Smith for his unending enthusiasm and motivation throughout my experience here. His extremely broad engineering knowledge base and keen physical intuition continues to astonish me, and I am very fortunate to have had the opportunity to work with him. I would also like to thank my other Thesis Committee members Professor A. Douglas Carmichael and Doctor Choon S. Tan for their invaluable advice, and encouragement, for which I am very grateful.

I would also like to thank the people in the graduate office, especially Leslie Regan, for helping to make my experience at MIT as pleasurable as possible. She was always very helpful, and often did much more than she was required to. The department is fortunate to have such a devoted and capable person. I am also very grateful to Lisa Desautels and Doris Elsemiller, in the Cryo Lab, for all their help and assistance.

There are many graduate students that I would like to thank, particularly Gregory Nellis, for his help with the data acquisition system, for reviewing this thesis, and for his comradery. I also want to thank Sankar Sunder, Bill Grassmyer, Hayong Yun, Hua Lang, Mac Whale, and Chris Malone, for their helpful inputs and support during those endless lab days. I would also like to thank Mike Demaree, and Bob Gertsen, for their technical support during the experimental phase of the project.

I also want to thank my family, particularly my mother and father, for all their help and support throughout my experience at MIT. Strong family ties make it easy to persevere, and help keep things in perspective. I am especially grateful to my wife, Donna, for her love, encouragement, and motivation to continue on. I realize and appreciate the sacrifices she made to make this thesis possible.

Finally, I wish to acknowledge the financial support of Textron-Lycoming, which funded a significant portion of this work. Specifically, I would like to thank John Twarog and Richard Lambert for their continued enthusiasm and interest in the project.

Table of Contents

Abstract.....	2
Dedication.....	3
Acknowledgments.....	4
Table of Contents.....	5
List of Figures.....	7
Nomenclature.....	9
1 Conceptualization of Recirculating Flow Steam Generating Dynamometer	
1.1 Background.....	10
1.2 New Dynamometer Concept.....	12
1.3 Resulting Advantages.....	16
1.4 Outline of Thesis.....	17
2 Investigation of Power Absorbing Mechanisms	
2.1 Overview.....	19
2.2 Hydraulic Jump Induced Dissipation.....	19
2.3 Shear Stress Induced Dissipation.....	29
3 Development of Dynamometer Flow Model	
3.1 Basic Flow Model.....	32
3.2 Power Balance Between Rotor Input and Recirculating Fluid.....	34
3.3 Friction Factor Prediction & the Effect of Streamline Curvature.....	36
4 Blade Generation Algorithms & Programs	
4.1 Overview.....	38
4.2 Base Curve Development.....	39
4.3 Inner Curve Development.....	43
5 Flow Visualization Experiment -- Linear Blade Cascades	
5.1 Objectives and Overview.....	46
5.2 Experimental Set-Up.....	46
5.3 Test Results.....	49
6 Dynamometer Code Development and Performance Simulation	
6.1 Overview of Numerical Program.....	53
6.2 Key Dimensionless Ratios & Performance Estimation.....	54
6.3 Parameter Variations & Sensitivity Analysis.....	57
7 Synthesis of a Dynamometer Design Algorithm	
7.1 Overview & the Design Starting Point.....	61
7.2 Blade Generation, Water Supply, and Steam Ventilation.....	64
7.3 Performance Map, Scaling, and Other Design Issues.....	67

8 Low-Speed Prototype -- Experimental Verification of Dynamometer Flow	
8.1 Objectives and Overview.....	71
8.2 Low-Speed Prototype Design and Performance Estimation.....	72
8.3 Experimental Set-Up & Test Procedures.....	75
8.4 Empirical Results.....	77
8.4.1 Verification of Basic Flow & Power Absorption.....	78
8.4.2 Radial Velocity Distribution, Flow Consistency, and Stability.....	83
8.5 Additional Remarks.....	88
9 Full-Scale Steam Generating Prototype Design.....	89
10 Fundamental Dynamics and Control Issues	
10.1 Overview.....	94
10.2 Dynamic Behavior of the Dynamometer.....	95
10.3 Key Dynamometer Parameters.....	97
10.4 Dynamometer Control Schemes and Engine Testing.....	98
11 Conclusions	
11.1 Summary of Results.....	100
11.2 Future Work.....	103
 References / Bibliography.....	 104
 Biographical Note.....	 105

APPENDICES

A Flow Visualization -- Procedures & Raw Data.....	106
B Rotor and Stator Blades	
B.1 Base Curve Generation (FORTRAN).....	110
B.2 Inner Curve Generation (Math Cad).....	115
C Flow Modeling	
C.1 Dynamometer Code (FORTRAN).....	123
C.2 Sample Run.....	134

List of Figures

1-1. Vapor-liquid stratification in torus.....	13
1-2. Toroidal geometry with rotor and stator blading.....	14
1-3. Channels formed by blades.....	15
2-1. Modeling a hydraulic jump in cylindrical coordinates.....	20
2-2. Jump Function (Number) dependence on flow ratio.....	23
2-3. [JEF] variation with flow ratio (r_1/R).....	26
2-4. Power dissipated by a hydraulic jump.....	29
2-5. Shear induced frictional losses compared to jump dissipation.....	30
3-1. Steady state velocity vectors -- rotor and stator.....	33
4-1. Centerline of blades defined by Base and Inner curves.....	38
4-2. Pictorial representation of Base curve development scheme.....	39
4-3. Trace curve specification in Z_o-S plane.....	40
4-4. Cylindrical coordinate system.....	41
4-5. Discrete Base curve and direction vectors.....	43
5-1. Profile view of the Test Set and nozzle.....	47
5-2. Test Bed showing nozzle angular displacement and linear offset scales.....	48
5-3. Test Section profile and free surface angle convention.....	50
6-1. P^* and k variation with Re , for fixed %-Fill.....	55
6-2. P^* and k variation with %-Fill, for fixed ω	56
6-3. P^* and k variation with N , with all other parameters held constant.....	57
6-4. P^* and k variation with $B.P.$, with all other parameters held constant.....	58
6-5. P^* and k variation with ε , with all other parameters held constant.....	59
7-1. Radial pressure gradient across recirculating liquid flow.....	63
7-2. Rotor and stator blade cutback scheme.....	64
7-3. Solid body blade shape and tapering scheme.....	65
7-4. Some possible fill conduit locations.....	66
7-5. Performance map of dynamometer.....	68
8-1. Low-speed prototype <i>predicted</i> performance map.....	73
8-2. CAD image of the rotor and stator.....	74
8-3. Sectional sketch of the low-speed prototype.....	75
8-4. Low-speed prototype experimental set-up.....	76
8-5. Recirculation factor trends, (a) k vs. ω , (b) k vs. %-Fill.....	79

8-6.	Friction factor variation with Re.....	80
8-7.	Low-speed prototype empirical performance map.....	80
8-8.	Comparison between measured power absorption & <i>modified predictions</i>.....	81
8-9.	Non-dimensional performance map.....	82
8-10.	Comparison of predicted and measured static pressure rise with ω.....	83
8-11.	Radial velocity profile at different speeds, for <i>100 %-Fill</i>.....	84
8-12.	Power supply step on test.....	85
8-13.	Power supply step off test, with unloaded and fully loaded dynamometer.....	86
8-14.	Rapid aperiodic rotor speed oscillation test.....	87
9-1.	CAD representation of full-scale prototype.....	90
9-2.	Predicted full-scale performance map.....	92
9-3.	Modified estimated full-scale performance map.....	93
10-1.	Engine-dynamometer system with several instruments.....	98

Nomenclature

α	Transformation variable	p_b	Blade pitch
A	Steam vent area	ψ	Blade rake angle
\bar{A}	Total acceleration vector	r	Radius to point in fluid sheet, Ch.2
A_f	Flow cross sectional area	r_i	Radius to free surface, Ch. 2
A_s	Wetted surface area	r_l	Radius to point in liquid sheet
\bar{A}_u	Unit acceleration vector	R_o	Cylindrical radius, Ch. 2
B	Damping coefficient	r	Torus minor radius
β	Rotor and stator blade turning angle	R	Torus major radius
B.P.	Blade packing	R'	Transformation variable
\bar{c}	Curvature vector	Re	Reynolds number
C_d	Drag coefficient	r_o	Radius from center of rotation
\bar{C}_v	Unit curvature vector	R_s	Steam property
\bar{d}	Directional vector	s	Spacing between blades
D	Outside diameter of dynamometer	ρ	Liquid density
d_h	Hydraulic diameter	t	Time, Ch. 10
\bar{D}_u	Unit direction vector	t_{max}	Maximum blade thickness
ϵ	Surface roughness	T	Rotor torque
\dot{E}_{out}	Energy rate out of hydraulic jump	T_z	Torque applied about z-axis
\dot{E}'_{out}	Jump energy rate out per unit width	θ	Nozzle relative angle, Ch. 5
ϕ	Free surface angle, Ch. 5	τ_w	Wall shear stress
f	Friction factor	U	Rotor blade tip speed
γ	Steam property	\bar{U}	Blade tangential velocity vector
Γ	Circulation	V	Recirculation velocity
F_d	Fluid drag force	V_θ	Angular velocity
h	Blade height	V_{rn}	Relative normal velocity
h_{lg}	Latent heat of vaporization	V_t	Tangential velocity
h_w	Wetted blade height	\bar{v}	Base curve position vector
\dot{H}_o	Stagnation enthalpy rate	\bar{V}	Absolute velocity vector
\bar{i}_o	Tangential unit vector	V_{liq}	Liquid volume
\bar{I}	Inner curve vector	V_m	Velocity magnitude
J	Rotational inertia	\bar{V}_u	Unit velocity vector
k	Recirculation factor	\bar{W}	Relative velocity vector
L	Transformation variable	ω	Rotor angular speed
%-Fill	Liquid level in dynamometer	X	Space curve coordinate
\dot{m}	Mass flow rate	X'	Base curve coordinate
N	Number of blades	Y	Space curve coordinate
ν	Liquid kinematic viscosity	Y'	Base curve coordinate
P	Dynamometer power absorption	Z	Space curve coordinate
P^*	Dimensionless power	Z'	Base curve coordinate
p	Pressure	ζ	Polar angle

CHAPTER 1

Conceptualization of Recirculating Flow Steam Generating Dynamometer

1.1 Background

The main function of a shaft-power absorbing dynamometer is to produce a load torque to simulate a duty cycle for developmental and/or diagnostic testing of shaft-power producing engines or machines. There are many different kinds of dynamometers available today that operate according to various physical principles and collectively offer a wide range of power absorption conditions. Some well known examples are, electric eddy-current brakes, viscous shear plate absorbers, perforated disc evaporators, and Froude type water brakes, to name a few. However, these devices generally suffer from at least one of the following problems; lack of portability due to low power density (i.e., large size and weight), complex or costly external apparatus required for operation (e.g., heat exchangers, pumps, or condensers), cavitation erosion which shortens mechanical life of integral parts, or the performance envelope is simply too limited.

In an attempt to overcome these problems Textron-Lycoming (a gas turbine engine manufacturer that is now part of Allied-Signal) developed a preliminary steam generating dynamometer prototype based on the available body of dynamometer knowledge. While the device successfully generated steam, the quality of the effluent was lower than anticipated (i.e., liquid water sprayed out with the steam because of the large degree of blade incidence), resulting in a undesirable large feed-water requirement. Furthermore, there was a significant amount of erosion concentrated in one area of the vanes. Therefore, a need was realized to develop a logical and rigorous method for the design of a portable high-power-density dynamometer that would more successfully overcome the problems described above. This need is the fundamental motivation for the work presented here (which was funded largely by Textron-Lycoming).

The first task was a review of fluid dynamometers in the technical literature, to determine if there were any tools or techniques that could be used here. The conclusions of this literature survey are summarized as follows. Traditional or commercially available fluid dynamometers work by utilizing at least one of the following phenomenon or dissipation

mechanisms; viscous shear, cavitation, incidence, or momentum transfer by hurling fluid between a rotor and stator (possibly several stages).

For example, in a viscous shear plate absorber a large plate (or disc) is mounted to a rotor in close proximity to a stator and immersed in a bath of liquid. As the rotor spins the disc (or discs) develop a shear stress that leads to viscous dissipation in the fluid. Cool fluid must continually replace hot fluid which can be either dumped to a sink or fed through external equipment, cooled, and recycled. However, in order to get high power absorption levels the shear surface area must be extensive, resulting in a large and massive dynamometer. Other problems with this type of machine are that the performance envelope is very narrow which limits its utility, and the external equipment required for continuous operation makes the device bulky and impractical to transport.

The perforated disc evaporator functions in the same basic way except that the plates (or discs) have holes bored in them to induce cavitation. The cavitation augments power dissipation and thus reduces the overall size of the machine. Vapor that is generated as power is absorbed can be either vented straight into the atmosphere or condensed and recycled through external equipment. The main problems with this device are vibration and cavitation erosion which results in excessive mechanical wear and thus frequent part replacement. The current status of these cavitating devices is concisely summarized by *Courtney* [1].

Less self destructive machines are the Froude type water brakes. These devices consist of a fluid filled toroidal working compartment, much like a fluid coupling or torque converter, that is split into two halves (generally equal in volume and shape) forming a rotor and stator. The rotor has radial vanes (or some deviation thereof) that spins or hurls the liquid into the stator stage, which may also have vanes. The device absorbs power primarily through incidence resulting from the liquid impingement on the vanes, and to some extent viscous friction. Theories have been developed and experiments executed by *Raine* [2] and *Shute* [3] that are a good source of information for modeling or sizing standard Froude-type water brakes. These devices have existed for a long time and, over the ages, many attempts have been made to improve performance by varying the number, position, shape, and angle, of the vanes such as the work presented by *Patki and Gill* [4] and others. Most of the analyses or experimental data presented in the literature is for fully filled machines. Some recent work by *Raine and Hodgson* [5] formalizes the current status of these Froude type machines, and presents an analytical method for predicting performance of both fully

and partially filled liquid water brakes. Unfortunately, Froude type water brakes suffer from low power density, erosion, and a performance envelope that is too limited to meet the requirements of modern gas turbine engines (although partial fill improves this). The material reviewed in the literature was not directly applicable to the development of the type of dynamometer required for this application. This substantiated the need for the work reported here.

Simply stated, the objective of this work is the development of a new type of hydraulic dynamometer that is suitable for the diverse range of power levels and high rotor speeds associated with modern gas turbine engines, as well as a method for the design of these new turbomachines. The desired characteristics of the dynamometer are long-life, transportability, high-power-density, and a wide operational envelope.

1.2 New Dynamometer Concept

To accomplish this objective a new type of dynamometer has been developed that functions by developing an organized high-speed free-surface liquid flow that helically recirculates on the inside surface of a torus. An impeller (or rotor) is used to accelerate the liquid to a high speed at which point rotor power input is absorbed by primarily viscous dissipation in the recirculating stream. The thesis develops an appropriate geometric configuration and blading scheme that produces this flow.

In order to have viscous dissipation as the primary power absorption mechanism, a high speed recirculating flow must be generated. A torus, which is particularly well suited for a recirculating flow, was selected as the working compartment geometry, although there are several other possible geometric configurations that could have been used. This flow can be visualized as a sheet of liquid that helically swirls around, or recirculates, on the inside surface of the torus. The liquid is accelerated by a bladed rotor (which is part of the torus) and is held against the toroidal surface by a strong centrifugal field. A large radial pressure gradient that results from the streamline curvature of the liquid flow stratifies the fluid by density resulting in the evolution of a vapor core surrounded by a liquid sheet, as shown in Figure 1-1. As vapor is generated it is vented through radial holes in the blades (described below) that cut through the liquid layer into the vapor core. Furthermore, due to the

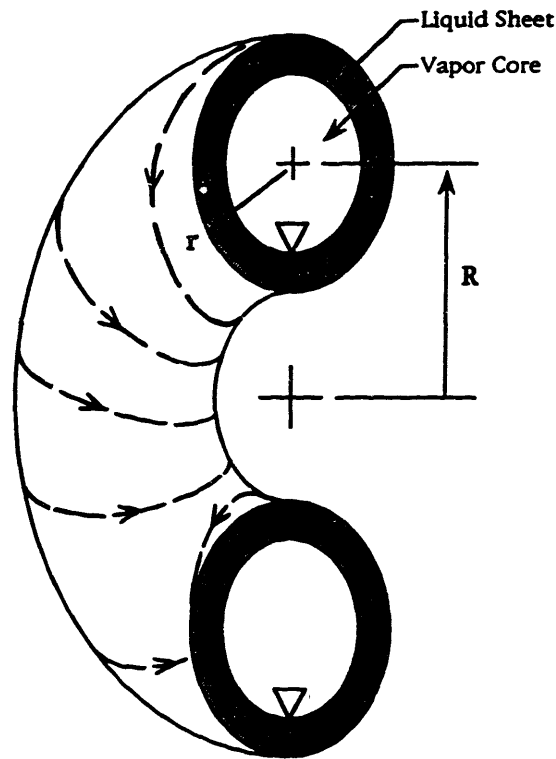


Figure 1-1. Vapor-liquid stratification in torus

presence of this large radial pressure gradient, boiling is confined to a relatively thin layer of the liquid sheet near the free surface. The power absorption in this device is clearly related to the amount of liquid water in the toroidal working compartment (or thickness of the liquid sheet) and the fluid recirculation velocity.

A unique blading scheme has been developed that produces this phase separated helical flow. The torus is divided in two parts (or stages), a bladed rotor stage and a bladed stator stage. The rotor is the inner part of the torus, or region inside the major radius, and the stator is the remainder of the torus, as depicted in Figure 1-2. The liquid flowing between the rotor blades is accelerated and exits into the inlet of the stator stage. The liquid flows between the stator blades and, due to the toroidal geometry, exits back into the inlet side of

the rotor stage where the process continues. The liquid in this flow circuit accelerates until the power dissipated by viscous shear equals the power input by the rotor. The rotor torque input, recirculating mass flow rate, and power dissipation, are all coupled to the

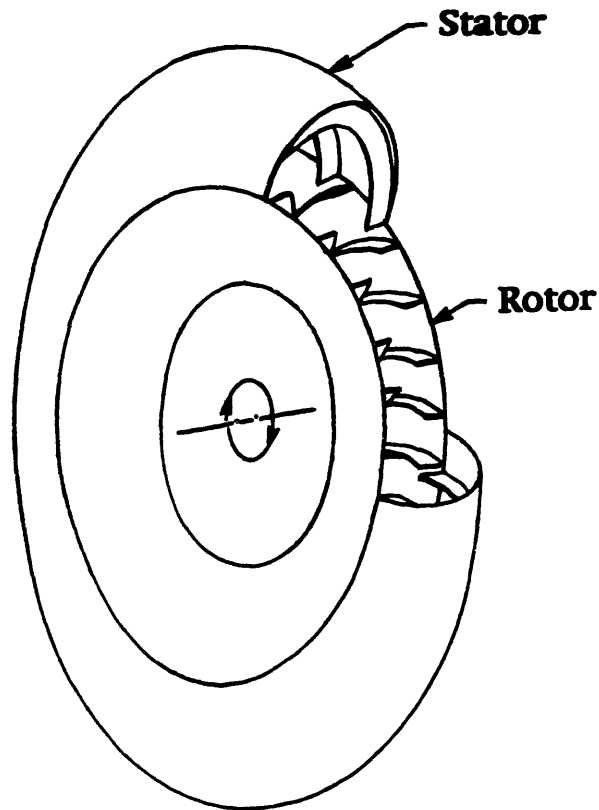


Figure 1-2. Toroidal geometry with rotor and stator blading

geometric profile (or turning angle) of the rotor and stator blades. However, to make the liquid flow smoothly through this turning angle, the blades must be oriented (defined by rake angle) properly at each point throughout the flow circuit. In other words, the blades must act effectively as the walls of channels in which the liquid flows, as depicted in Figure 1-3. Developing blades in this way reduces the propensity for incidence and cavitation, which is undesirable because it results in localized mechanical wear or concentrated erosion.

The appropriate blade turning and rake angles (which define the shape of the blade) are determined from mass, momentum, and energy conservation, as well as the concept of geometric principle curvature. The turning angle (β) is defined as the angular change in

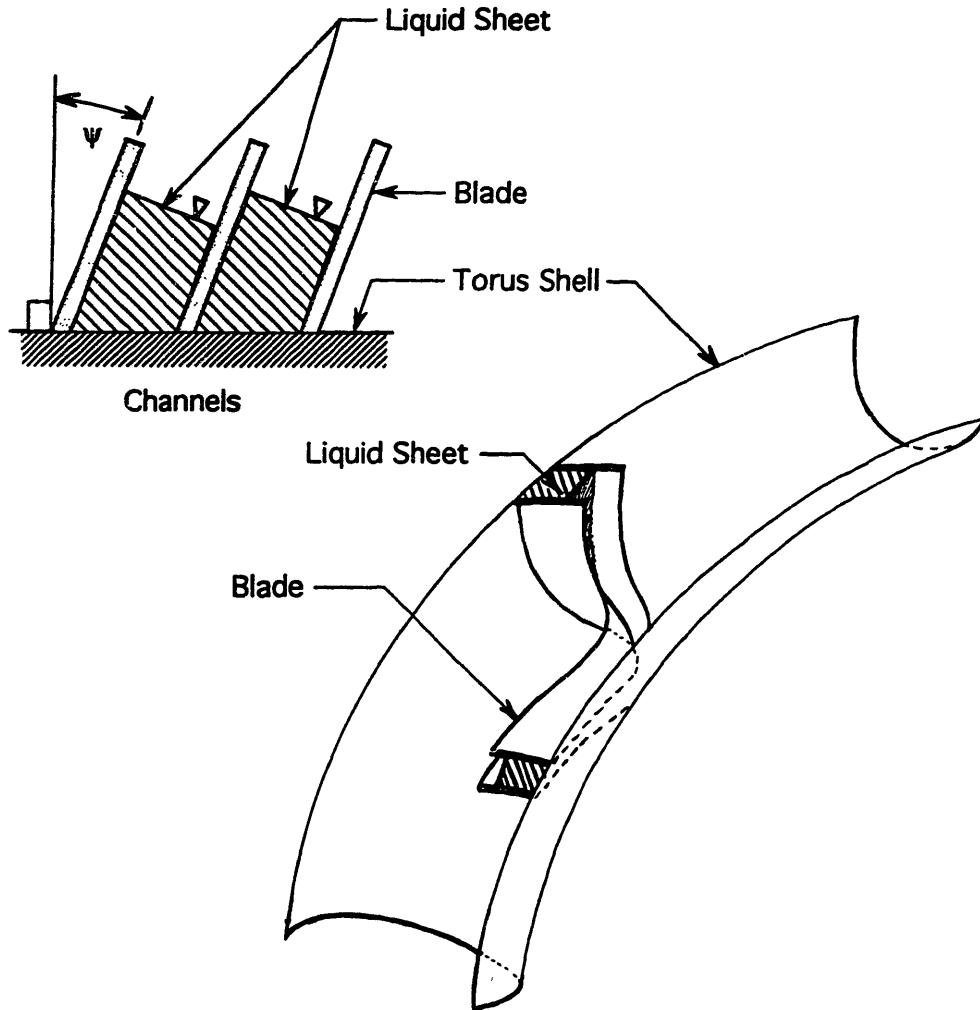


Figure 1-3. Channels formed by blades

direction that the liquid flow undergoes between the inlet and outlet of either stage. The rake angle (ψ) is defined as the angle between the blade and a line perpendicular to the torus shell, as shown in Figure 1-3. A blading algorithm and quantitative techniques have been developed in the thesis for the rigorous determination of blade shapes (*defined by β and ψ*) that produce this high-speed helically recirculating liquid flow. The advantages of a dynamometer that operates based on this flow are summarized below.

1.3 Resulting Advantages

There are several advantages that result from a dynamometer that operates based on this unique liquid flow. Clearly, by utilizing the liquids latent heat of vaporization the dynamometer power density is quite high. Furthermore, configuring the rotor and stator stages and blading in this way results in several practical benefits.

The power density of this dynamometer is much higher than conventional (non cavitating) liquid dynamometers because a portion of the recirculating liquid stream undergoes a phase transition. Furthermore, nearly pure steam generated as power is absorbed collects in the inner part (or core) of the torus that can be accessed with the stator blades and vented straight to atmosphere. This not only reduces the feed-water requirements (because the steam quality is high), but also eliminates the need for bulky external support apparatus. The combination of these feature results in a high-power-density dynamometer that can be easily transported. This is particularly beneficial for diagnostic testing of engines, which is typically done by removing and shipping the troubled engine to a test facility which is extremely costly. A portable dynamometer will greatly reduce the cost associated with this type of engine testing.

The dynamometer power absorption is a function of both rotor speed (ω) and liquid level (or volume of liquid) in the working compartment. In other words, at a fixed ω the absorption level can be varied by changing the amount of liquid in the working compartment. Therefore, the dynamometer has a wide range of operation that is suitable for modern gas fueled turboshaft engines.

Another benefit, that results from this rotor-stator configuration, is that the net axial thrust produced is approximately zero. This clearly reduces the cost associated with dynamometer fabrication. In a typical Froude type dynamometer axial thrust is typically handled by designing the machine such that it has two equal (but opposite facing) working compartments which cancel out each others thrust. This obviously increases the size and complexity of the device, which is undesirable.

Finally, the dynamometer developed here absorbs power through primarily shear stress induced dissipation, which acts on the entire wetted surface of the machine. Since this organized dissipation mechanism is distributed over a relatively large area, the propensity

for concentrated erosion is minimized and the machine life is considerable increased, which is beneficial for obvious reasons.

1.4 Outline of Thesis

The thesis presents a logical and rigorous method (based on a flow model, blading algorithm, and numerical programs) that can be used to design dynamometers that develop a recirculating liquid flow, and predict power absorption (P) as a function of rotor speed (ω) and liquid level (*%-Fill*). A blade cascade experiment was conducted and a low-speed prototype was designed, constructed, and tested to validate theoretical predictions and explore the question of dynamic stability. The numerical programs can be used for design, analysis and performance prediction which, in conjunction with the experimental results, serves as a basis for a general algorithm that can be used to design this new type of turbomachine. Furthermore, some scaling laws are identified which are useful for making rough performance extrapolations. Finally, control issues are explored for a typical engine-dynamometer system and some possible control scenarios are presented that aid in the application of this new dynamometer.

In Chapter 2, different dissipation mechanisms are examined that can absorb a significant amount of power while maintaining an organized recirculating flow, and quantitative techniques for estimating power absorption are presented. This leads to the development of a flow model in Chapter 3 which equates rotor power input with shear stress induced dissipation, and determines the appropriate blade profiles (*fluid turning angles*, β) that result in this power balance. In Chapter 4 a blading algorithm and numerical programs are presented that were developed here and used to generate rotor and stator blades that have the correct shape (*defined by β and ψ*) for this device. The programs are included in Appendix B. Then a blade cascade flow visualization experiment was conducted to verify the blading algorithm and examine the impact of varying parameters way off design. The conclusions and results of this experiment are presented in Chapter 5. The experimental procedures and raw data are included in Appendix A.

In Chapter 6 a numerical code is presented that was developed based on the flow model and blading algorithm. Also, some key dimensionless parameters are identified that characterize this new dynamometer. Among other things, the code can be used to make dimensionless performance estimations, study the effects of parameter variations, as well

as predict P for any particular ω and %-Fill. Some examples are presented for the purpose of illustration. The code and a sample run are presented in Appendix C.

The dynamometer code and blading programs form the basis of a rigorous general algorithm, presented in Chapter 7, that can be used to design this new type of dynamometer. A method for liquid filling and steam venting is presented that takes advantage of the natural phase separation (resulting from the large centrifugal field) in the working compartment. Furthermore, some scaling laws were identified that relates P to ω and size (D), which are useful for making rough performance extrapolations. In Chapter 8 the general algorithm is applied to the design of a low-speed prototype, which was subsequently constructed and tested to verify the basic liquid flow characteristics and explore the question of dynamic stability. The experimental results are presented and compared to theoretical predictions. This information, in conjunction with the general algorithm, was used to design a high speed full-scale steam generating prototype which is presented in Chapter 9.

Finally, fundamental dynamics and control issues were explored for a typical engine-dynamometer system, and some possible control scenarios are presented in Chapter 10 to aid in the application of this new dynamometer. Chapter 11 consists of a summary of the main contributions of this thesis, as well as some proposals for future work.

CHAPTER 2

Investigation of Power Absorbing Mechanisms

2.1 Overview

The main task here is to dissipate power in the working fluid of the dynamometer. Enough power must be dissipated so that the dynamometer has a high power density. There are several possible fluid dissipation mechanisms that can be considered, including incidence or shock, frictional drag or shear stress, or dissipation associated with the formation of a hydraulic jump. However, incidence or shock losses are usually caused by fluid impingement on machine parts resulting in damage, and a relatively short mechanical life, which is inconsistent with the fundamental objective. Conversely, the latter two dissipation mechanisms can be generated in an organized (much less destructive) flow and can absorb significant amounts of power. Therefore, hydraulic jumps and wall shear stress are investigated in the following sections as potential power absorption mechanisms.

2.2 Hydraulic Jump Induced Dissipation

Inside the dynamometer there is a centrifugally accelerated two-phase, helically swirling, free surface flow. Since the flow has a free surface, it is capable of spontaneously hydraulically jumping to a lower energy state, which can be exploited as a power absorption mechanism. To precisely model a hydraulic jump in this complex toroidal flow would be extremely difficult and unnecessary to capture the essence of the jump. Instead, the jump behavior is explored in a cylindrical system, concentrating on the important fundamental characteristics without complicating the equations with the toroidal geometry. This is a reasonable approximation since the flow's helical progression speed is (by design) small compared to its angular (tangential) velocity (V_{θ}) component around the minor dimension of the torus.

Therefore, the first step to modeling a hydraulic jump in the dynamometer is to unfold the torus into a right circular cylinder and focus on an infinitely thin cylindrical section, see Figure 2-1. Then, the velocity field in the flow circuit must be modeled. Since the Reynolds number for this flow is very large (by design), the liquid can be approximated as inviscid, except within a very small boundary layer that can be safely neglected here

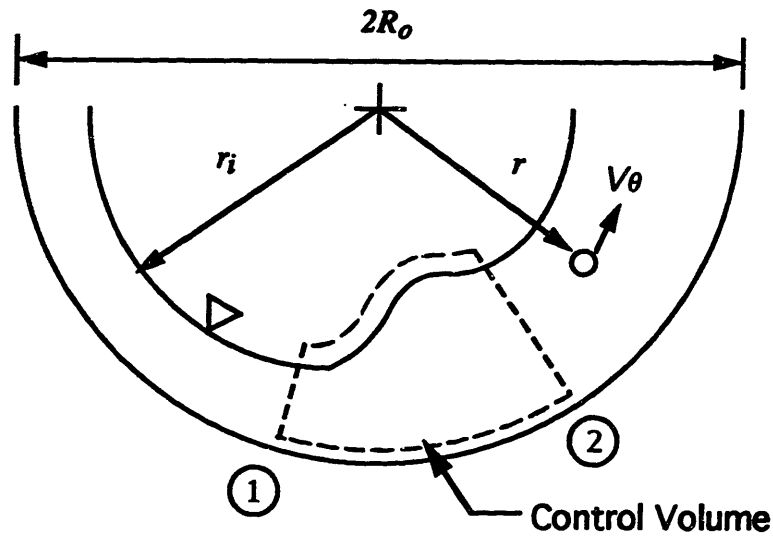


Figure 2-1. Modeling a hydraulic jump in cylindrical coordinates

because it has little impact on the jump. To conserve angular momentum the angular velocity of a fluid particle times the radius (or distance from the center of rotation to the particle) must be constant. This is the well known Free Vortex solution to Euler's Equation (in streamline coordinates) for steady incompressible flow,

$$V_{\theta} = \frac{C}{r} \quad (2.1)$$

$$C = \frac{\Gamma}{2\pi} \quad (2.2)$$

where the constant is proportional to the circulation (Γ), and the radial and axial components of velocity are negligible compared to the angular component.

The radial pressure gradient (traversing the liquid sheet) can be described in terms of the angular (tangential) velocity, using Euler's Equation in streamline coordinates.

$$\frac{\partial p}{\partial r} = \rho \frac{(V_{\theta})^2}{r} = \frac{\rho \Gamma^2}{4\pi^2 r^3} \quad (2.3)$$

Since the rate of pressure change in the radial direction is much greater than in any other direction the partial differential equation can be reasonably approximated by an ordinary differential equation. The radial pressure distribution is determined by integrating this equation from the inside free surface of the flow (r_i) to any point (r) within the liquid sheet.

$$\int_{r_i}^r dp = \rho \frac{\Gamma^2}{4\pi^2} \int_{r_i}^r (dr/r^3) \quad (2.4)$$

$$p_s(r) = p(r) - p_o = \rho \frac{\Gamma^2}{8\pi^2} \left(\frac{1}{r_i^2} - \frac{1}{r^2} \right) \quad (2.5)$$

The gage pressure distribution ($p_g(r)$) is relative to the core pressure (p_o), which is assumed to be atmospheric. The (gage) pressure distribution is used subsequently to evaluate the angular momentum and energy equations across the hydraulic jump. But first, continuity must be addressed.

Clearly, the mass flowing upstream (pre-jump) of the hydraulic jump must equal the mass flowing down stream (post-jump), neglecting the mass leaving as vapor which is several orders of magnitude smaller than the liquid terms (again by design). Furthermore, since the normal velocity component is approximately equal to the angular velocity at any point in the liquid sheet, the mass flow rate in the circuit per unit width of the cylinder can be evaluated as follows.

$$\dot{m}_{in} = \dot{m}_{out} = \dot{m} = \rho \int_{r_i}^{R_o} V_\theta dr = \frac{\rho \Gamma}{2\pi} \ln(R_o/r_i) \quad (2.6)$$

The circulation can be solved for using this expression, and noting that the mass flow rate per unit width divided by the density is the volume flow rate per unit width (Q').

$$\Gamma = \frac{2\pi Q'}{\ln(R_o/r_i)} \quad (2.7)$$

Now the angular momentum across the hydraulic jump can be readily evaluated. The Angular Momentum Theorem states that the rate of change in angular momentum in a given control volume, plus the net efflux of angular momentum across the control surface, must equal the total torque acting on the control volume. In the steady state case, the net rate of change of angular momentum in the control volume is zero. Therefore, the angular

momentum equation can be written in standard notation for the control volume shown in Figure 2-1 as follows.

$$\int_{c.v.} \rho(r \times V) V_{rn} dA = T_z \quad (2.8)$$

The cross product of the radius with velocity is simply equal to the angular (tangential) velocity times the radius to that point in the liquid sheet. The relative normal velocity (V_{rn}) is also equal to the angular velocity. The torque applied to the control volume (neglecting skin friction) results from the different pressure forces acting on opposite sides of the jump, due to the difference in pre and post jump liquid sheet thickness. Therefore, the angular momentum equation for the hydraulic jump in this cylindrical system can be expressed as follows.

$$\int_1 \rho(r V_{\theta}^2) dr - \int_2 \rho(r V_{\theta}^2) dr = \int_2 r p dr - \int_1 r p dr \quad (2.9)$$

Where the numbers 1 and 2 designate pre-jump and post-jump respectively as shown in Figure 2-1. Combining this with Equations (2.1), (2.2), and (2.5), transforms the angular momentum equation into a more useful form.

$$\int_1^{R_o} \rho \frac{\Gamma^2 dr}{4r\pi^2} - \int_2^{R_o} \rho \frac{\Gamma^2 dr}{4r\pi^2} = \int_2^{R_o} r \rho \frac{\Gamma^2}{8\pi^2} \left(\frac{1}{r_1^2} - \frac{1}{r^2} \right) dr - \int_1^{R_o} r \rho \frac{\Gamma^2}{8\pi^2} \left(\frac{1}{r_1^2} - \frac{1}{r^2} \right) dr \quad (2.10)$$

Where again r_i is the radial distance from the cylinder's center to the free surface and R_o is one half of its diameter. This integral can now be directly evaluated.

$$\begin{aligned} & \frac{\Gamma_1^2}{4\pi^2} \ln\left(\frac{R_o}{r_1}\right) - \frac{\Gamma_2^2}{4\pi^2} \ln\left(\frac{R_o}{r_2}\right) = \\ & \left[\frac{\Gamma_2^2}{16\pi^2} \left(\frac{R_o^2}{r_2^2} - 1 \right) - \frac{\Gamma_2^2}{8\pi^2} \ln\left(\frac{R_o}{r_2}\right) \right] - \left[\frac{\Gamma_1^2}{16\pi^2} \left(\frac{R_o^2}{r_1^2} - 1 \right) - \frac{\Gamma_1^2}{8\pi^2} \ln\left(\frac{R_o}{r_1}\right) \right] \end{aligned} \quad (2.11)$$

This equation can be simplified by collecting common terms, as in Equation (2.12).

$$\Gamma_1^2 \left[2 \ln\left(\frac{R_o}{r_1}\right) + \left(\frac{R_o^2}{r_1^2} - 1 \right) \right] = \Gamma_2^2 \left[2 \ln\left(\frac{R_o}{r_2}\right) + \left(\frac{R_o^2}{r_2^2} - 1 \right) \right] \quad (2.12)$$

This can be further simplified by using Equation (2.7) to eliminate the circulation terms.

$$\frac{2\ln\left(\frac{R_o}{r_1}\right) + \left(\frac{R_o}{r_1}\right)^2 - 1}{\left[\ln\left(\frac{R_o}{r_1}\right)\right]^2} = \frac{2\ln\left(\frac{R_o}{r_2}\right) + \left(\frac{R_o}{r_2}\right)^2 - 1}{\left[\ln\left(\frac{R_o}{r_2}\right)\right]^2} \quad (2.13)$$

Interestingly, from the Angular Momentum Theorem it is clear that a hydraulic jump in a cylindrical system is independent of the mass flow rate, with respect to the post-jump liquid sheet thickness. This means that the post-jump liquid sheet thickness h_2 (equal to $R_o - r_2$) is uniquely determined by the pre-jump thickness h_1 (equal to $R_o - r_1$). Of course h_1 (and thus the input radius ratio r_1/R_o) depends on the mass flow rate or, more specifically, the recirculating mass flow rate. Furthermore, one side of equation (2.13) contains all of the information needed to completely characterize the hydraulic jump, and is a non-dimensional number that shall be referred to hereafter as the Jump number or Jump Function [JF]. Figure 2-2 shows how the Jump Function varies with flow ratio r/R_o over a wide range of values. From the figure it is clear that for any flow ratio other than 0.367 there are two solutions to the Jump Function. However, only one solution is physical

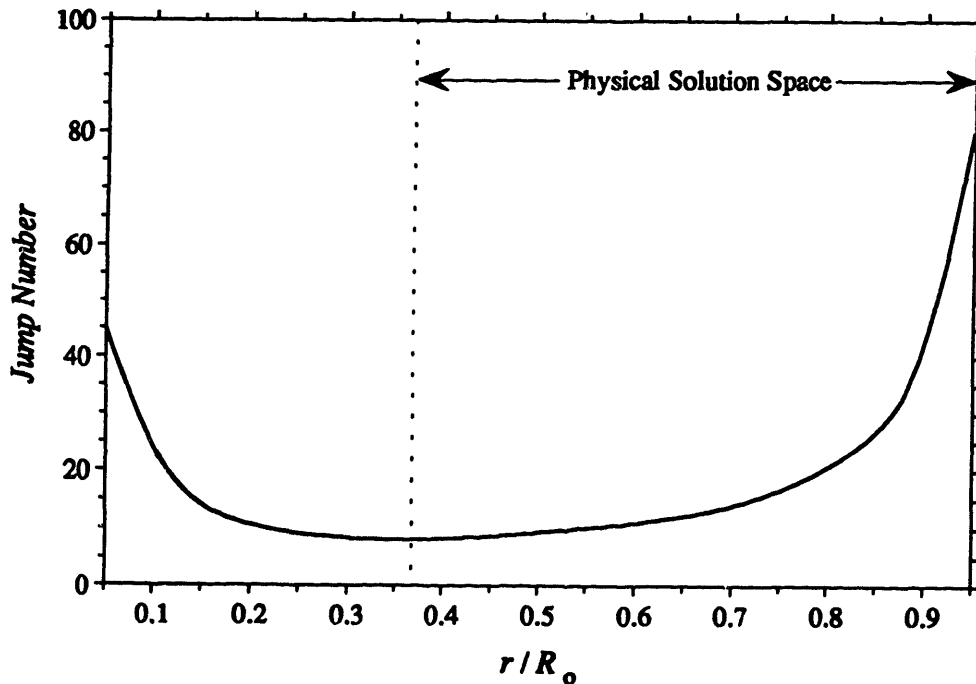


Figure 2-2. Jump Function (Number) dependence on flow ratio

and does not violate the Second Law of thermodynamics. The same holds true for a linear hydraulic jump in a rectangular channel, which can only spontaneously jump from a (high energy) super-critical flow to a (low energy) sub-critical flow. The difference in kinetic energy is equal to the heat added to the water. In a linear hydraulic jump the characterizing parameter is the Froude number, while in a cylindrical system the equivalent parameter is the Jump number (or Function). If the Froude number is greater than one, or in the cylindrical system the Jump number is greater than 0.367, then the flow is super-critical and a hydraulic jump is possible. A spontaneous jump in the opposite direction is not physical.

To clarify this a little further look at Figure 2-2 again. Envision a vertical line parallel to the ordinate that passes through the 0.367 point on the abscissa (represented by a broken line in the figure). The line cuts the space into two regions. The region on the right side of the line is the physical solution space, which means if the flow has a radius ratio greater than 0.367 then a spontaneous jump is possible. If a jump occurs, then the post-jump liquid sheet thickness can be easily evaluated by determining the radius ratio on the left side of the solution space that corresponds to the same Jump Number in the physical region.

Now that the jump characteristics have been quantified, the power dissipated (as heat) by the jump can be examined. Consider again a control volume that surround a hydraulic jump in a cylindrical system. Using the First Law of thermodynamics, for a steady bulk flow process, the following observations can be made. The difference in the stagnation enthalpy rate between the pre and post-jump liquid sheets must be equal to the energy (heat) rate out of the control volume.

$$\dot{E}_{out} = \dot{H}_{oin} - \dot{H}_{oout}, \text{ where } \dot{H}_o = \dot{m} \left(u + \frac{p}{\rho} + \frac{V^2}{2} \right) \quad (2.14)$$

It is reasonable to assume that the hydraulic jump will occur at near isothermal conditions in the steady case, since the objective is to induce boiling in the vicinity of the jump. Thus, the specific internal energy will be the same on both sides of the jump and cancel out of the equation. Therefore, the energy balance across the jump can be written in integral form as follows.

$$\dot{E}_{out} = \int_{r_1}^{R_o} \left(\frac{p}{\rho} + \frac{V^2}{2} \right) d\dot{m} - \int_{r_2}^{R_o} \left(\frac{p}{\rho} + \frac{V^2}{2} \right) d\dot{m} \quad (2.15)$$

Consider one of the integrands of this equation, with the previously derived expressions for $p(r)$ and $V(r)$ substituted in.

$$\frac{p}{\rho} + \frac{V^2}{2} = \frac{\Gamma^2}{8\pi^2} \left(\frac{1}{r_1^2} - \frac{1}{r^2} \right) + \frac{\Gamma^2}{8\pi^2 r^2} = \frac{\Gamma^2}{8\pi^2 r_1^2} \quad (2.16)$$

Interestingly, the integrand is only a function of the circulation and radius to the free surface of the liquid sheet (a constant input parameter), and is independent of the radius to a fluid particle inside the liquid. Substituting Equation 2.16 into 2.15 yields the following energy balance on a per unit width basis.

$$\dot{E}_{out} = \frac{\dot{E}_{out}}{\text{unit width}} = \int_{r_1}^{R_o} \rho \left(\frac{\Gamma_1^2}{8\pi^2 r_1^2} \right) \frac{\Gamma}{2\pi r} dr - \int_{r_2}^{R_o} \rho \left(\frac{\Gamma_2^2}{8\pi^2 r_2^2} \right) \frac{\Gamma}{2\pi r} dr \quad (2.17)$$

Again, r_1 and r_2 are the radial distances from the center of the cylinder to the free surface before and after the jump respectively, and R_o is half of the cylinder's diameter. Evaluating the integrals in Equation 2.17 yields an expression involving logarithmic functions of the up and down stream radius ratios.

$$\dot{E}_{out} = \left(\frac{\rho \Gamma_1^2}{8\pi^2 r_1^2} \right) \frac{\Gamma_1}{2\pi} \ln \left(\frac{R_o}{r_1} \right) - \left(\frac{\rho \Gamma_2^2}{8\pi^2 r_2^2} \right) \frac{\Gamma_2}{2\pi} \ln \left(\frac{R_o}{r_2} \right) \quad (2.18)$$

The energy equation can be further simplified by substituting in Equation 2.7 and collecting similar terms.

$$\dot{E}_{out} = \frac{\rho(Q')^3}{2r_1^2 \left[\ln \left(\frac{R_o}{r_1} \right) \right]^2} - \frac{\rho(Q')^3}{2r_2^2 \left[\ln \left(\frac{R_o}{r_2} \right) \right]^2} \quad (2.19)$$

This equation can be put into dimensionless form by rearranging terms as follows.

$$\frac{2r_1^2 \left[\ln\left(\frac{R_o}{r_1}\right) \right]^2}{\rho(Q')^3} (\dot{E}_{out}) = 1 - \left(\frac{r_1}{r_2}\right)^2 \left[\frac{\ln\left(\frac{R_o}{r_1}\right)}{\ln\left(\frac{R_o}{r_2}\right)} \right]^2 \quad (2.20)$$

Notice that the right hand side of the equation can be computed from exclusively angular momentum results. Physically this number is the fraction of the initial (or pre-jump) head that is irreversibly converted into heat by the hydraulic jump. Hereafter this number is referred to as the Jump Energy Fraction (or Function), abbreviated simply as [JEF].

The results of evaluating the [JEF] over a wide range of values is plotted in Figure 2-3. For any flow ratio the [JEF] is easily determined. But again, only input radius ratios greater than 0.367 (supercritical flow) are valid (i.e., can jump to a lower energy state). The physical space here is the positive region of the solution space, or everything to the right of $(r_1/R_o)=0.367$. This one-dimensional cylindrical hydraulic jump model can now be used to estimate how much dissipation will occur in a dynamometer utilizing a jump to absorb power — neglecting other loss mechanisms.

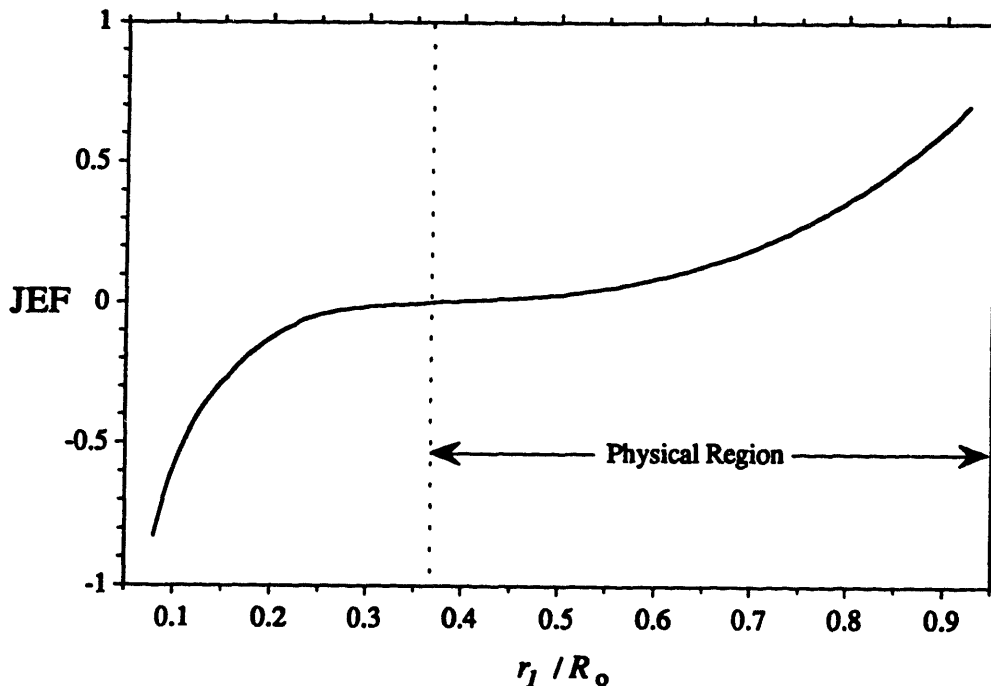


Figure 2-3. [JEF] variation with flow radius ratio (r_1/R)

To proceed, consider the rotor blades in the cylindrical system to be approximated by a cascade of linear blades. That is, in the proximity of the rotor blades unwrap the cylindrical flow circuit and treat it as a linear flow system, which is a reasonable estimation technique for a first approximation. This simplifies the equations by permitting the rotor power input to be estimated with a linear momentum balance across the blades. Then the force (F) exerted by a rotor blade on the flow can be written as follows, where V_{t1} and V_{t2} are the

$$F = \dot{m}(V_{t2} - V_{t1}) \quad (2.21)$$

tangential velocities at the blade inlet and outlet respectively. Equation 2.22 is the mass flow rate per blade pitch (p_b),

$$\dot{m} = \rho h p_b V_{n1} \quad (2.22)$$

where h is the liquid sheet height (or thickness) through the rotor stage, p_b is the pitch (blade spacing) and V_{n1} is the normal component of velocity at the rotor inlet. The difference in tangential velocity is approximately equal to (by design) the average rotor blade velocity (U). Combining this with Equation 2.21 yields an expression for the force acting on the rotor blade, in previously determined variables.

$$F \approx \rho h p_b V_{n1} U \quad (2.23)$$

The rotor power input per pitch (P') is equal to the force per pitch multiplied by the average rotor blade velocity.

$$P' = \frac{P}{p_b} = \frac{F \cdot U}{p_b} \approx \rho h V_{n1} U^2 \quad (2.24)$$

Non-dimensionalizing this yields the dimensionless power (P^*) input to the rotor (per pitch), which is clearly a function of liquid sheet height (h) and velocity ratio (V_{n1}/U).

$$P^* = \frac{P'}{R_o U^3 \rho} = \frac{h_2}{R_o} \left(\frac{V_{n1}}{U} \right) = \frac{(R_o - r_2)}{R_o} \left(\frac{V_{n1}}{U} \right) \quad (2.25)$$

Since all the rotor input power is assumed to be absorbed in the jump, Equation 2.24 must be equal to jump energy rate (\dot{E}'), which can be extracted from Equation 2.20.

$$\rho h_2 V_{n1} U^2 = \frac{\rho(Q')^3[\text{JEF}]}{2r_1^2 \left[\ln\left(\frac{R_o}{r_1}\right) \right]^2} \quad (2.26)$$

Since the volume flow rate per unit width (Q') is equal to the height (h_2) times the normal velocity ($V_1=V_2=V_{n1}$), this expression can be further simplified.

$$h_2 V_{n1} U^2 = \frac{h_2^3 V_{n1}^3 [\text{JEF}]}{2r_1^2 \left[\ln\left(\frac{R_o}{r_1}\right) \right]^2} \quad (2.27)$$

Rearranging terms gives the following compact form of the energy balance between rotor input and jump output.

$$\left(\frac{U}{V_{n1}} \right)^2 = \frac{h_2^2 [\text{JEF}]}{2r_1^2 \left[\ln\left(\frac{R_o}{r_1}\right) \right]^2} = \frac{(R_o - r_2)^2 [\text{JEF}]}{2r_1^2 \left[\ln\left(\frac{R_o}{r_1}\right) \right]^2} \quad (2.28)$$

This relationship combines the results of the angular momentum analysis with the power balance between rotor input and jump dissipation. The (recirculation) velocity ratio can be computed from this equation, once the jump is characterized, and used in Equation 2.25 to compute the dimensionless power input to the rotor, which is equal to the power dissipated by (in) the dynamometer.

This information can now be used to estimate power dissipation for different rotor speeds. But first, some rough machine (toroidal) dimensions must be selected for a hypothetical dynamometer. The toroidal major radius is selected to be 6 inches, and the minor radius 3 inches. Therefore, the cylindrical diameter is 6 inches, and the dynamometer outside diameter is 18 inches. Furthermore, water is selected as the working fluid in this hypothetical case.

Figure 2-4 is a plot of the power absorbed in this hypothetical dynamometer by a hydraulic jump over a wide range of rotor speeds. The power curve is more accurate at low rotor

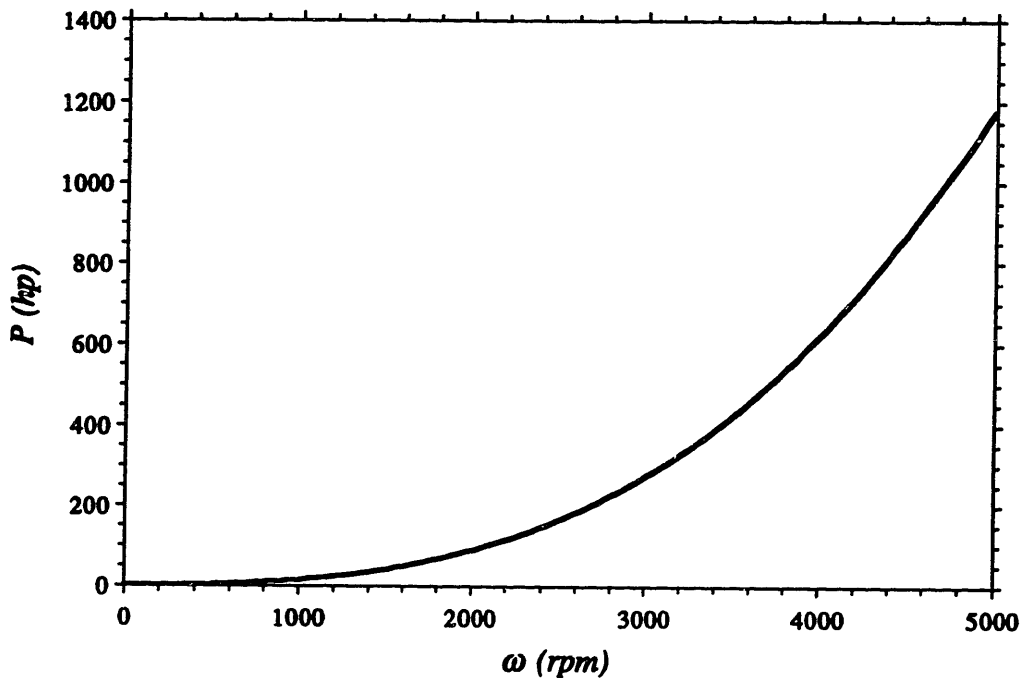


Figure 2-4. Power dissipated by a hydraulic jump

speeds because at high rotor speeds the jump dissipation rate becomes so high that appreciable mass leaves the jump in the form of vapor. Thus, at very high rotor speeds the analysis breaks down somewhat, but is still a reasonable and conservative first order tool for estimating power absorption by this particular dissipation mechanism. In the above analysis the losses associated with skin friction were neglected. However, at high speeds these losses are not small, and in fact may be quite large, which is the subject of the next section.

2.3 Shear Stress Induced Dissipation

In the previous section a hydraulic jump was investigated as a potential power dissipation mechanisms for the dynamometer, neglecting any contribution from skin friction. Clearly, as the rotor speed increases the recirculation velocity (which is approximately normal to the

blade rotational velocity) must also increase. At some point the skin friction induced dissipation must become significant, and can in fact be more effective than the jump as a power absorber. This is discussed below, as well as the conditions that are required to produce significant frictional dissipation.

The viscous losses in the recirculating liquid sheet can be estimated by calculating the skin friction drag acting on the wetted surface of the flow circuit. The drag force (F_d) can be written as follows, where ρ is the liquid density, A_s is the wetted or shear surface area, C_d is the average drag coefficient, and V is the (recirculating) liquid stream velocity which can be expressed as a factor (k) times the average rotor blade speed (U).

$$F_d = \frac{1}{2} \rho A_s C_d V^2 = \frac{1}{2} \rho A_s C_d (kU)^2 \quad (2.29)$$

Clearly, the power dissipated by friction is simply the drag force F_d multiplied by the recirculation velocity V .

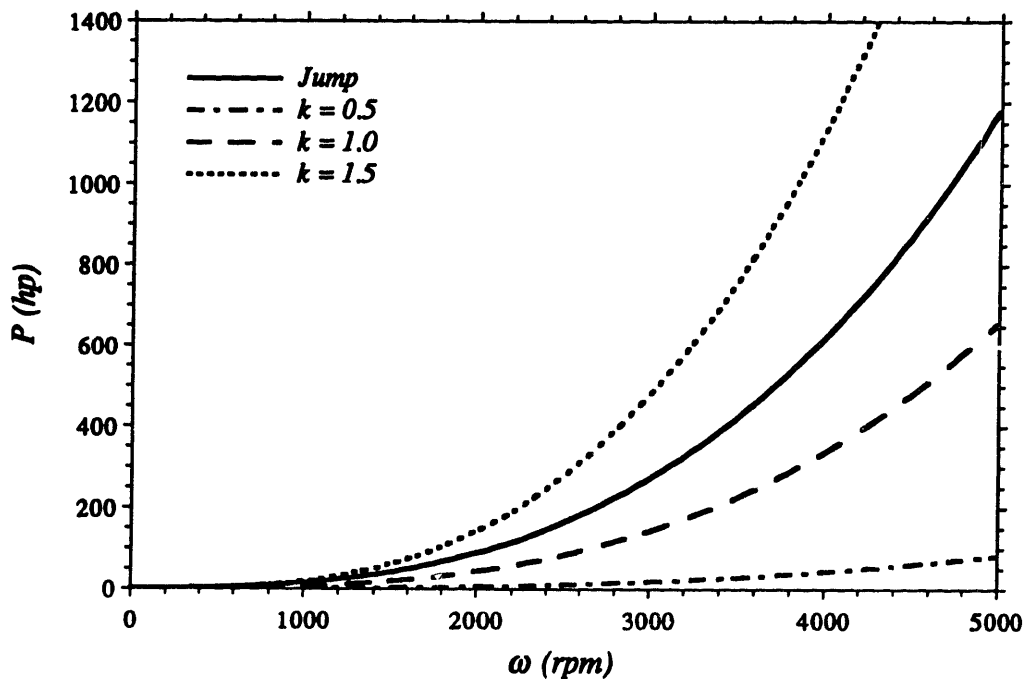


Figure 2-5. Shear induced frictional losses compared to jump dissipation

To get some tangible dissipation estimates, consider again the hypothetical dynamometer discussed in the previous section. The wetted surface area can be approximated as the surface area of the torus and the average drag coefficient can be conservatively estimated to be 0.01. With these approximations the shear induced frictional power dissipation can be evaluated. Figure 2-5 shows the power dissipation for several different recirculation factors (k), compared to the power absorbed by a hydraulic jump, over a wide range of rotor speeds. Notice that the shear induced power dissipation surpasses the hydraulic jump dissipation when the recirculation factor reaches a value somewhere between 1.0 and 1.5. In other words, for high recirculation factors the power dissipated by skin friction is more substantial than the power absorbed in a hydraulic jump.

Theoretically both dissipation mechanisms could be used to absorb substantial amounts of power. However, practical implementation of a hydraulic jump in a toroidal system is extremely difficult. The first question is how to design the blades so that a sub-critical flow is accelerated to a super-critical flow, without promoting destructive cavitation. The next question is how to control the jump to ensure that a jump occurs consistently in the appropriate location. Weirs can be used but would cause mechanical erosion, especially at high rotor speeds, which is inconsistent with the fundamental objective here. Furthermore, as aforementioned, at high rotor speeds the jump equations developed in the previous sections break down because as the power absorption rate increases a significant amount of mass leaves the jump as vapor. Incorporating these effects in a toroidal geometry would be a highly formidable task, and would most likely lead to impractical dynamometer designs.

Conversely, a high speed flow can be developed in a practical and controllable way that is capable of absorbing substantial amounts of power through wall shear stress induced dissipation, while minimizing blade incidence losses and cavitation erosion. Therefore, the dynamometer blading will be developed in a way that produces a recirculating liquid flow in which wall shear stress induced dissipation acts as the primary power absorption mechanism.

CHAPTER 3

Development of Dynamometer Flow Model

3.1 Basic Flow Model

Power absorption mechanisms were investigated in the previous chapter, and the shear induced dissipation mechanism was determined to be most consistent with the basic objective of the work presented in this thesis. In this chapter a flow model is developed for the helically recirculating flow dynamometer based on the shear stress induced dissipation mechanism. The flow field in the toroidal dynamometer is clearly very complex and it would be extremely difficult to precisely model a centrifugally accelerated, helically swirling, two-phase free surface flow. Instead, the intent here is to develop a basic model that embodies the fundamental characteristics of the flow, which can be used to make performance estimates.

There are several important features that must be included in the model. Clearly, the speed of the flow (or Reynolds number) is very important, as well as how the flow is accelerated to a steady operating speed. The volume of liquid recirculating around on the inside surface of the torus is also very important, as well as the determination of the appropriate wetted surface area. Furthermore, estimating friction factors for the flow is crucial for determining both the speed of the flow and predicting power absorption. This requires that the effects of streamline curvature due to the toroidal geometry be incorporated.

To proceed with the development of a basic model recall from chapter one that the torus is divided into two sections, a rotor and a stator, which form a closed flow circuit. The liquid in the rotor stage is accelerated by the action of the rotor. The liquid flows from the rotor stage into the inlet of the stator stage, proceeds through the stator, and exits into the inlet of the rotor, thus completing a circuit. The liquid accelerates unidirectionally (by design) until a steady state speed is reached at which point the power input from the rotor equals the shear stress induced dissipation in the recirculating liquid. As power is absorbed, a portion of the recirculating liquid undergoes a phase transition which must be bled off and continually replenished with liquid feed-water to maintain steady operation. As a consequence of the strong centrifugal field, the liquid and vapor self separate, and a liquid sheet is formed on the surface of the torus. The liquid phase portion of the fluid is much denser than vapor and is by far the most significant part of the flow. Therefore, the model

is built on the concept of a recirculating liquid sheet that dissipates power (by predominantly fluid frictional drag) at a rate equal to the rotor power input.

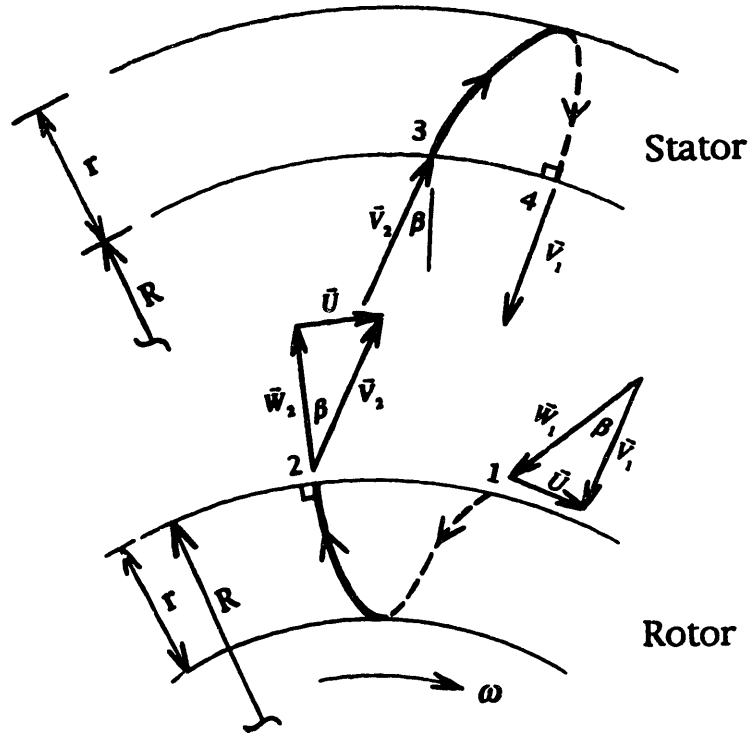


Figure 3-1. Steady state velocity vectors — rotor and stator stages

To accomplish this power balance the rotor and stator blades must have the appropriate turning angles (β), such that the steady state speed (V) of the (recirculating) fluid sheet is related to the rotor blade tip speed (U). This relation is defined here as simply a factor k (referred to as a recirculation factor) times U . Figure 3-1 shows the velocity triangles that correspond to the steady state power balance between frictional drag and rotor power input. The liquid in the rotor is accelerated and exits (at point 2) into the inlet of the stator (at point 3). The liquid flows through the stator and exits (at point 4) into the inlet of the rotor (at point 1). The flow continues to accelerate until the power dissipated in the recirculating fluid (by frictional drag) is equal to the rotor power input. Then, by design the steady state change in tangential velocity between rotor inlet and outlet is equal to U . The turning angle

of the blades (β) is related to the recirculation factor (k), and can be calculated from Equation 3.1 below.

$$\beta = \tan^{-1}\left(\frac{U}{V_1}\right) = \tan^{-1}\left(\frac{1}{k}\right) \quad (3.1)$$

Since the flow path is closed on itself, and both U and V_1 are direct functions of ω , a fixed turning angle (and hence recirculation factor) can be determined so that the velocity triangles remain approximately similar over a wide range of rotor speeds. The main objective here is to design the blades so that the fluid exits the stator blades at the correct rotor blade inlet angle, and similarly exits the rotor stage at the correct stator inlet angle. To accomplish this, the correct blade turning angle for both rotor and stator blades should be equal to β as defined above. Clearly, the recirculating mass flow rate in the torus, as well as the momentum and energy exchange between the rotor and liquid, must all be related to (among other things) the recirculation factor (k). These relationships are developed in the following section.

3.2 Power Balance Between Rotor Input and Recirculating Fluid

The liquid in the working compartment is accelerated to a steady state speed at which point the power dissipated by shear stress in the recirculating fluid, neglecting other loss mechanisms, equals the rotor power input. The liquid flow is modeled here as a *pseudo* one-dimensional flow, with the effects of the highly twisted streamlines and toroidal geometry included. The blades form channels in which the flow helically recirculates on the inside surface of the torus, see Figure 1-2 and 1-3. The recirculating mass flow rate, torque retarding the rotor, and power absorption rate, are all tied to the recirculation factor (k) of the liquid in the channels.

The torque acting on the rotor is equal to the net efflux of angular momentum from the rotor stage, and can be determined from elementary turbomachine analysis — expressed as follows.

$$T = \dot{m}(\Delta V_t)R \quad (3.2)$$

Due to the closed toroidal flow circuit, the mass flowing through the rotor stage is equal to the recirculation mass flow rate (\dot{m}) which can be expressed in terms of the liquid flow cross sectional area (A_f), recirculation factor, and rotor blade tip speed (U), as in Equation 3.3 below.

$$\dot{m} = \rho A_f (kU) \quad (3.3)$$

Furthermore, A_f is equal to the product of the number of blades (N), the flow width or spacing between the blades (s), and the liquid sheet depth or wetted blade height (h_w). From Figure 3-1 it is clear that the change in tangential velocity is simply equal to the rotor blade speed, and the radius at which the flow enters and exits the rotor is the torus major radius (R). Thus, Equation 3.2 can be re-written as follows, where the term in parenthesis is the recirculating mass flow rate.

$$T = (\rho A_f kU)UR \equiv (\rho Nsh_w kU)UR \quad (3.4)$$

The torque times the rotor speed (ω) is the power input to the fluid through the rotor, which can be expressed in terms of the machine parameters defined above.

$$P_{rotor} = T\omega \equiv (\rho Nsh_w kU)UR\omega \quad (3.5)$$

Since ω is simply the blade tip speed (U) divided by R , Equation 3.5 can be expressed more succinctly as follows.

$$P_{rotor} = T\omega \equiv (\rho Nsh_w kU)UR \left(\frac{U}{R} \right) = \rho Nsh_w kU^3 \quad (3.6)$$

At steady state, the rotor power input must be equal to the power dissipated by the fluid, which is equal to the drag force (F_d) times the flow speed (V), neglecting other losses. The flow speed is (approximately) the recirculation factor times the blade tip speed. Thus the absorbed power can be written in terms of these parameters, a friction coefficient or factor (C_d) and the wetted surface area (A_s), as in Equation 3.7.

$$P_{dissipated} = F_d V = \left(\frac{1}{2} \rho C_d A_s V^2 \right) V \equiv \frac{1}{2} \rho C_d A_s (kU)^3 \quad (3.7)$$

The wetted surface area is simply the product of the total fluid path length through the rotor and stator stages, the number of blades, and the wetted perimeter of the channels. However, the dimensions of the channel change as the fluid travels around the flow circuit due to the toroidal geometry. Therefore, the flow circuit must be broken down into (n) sub-sections, with the wetted surface area (A_i) and friction factor (f_i) individually evaluated for each sub-section (or locality). Incorporating this into Equation 3.7 yields the following expression for the dissipated power.

$$P_{dissipated} \equiv \frac{1}{2} \rho (kU)^3 \sum_{i=1}^n f_i A_i \quad (3.8)$$

By design, the steady state power dissipated in the dynamometer by frictional drag (Equation 3.8) is equal to the power input by the rotor (Equation 3.6). Canceling terms reduces this equality to a simple form.

$$Nsh_w \equiv \frac{1}{2} k^2 \sum_{i=1}^n f_i A_i \quad (3.9)$$

The fluid recirculation factor (k) that equates rotor power input with shear stress induced dissipation can be determined from Equation 3.9. However, the local friction factor (f_i) is a function of (among other parameters) k , which makes the equation non-linear. Therefore, Equation 3.9 is best solved iteratively using a computer. An iterative procedure is described in Chapter 6, where a numerical code is presented that was developed based on the model described here. But first a method for predicting the (local) friction factor for the liquid flow is presented.

3.3 Friction Factor Prediction & the Effect of Streamline Curvature

There is no known formula or empirical correlation to accurately calculate the friction factor for this highly twisted, free surface, turbulent recirculating flow. This could only come through the testing of machines that operate on the principles set forth in this thesis. Since there are no known machines like this, there are no experimentally generated correlations to use. Instead, friction factors are predicted here in a way that is consistent with the flow model developed above, with the toroidal geometry and effects of streamline curvature incorporated.

Recall that the liquid flow through the rotor and stator stages is effectively a channel flow, with the blades forming the sides of the channels. Clearly, the friction factor for this flow is proportional to the shear stress acting on the wall (τ_w) and, from dimensional analysis, has a functional form as follows where ε is the surface roughness, d_h is the hydraulic diameter of the channels, and r_c is the radius of curvature of the mean streamline.

$$f \propto \frac{\tau_w}{\rho V^2} = f(\text{Re}, \varepsilon/d_h, d_h/2r_c) \quad (3.10)$$

To get tangible numbers, a reasonable starting point for approximating the friction factor is the Moody diagram, which presents data for f as a function of Reynolds number and relative roughness (ε/d_h). The Moody diagram is for fluid flow through straight fully wet conduits, but can be used to obtain reasonable approximations for partially filled conduits. To include the secondary flow effects that result from the streamline curvature, the following correlation from *Rohsenow and Choi* [6] can be used to modify the friction factor predicted for flow through straight fully wet conduits.

$$f_{\text{mod}} = f \cdot \left[\text{Re} \cdot \left(\frac{d_h}{2r_c} \right)^2 \right]^{1/20} \quad (3.11)$$

This relationship is for a fully wet conduit that is helically twisted, but again can be used to obtain reasonable estimations for friction factors in partially filled conduits, where r_c is the approximate helix radius of the mean streamline.

To summarize, the Moody diagram in conjunction with Equation 3.11 provides a means of estimating the shear stress induced friction factors in a way that satisfies the functional relation in Equation 3.10. This technique is used to evaluate Equation 3.9 in the dynamometer flow code (developed in Chapter 6) but first an algorithm to create blades that have the appropriate turning angle (β) is presented in the next chapter.

CHAPTER 4

Blade Generation Algorithms & Programs

4.1 Overview

The rotor and stator turning angles (β) are defined by the recirculation factor (k), which is determined from the power balance developed in the previous chapter. The next step is to determine blade profiles that have the correct turning angles. These profiles define the base of the rotor and stator blades, and will thus be referred to as Base curves. This is broken down into two steps. First, a reasonable planar (2-D) curve is selected that can make the liquid flow smoothly through the correct turning angle. This 2-D curve is called a Trace curve, which would exactly define the profile if the flow was planar. But since the flow is clearly three dimensional, the Trace curves must be transformed into the appropriate coordinates. Therefore, the second step is to transform the Trace curve into cylindrical, and ultimately toroidal, coordinates which define the rotor and stator Base curves that lay on the surface of a torus. Then, an Inner curve is developed that together with the Base curve (i.e., connected by a surface) define the centerline (or basic shape) of the blades, as shown in Figure 4-1.

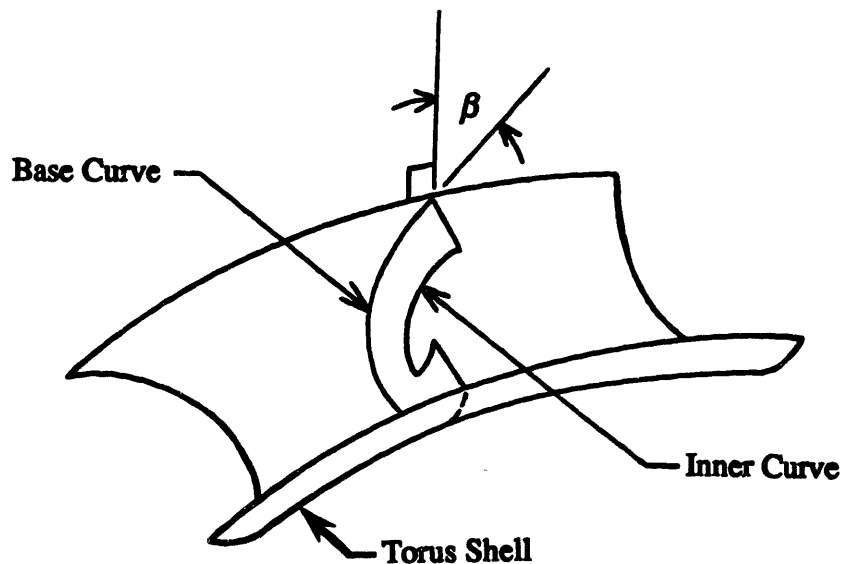


Figure 4-1. Centerline of blades defined by Base and Inner curves

The blades must be oriented in a way that keeps the liquid in the channels (formed between any two blades). That is, the blades must have the correct rake angle (ψ , defined in Figure

1-3) at each point along the flow path to keep the free surface of the liquid perpendicular to the blades, just as a roller coaster track must be banked properly to keep the car's wheel force perpendicular to the track. For the stator this is done by determining the direction of principle curvature, at each point along the flow path, and orienting the blades in this direction. The rotor blades are more complicated to account for the acceleration terms associated with its rotation. Therefore, the rotor blades are oriented parallel to the total acceleration vector of the fluid particles, instead of in the direction of principle curvature. The result is the same, the free surface of the liquid in the channels is kept approximately perpendicular to blades as the fluid turns through the prescribed angle (β).

4.2 Base Curve Development

The first step in the blade generation process presented here is the development of a Base curve. To accomplish this, a planar (or Trace) curve is specified that has the appropriate turning angle (β), such as a circular segment cut at the correct point. Then the planar curve is transformed, or mapped, onto the surface of a cylinder. Next, the cylindrical curve is transformed into toroidal coordinates, where the resulting space curve is the Base curve. This scheme is pictorially represented in Figure 4-2, where r is the toroidal minor radius.

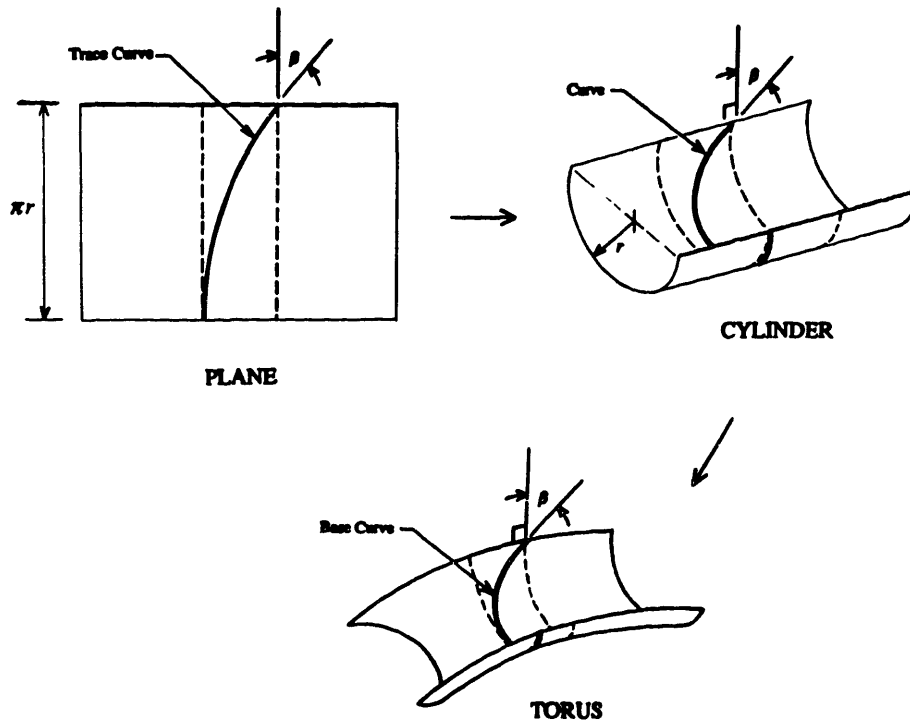


Figure 4-2. Pictorial representation of Base curve development scheme

Any planar curve that guides the liquid flow through the correct turning angle (β) can be chosen as the Trace curve and defined in terms of Z_o and S coordinates (where Z_o and S are dummy variables to be eliminated by transformations). Since this is a planar curve the rotor and stator Trace curves are the same, except that they are complimentary, or 180° reversed. As alluded to above, the Trace curve selected here is a circular segment of radius (a) centered at the origin, which can be described by Equation 4.1.

$$Z_o^2 + S^2 = a^2 \quad (4.1)$$

More specifically, the Trace curve is defined as the segment of this circle that produces the correct turning angle (β). To achieve this, consider another variable Z whose axis is parallel to the Z_o -axis. The Z -axis is positioned a distance (L) to the right of the origin such that the angle between the line tangent to the circle (at the intersection point) and the Z -axis is equal to β , as shown in Figure 4-3.

The parameters needed to describe the Trace curve can be computed from Equations 4.1 through 4.4, where (r) is the radius of a cylinder that corresponds to the minor radius of the torus, which will (together with R the major radius) define the dynamometer's working compartment. Equation 4.2 (on the following page) defines the maximum value of S which clearly must correspond to one half the minor circumference of the torus in order to

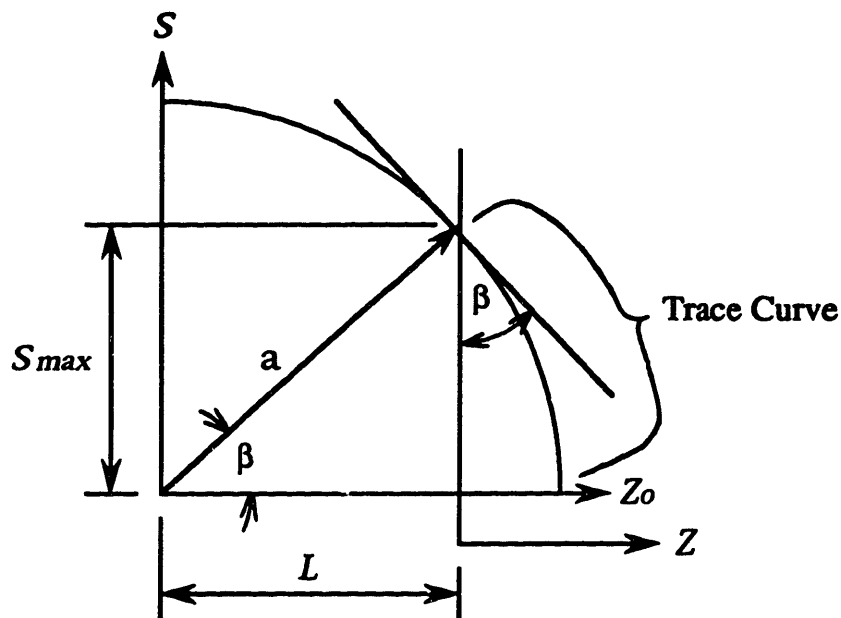


Figure 4-3. Trace curve specification in Z_o - S plane

have a Trace curve that is transformed onto this cylindrical surface. In Equation 4.3 and 4.4 the variables a and L are defined by the geometry of the Trace curve, defined above.

$$S_{max} = \pi r \quad (4.2)$$

$$a = S_{max} / \sin(\beta) \quad (4.3)$$

$$L = a(\cos\beta) \quad (4.4)$$

Next, the Trace curve is transformed into cylindrical coordinates, such that it lays on the surface of a half cylinder. The transformation equations developed to accomplish this are as follows (Equations 4.5 through 4.8), where X , Y , and Z are the Cartesian coordinates of a point that lays on the cylindrically transformed Trace curve. The X - Y origin is located at the upper left hand point on the half cylinder on which the Trace curve is wrapped, and ζ is the polar angle to a point on the cylindrically transformed Trace curve, as shown in Figure 4.4 (a).

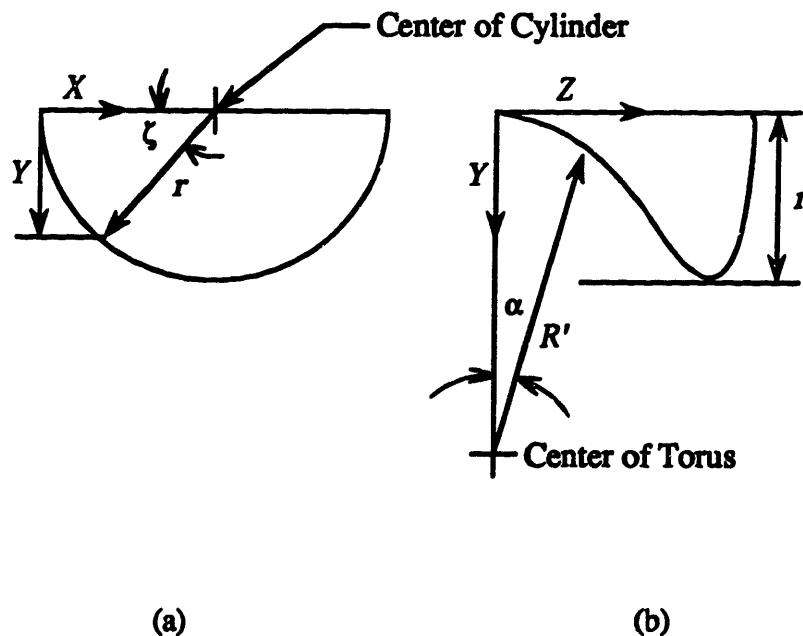


Figure 4-4. Cylindrical coordinate system

$$S = \zeta r \quad (4.5)$$

$$X = r(1 - \cos \zeta) \quad (4.6)$$

$$Y = r(\sin \zeta) \quad (4.7)$$

$$Z = \sqrt{a^2 - S^2} - L \quad (4.8)$$

In these equations ζ is the independent variable, and since they define a cylindrical space curve they can be used for both the rotor and stator.

The next step is to transform the Trace curve from cylindrical to toroidal coordinates. This transformation can be thought of as wrapping the cylinder to an extent such that the center of curvature is the center of the torus. The radius from the center of the torus (R'), and angle (α) to a point on the curve are defined as in Figure 4-4 (b), and can be expressed in terms of the cylindrical variables Y , and Z as follows, where R is the torus major radius.

$$R' = R - Y \quad (4.9)$$

$$\alpha = \tan^{-1}\left(\frac{Z}{R'}\right) \quad (4.10)$$

Then, the equations needed to transform the cylindrical Trace curve into toroidal coordinates, which define the Base curve, are straight forward and are written below (for the rotor) where Y and Z (to calculate α) are used as the independent variables.

$$X' = X \quad (4.11)$$

$$Y' = Y + R'(1 - \cos \alpha) \quad (4.12)$$

$$Z' = R'(\sin \alpha) \quad (4.13)$$

Now, the blade Base curve (which lays on the surface of the torus) can be defined in terms of the Cartesian coordinates X' , Y' , and Z' , using Equations 4.9-4.13, where (0,0,0) is at

the center of the torus. These equations are for the rotor, but it is a trivial matter to adjust them for the stator which therefore will not be presented here. This algorithm was invoked to develop a FORTRAN code (see Appendix B.1) that can be used to generate rotor and stator blade Base curves, from which the Inner curves are developed.

4.3 Inner Curve Development

The third part of the blade generation algorithm is the development of the Inner curves which, when joined by a single curved surface to the Base curve, form the centerline (or center-surface if you will) of the blade, see Figure 4-1. As aforementioned, the objective here is to form blades that act as the walls of channels in which the liquid flows. This can be accomplished by orienting the blades in such a way that they are perpendicular to the free surface of the liquid. For the stator this is done by orienting the blades in the direction of principle curvature, which can be determined strictly from geometry. However, the rotor blades are more complicated due to the angular motion of the rotor, and therefore must be oriented parallel to the local total acceleration vector of a fluid particle.

A stator blade generation algorithm was developed that can generate the appropriate Inner curve and is presented first since it requires only knowledge of the geometry. The method developed here uses differential vector calculus, so the first step required is to discretize the Base curve. Next, the discretized Base curve is put into vector notation (\vec{v}) referenced to a local origin and a directional vector (\vec{d}), from point to point on the Base curve, is determined that corresponds to the flow direction as shown in Figure 4-5.

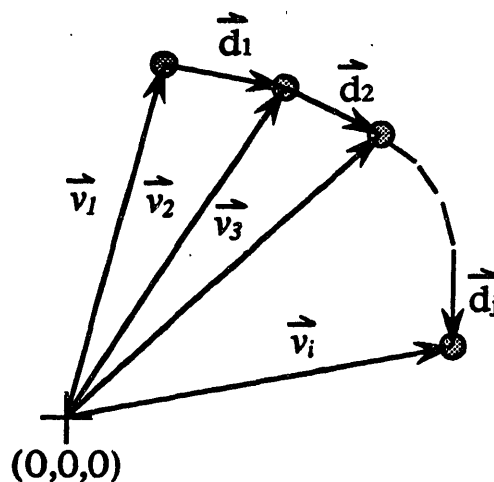


Figure 4-5. Discrete Base curve and directional vectors

The directional vector is simply the vector difference between any two successive Base curve vectors, and can be computed as follows where the subscripts indicate a particular vector.

$$\vec{d}_j = \vec{v}_{i+1} - \vec{v}_i \quad (4.14)$$

From this, the local unit direction vector (\vec{D}_u) can be determined at each point along the Base curve, and used to calculate a local curvature vector (\vec{c}).

$$\vec{c}_k = (\vec{D}_u)_{j+1} - (\vec{D}_u)_j \quad (4.15)$$

Then, the local unit curvature vector (\vec{C}_u) can be calculated and used to determine the location of the points that comprise the Inner curve (where \vec{I} is relative to the same previously defined origin), which together with the Base curve define a stator blade that is oriented in the direction of principle curvature at every point along the flow path in the stator stage.

$$\vec{I} = \vec{v} + h \cdot \vec{C}_u \quad (4.16)$$

The correct multiplier (h) in Equation 4.16 is the height of the stator blade. This algorithm was used to develop a *MathCAD* program to generate the Inner curve for stator blades, which is included in Appendix B.2.

The rotor blade Inner curve generation scheme is the same as that for the stator up to Equation 4.14. Then, instead of computing the direction of principle curvature, the local total acceleration vector must be determined. The technique developed here requires a Lagrangian analysis of a fluid particle traveling along the rotor Base curve. The velocity of a fluid particle in the rotor stage can be written in the following vector form, where \vec{V} is the absolute velocity, \vec{W} is the relative velocity, and $\vec{U}(r_o)$ is the blade tangential velocity which is a function of r_o (the radius from the center of rotation to any particular point on the Base curve).

$$\vec{V} = \vec{W} + \vec{U}(r_o) \quad (4.17)$$

The relative velocity is approximately equal to the recirculation velocity which can be written as follows, where ω is the rotor angular speed, $\vec{U}(R)$ is the blade tip tangential velocity, and r_o is equal to R (the torus major radius).

$$\vec{W} = \vec{D}_u |\vec{W}| \cong \vec{D}_u |k\vec{U}(R)| = \vec{D}_u \cdot (kR\omega) \quad (4.18)$$

The local blade speed is calculated using the radius (r_o), as in Equation 4.19, where (\vec{i}_o) is a tangential unit vector in the direction of rotation.

$$\vec{U}(r_o) = \vec{i}_o \cdot (r_o \omega) \quad (4.19)$$

Next, an absolute acceleration vector (\vec{A}) is calculated at each point by taking the Substantial derivative of \vec{V} , which can be decomposed into a magnitude (V_m) and unit vector (\vec{V}_u), as in Equation 4.20 below.

$$\vec{A} = \frac{D}{Dt} \vec{V} = \frac{D}{Dt} (V_m \cdot \vec{V}_u) = \left(\frac{dV_m}{dt} \right) \cdot \vec{V}_u + V_m \cdot \left(\frac{d\vec{V}_u}{dt} \right) \quad (4.20)$$

With the appropriate approximation for dt (i.e., based on the design point operating speed, $\Delta t \approx \Delta x / V_m$), Equation 4.20 can be numerically evaluated. Then the unit total acceleration vector (\vec{A}_u) can be computed and used to determine the points that define the rotor blade Inner curve that, together with the rotor Base curve, define blades that are parallel to the total local acceleration vector at each point along the flow path in the rotor stage. Computationally, this step is the same as shown above for the stator (Equation 4.16), but with \vec{A}_u in place of \vec{C}_u . This algorithm was used to develop a *Math CAD* program that can be used to determine the Inner curve for rotor blades (which is included in Appendix B.2).

CHAPTER 5

Flow Visualization Experiment — Linear Blade Cascades

5.1 Objectives and Overview

The main objectives of the flow visualization experiment were to verify the blading algorithm by directly observing flow through the blades, and to provide insight into the flow behavior as several important parameters are varied off the design point. In other words, would water flow through the blades and exit at a specific angle (i.e., the blade angle), while maintaining a free surface perpendicular to the blades? Once this question was answered, then the impact of parameter variations on flow behavior were evaluated. The parameters that were varied in the experiment are listed as follows: Recirculation factor (k), jet velocity, nozzle offset from blades (d), nozzle angle relative to blade inlet (θ), and blade leading edge shape (blunt or sharp).

This was carried out using two *pseudo* linear blade cascades, each consisting of several blades with different recirculation factors ($k=2$, and $k=3$, which corresponds to a β of 27° and 19° respectively). The linear blade cascades can be thought of as a section of the stator that has been unwrapped from a torus into a cylinder. The raw data for the blades was generated using the algorithms developed in Chapter 4, and was fed into a CAD program that interfaced with a Stereo Lithography rapid prototyping system, from which two epoxy-resin linear blade cascades (or cylindrical Test Sections) were produced. A nozzle was constructed that produces a square jet to supply high speed water to the blade cascades. Furthermore, a Test Set was designed and constructed to conduct this experiment which is described below.

5.2 Experimental Set-Up

The flow visualization experimental apparatus is comprised of a Test Set, nozzle, and the blade cascades, or Test Sections. The Test Set consists of a frame, water supply and return system, reservoir, drainage hoses and pumps, and a Test Bed upon which the controlled tests were executed. The Test Set frame, Test Bed, and Test Section Stand, are constructed out of wood which is mounted on a foundation comprised of standard cinder blocks. The frame houses a water collection tank (or reservoir) to catch the return water (or effluent)

from the Test Section. Figure 5-1 is a profile view of the Test Set and nozzle. The pressure gauge shown in the figure was used to determine the speed of the jet produced by the nozzle.

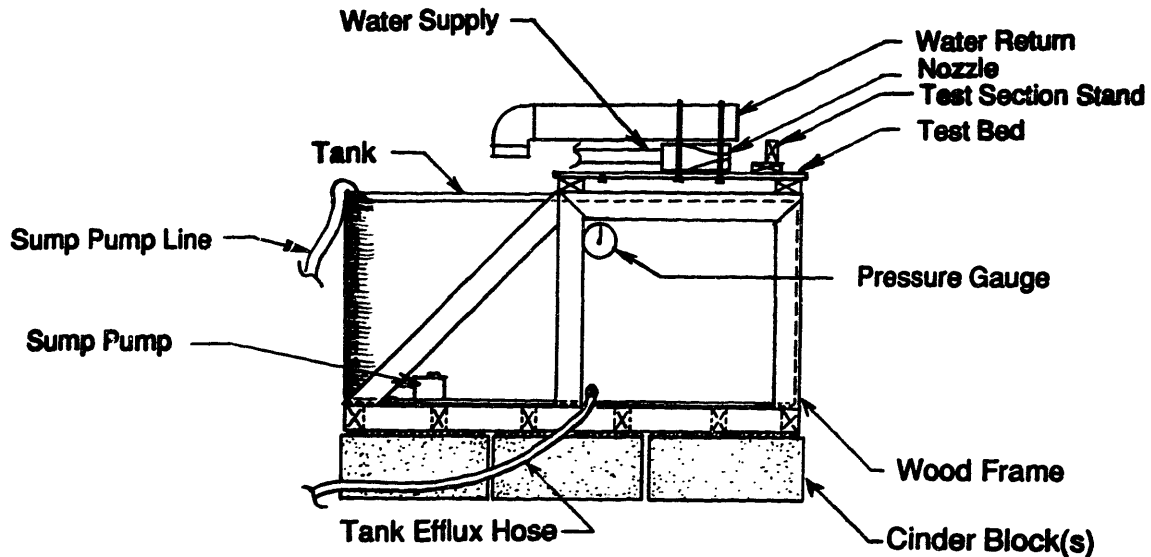


Figure 5-1. Profile view of the Test Set and nozzle

The nozzle produces a high speed square jet from a high pressure circular inlet, which was constructed out of clear cast acrylic, and is reinforced with a metal frame. To get the desired nozzle shape, a metal mold was fabricated and used to *heat form* acrylic sheets. The pieces were then machined and bonded together with cement. The metal frame was designed to make the nozzle strong enough to withstand the high pressure. Two taps were bored into the back plate of the nozzle, one for pressure readings and the other for a catheter dye injection system. The water supply was city water at approximately 70 *psi*, connected by a flexible rubber hose to the nozzle with a circular diameter of 1.25 inches. The square nozzle outlet is 2.375 inches wide by 0.25 inches thick.

The relative inlet angle between the nozzle and the linear cascades (θ) is varied by pivoting the Test Section Stand, which rotates about its center. The convention for angular displacement is positive for clockwise rotations as shown in Figure 5-2. Of course, the angular displacement is limited by how much the nozzle is offset (d) from the stand. The linear offset scale can be easily identified in the figure.

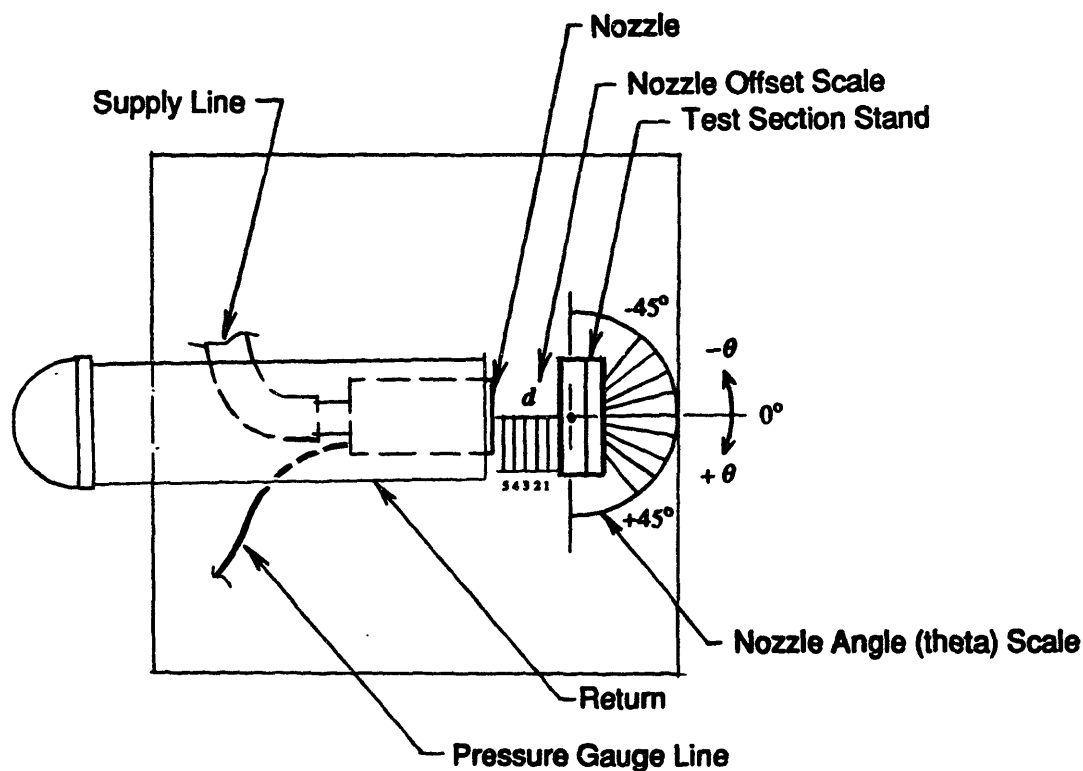


Figure 5-2. Test Bed showing nozzle angular displacement and linear offset scales

The return system, which catches water jetting out of the blade cascade, is a large cylinder made out of clear cast acrylic, with an elbow at the end to direct the effluent into the tank. Having a clear return system made it easy to directly observe the flow coming out of the blade cascades (i.e., Test Sections). The water in the reservoir was drained by sump pumps and a gravity driven hose.

Two Test Sections were fabricated (by Stereo Lithography), one has blades with a recirculation factor (k) of two, while the other has blades with a k equal to three. The blades were designed with the algorithms described in Chapter 4, except that the Trace curve was not transformed into toroidal coordinates, but instead was left in cylindrical coordinates. They both have a 1.5 inch cylindrical radius, with 0.5 inch height blades that are spaced 0.75 inches apart. The blades are 1/8 of an inch thick, so that they are structurally rigid enough to withstand the fluid loading of the high speed jet.

5.3 Test Results

The experiment was conducted as a sequence of procedures, each one designed for a particular task. The individual procedures are not described here, but are included in Appendix A, as well as raw data from the experiment. Fortunately, the apparatus performed without any major component failures, so all the procedures were executed without interruption or modification of the apparatus. The results of the experiment were quite astonishing. Not only did the experiment substantiate theoretical predictions, but it revealed that the algorithm produced blades that are very robust with respect to parameter variations.

The first task was to verify the flow near the design point. The blades are designed for a water jet that enters at a particular angle and speed, flows through the stage, and exits after being turned a number of degrees (β). With the nozzle oriented in the appropriate direction the flow was turned on to an intermediate level. The flow behaved very well. Water flowed through the blades in the anticipated manner, with a free surface approximately perpendicular to the blades. Furthermore, the water exited the linear cascade at the appropriate angle. Changing the jet speed, over a wide range (1-12 m/s), had little impact on the behavior of the free surface and outlet angle (β). The flow remained organized and exited at the correct angle. However, at higher speeds the wave produced by the leading edge of the blades was slightly larger and the flow more turbulent. But the radial pressure gradient also increases with speed, so disturbances were very quickly dissipated and erratic flow drawn back into the main stream. Two of the blades were sharpened, while the others had round edges. Not surprisingly, the blades with sharp leading edges performed better, and produced smaller waves. The effect of the different recirculation factors on the flow behavior was observed to be minimal. Although the blade cascade with the higher recirculation factor ($k=3$) blades did perform slightly better than the $k=2$ cascade, predominantly because β is smaller (by approximately 8°).

The next task was to vary the input parameters off the design point so that the blade design robustness could be gauged. First, the nozzle offset (d) was varied between a flush mount and a 10 cm gap. As the nozzle offset gap increased the jet expanded (or spread out), but once it entered the Test Section it re-collapsed into a more organized flow due to the presence of the strong centrifugal field. Even at a 10 cm offset the flow would reorganize

in the Test Section and exit vectored in the correct direction. At higher speeds the jet spread out more, but also re-collapsed faster once in the Test Section.

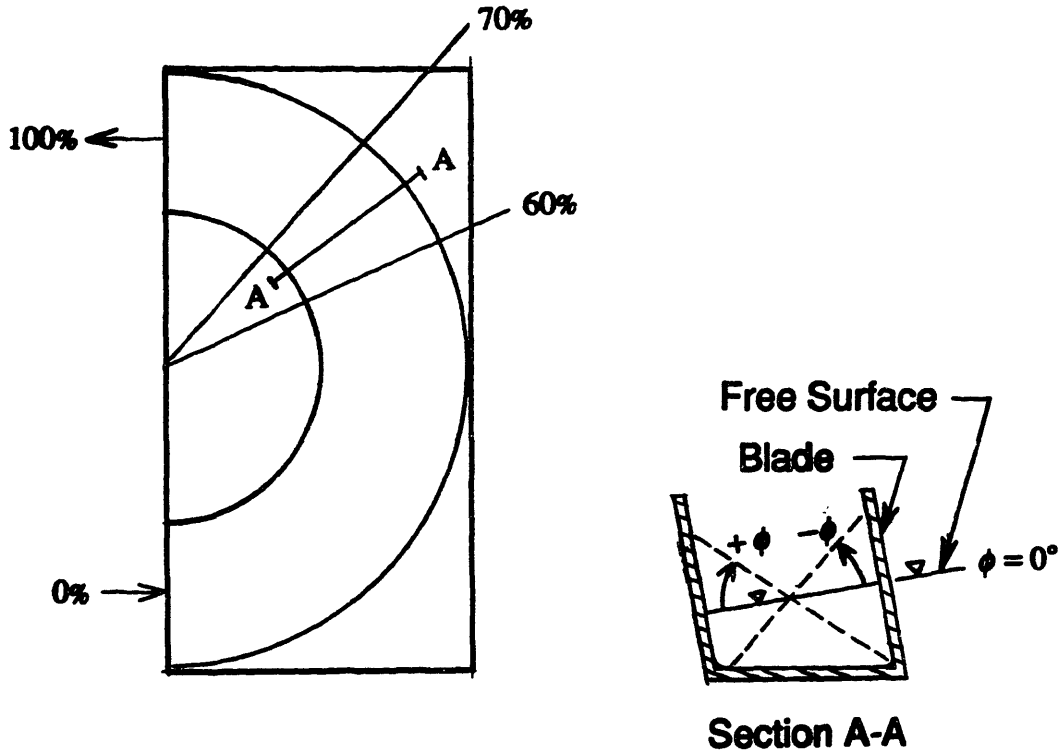


Figure 5-3. Test Section profile and free surface angle convention

The robustness evaluation continued by exploring how the flow changed as the relative nozzle angle was varied. For this set of procedures the nozzle was given just enough offset to permit the Test Section to swivel (or pivot) about the origin by plus or minus 40 degrees. As the nozzle angle was varied the free surface angle (ϕ) of the flow relative to the blades would also vary. The free surface angle convention is pictorially represented in Figure 5-3. Surprisingly, the flow remained intact as the nozzle was varied over the full range, but with appreciable cross blade overflow at plus or minus 40 degrees. The blade overflow occurs predominantly in the 60-70% region, shown in Figure 5-3, where the flow enters at 0% and exits at 100%. In the 0-60% region the flow steadily banks up to the point of overflow. Conversely, in the 70-100% region the flow gradually banks down (although not entirely) before exiting. The flow was very well behaved for nozzle angular

displacements (θ) up to approximately plus or minus 15 degrees, with no overflow and a maximum free surface angular displacement (ϕ) of plus or minus 25 degrees. The flow was still reasonably organized over the range θ equal to plus or minus 15-25 degrees. Between θ equal to plus or minus 25-40 degrees the flow deteriorated rapidly, banking more and more, until appreciable amounts of water overflowed the blades. Again, the sharp leading edges performed much better for these tests. Also, as in other tests, there was no significant difference observed for the two Test Sections. Furthermore, the same type of behavior was noticed as the jet speed was increased. That is, as the jet speed increased the leading edge wave increased slightly, but as with other disturbances they were quickly pulled back into the main stream flow due to the large radial pressure gradient.

The final issue to be investigated was the degree of turbulence and secondary flow induced mixing. However, the catheter dye injection system, comprised of a catheter that was snaked through the nozzle and supplied by a dye source, did not work because of large amplitude vibrations. Instead, a hypodermic needle was used to inject dye directly into the square jet, which worked quite well. For the full range of jet speeds the dye was thoroughly mixed upon exiting the Test Section. In fact, the mixing length was determined to be quite short, approximately one hydraulic diameter along the flow path (or about 3 cm here), which corresponds to the first 10% of the total flow path through the blades in the Test Section.

In summary, both Test Sections performed as expected when subjected to the correct flow conditions. However, the performance exceeded expectations for variations off the design point. In other words, the blade algorithm produces blades that are very robust with respect to parameter variations. The flow was stable for a much greater range of nozzle offset gaps and angular variations than expected, indicating they can tolerate appreciable changes in the shape of the velocity triangles. Furthermore, the highly turbulent nature of the flow and the secondary flow effects were clearly visible, which is beneficial in a dynamometer that seeks to exploit viscous dissipation.

The Flow Visualization experiment was conducted using blade cascades (in a cylindrical configuration or once unwrapped torus) which is a reasonable technique for characterizing blades. However, since the geometry in this machine is clearly toroidal, the flow through the rotor could not be accurately evaluated with linear blade cascades due to the significant acceleration effects which result from angular motion. Therefore, the important question of

whether the flow will develop into an organized recirculating flow in a closed toroidal system required further investigation. This question and several other issues are addressed in Chapter 8, which presents the design of a low-speed prototype, an experimental set-up, as well as experimental test procedures and results. But first, a numerical code is presented in the following chapter that was developed based on the flow model and blading scheme.

CHAPTER 6

Dynamometer Code Development & Performance Simulation

6.1 Overview of Numerical Program

This chapter describes the numerical code that was developed based on the basic flow model and blading programs described in Chapters 3 and 4. The code (or Dynamometer Code) can be used as a starting point to design dynamometers that develop a recirculating liquid flow, and to predict power absorption. Then, key dimensionless ratios are identified, computed with the code, and used to make performance predictions. The code can also be used for sensitivity analyses and to examine the effect of design parameter variations. Several examples are presented below.

The code was written in FORTRAN and is comprised of three parts. In the first part the rotor speed and geometric parameters are input, such as the major and minor radii, blade height, and surface roughness. The second part of the code is the iterative segment, where the parameters that are typically iterated on are input, such as the recirculation factor (k), blade thickness (t) and number of blades (N), as well as the percentage of liquid level (*%-Fill*) in the dynamometer. For each iteration the blades shapes are calculated using the scheme developed in Chapter 4. A local Reynolds number and hydraulic diameter (used to calculate the local relative roughness, ϵ/d_h) are calculated so that the local friction factors (f_i) can be determined, where the torus is broken up here into three localities (or sub-sections). The friction factors are determined as described in Chapter 3 and input to the code. Then, the wetted surface area is computed for each locality. Once this is done, the power dissipation is calculated and compared to the power input by the rotor. If they are not equal then the appropriate parameter (*usually k*) is iterated on until power is conserved. Recall from Chapter 3 that this balance is represented by Equation 3.9, which is the criterion for convergence. Finally, in the third part of the program, steady state parameters of interest are determined after which the program terminates.

In the current version of the program there are several parameters calculated. Some of the most useful parameters are the power absorption, recirculating and evaporation mass flow rates, rotor torque, and overall effective friction factor. Dimensionless parameters are also calculated by the program, or easily determined from the program output, the most significant of which are defined in the following section. A thoroughly commented version

of the dynamometer flow modeling code (or Dynamometer Code) has been included in Appendix C.1.

6.2 Key Dimensionless Ratios & Performance Estimation

There are several parameters that can be non-dimensionalized and evaluated over a wide range of input conditions using the Dynamometer Code. This section concentrates on the key dimensionless ratios that are useful for many types of analyses and performance estimations. These ratios are evaluated (over a wide range) using the code and the results examined. Then, the ratios are used to make general performance estimations for the dynamometer. The key parameters are power absorption, recirculation velocity, rotor blade tip speed (or tangential velocity), and liquid level in the dynamometer. These parameters can be non-dimensionalized by either the *Buckingham-Pi* method or inspection. However, this must be done in a way that allows useful dimensional numbers to be backed out of the non-dimensional ratios with knowledge of only easily obtainable parameters such as torus size, rotor speed, and fluid properties. This permits the dimensionless curves (presented below) to be used for making performance estimations for specific machines. With this restriction in mind the key dimensionless ratios are developed as follows.

Consider first the power absorption, or dissipation (P), which is clearly a function of fluid density (ρ), torus size (r and R), and rotor blade tip speed (U). The non-dimensional power (P^*) can be expressed in terms of these parameters as in Equation 6.1. The recirculation velocity (V) can be non-dimensionalized by using ω and the major radius (R), or simply the rotor blade tip speed (U), as in Equation 6.2. Clearly this ratio is simply the recirculation factor (k). Next, the rotor blade tip speed can be non-dimensionalized in terms of r and R , and the fluid kinematic viscosity (ν) as shown in Equation 6.3, which is like a Reynolds number. Finally, the amount of liquid in the torus can be represented as a percentage of the wet blade height (h_w) defined at the rotor hub, compared to the total blade height (h), as in Equation 6.4.

$$P^* = \frac{P}{\rho R r U^3} = \frac{P}{\rho R r (R\omega)^3} = \frac{P}{\rho R^4 r \omega^3} \quad (6.1)$$

$$k = \frac{V}{R\omega} = \frac{V}{U} \quad (6.2)$$

$$Re = \frac{Ur}{\nu} = \frac{(R\omega)r}{\nu} \quad (6.3)$$

$$\% - Fill = \left(\frac{h_w}{h} \right) \times 100 \quad (6.4)$$

Performance predictions can now be made in terms of these key dimensionless ratios. But first, machine dimensions must be selected so that the code can be executed. Therefore, let a hypothetical dynamometer be defined such that the toroidal working compartment has a 1.0 inch minor radius (r) and a 2.5 inch major radius (R), with 16 rotor and stator blades (N) that have a 0.6 inch height (h) and 3/8 inch maximum thickness (t_{max}). Also, say that the surface is finished to a 600 micro-inch roughness.

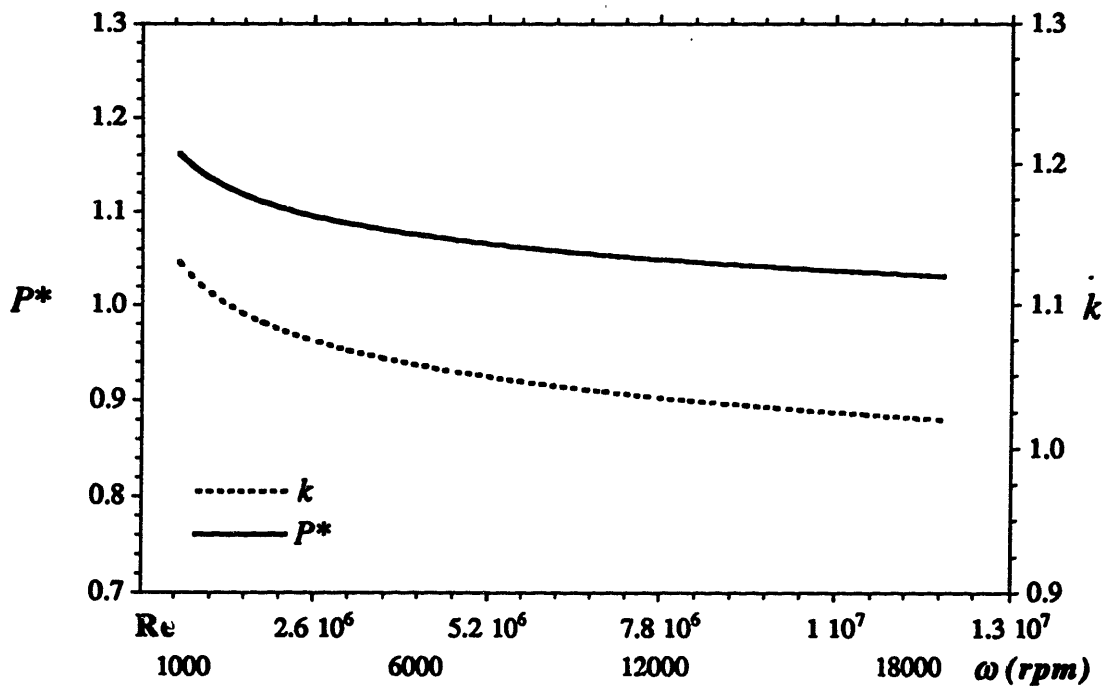


Figure 6-1. P^* and k variation with Re , for fixed $\% - Fill$

Figure 6-1 shows how the dimensionless power and recirculation factor vary as the Reynolds number (rotor speed) is increased, for a fixed $\% - Fill$ (75%). Notice that the dimensionless power and recirculation factor change very little over the entire range, which

corresponds to a rotor speed variation of $1,000$ - $20,000$ rpm. This supports the hypotheses set forth earlier that the velocity triangles remain approximately similar over a wide range of rotor speeds, and that the power was appropriately non-dimensionalized.

From Figure 6-2 it is clear that the dimensionless power increases dramatically as the liquid level in the machine is increased, at a fixed Reynolds number (corresponding to $16,000$ rpm). However, the recirculation factor rises quickly at first but then levels off somewhat to a value of approximately 1.2 . This makes physical sense since when the %-Fill is low the liquid stream inside the machine is spread much thinner over the surface.

Consequently, the hydraulic diameter of the flow in the channels is reduced and the skin friction increases (relative to the mass flow rate), resulting in higher dissipation per unit mass flow.

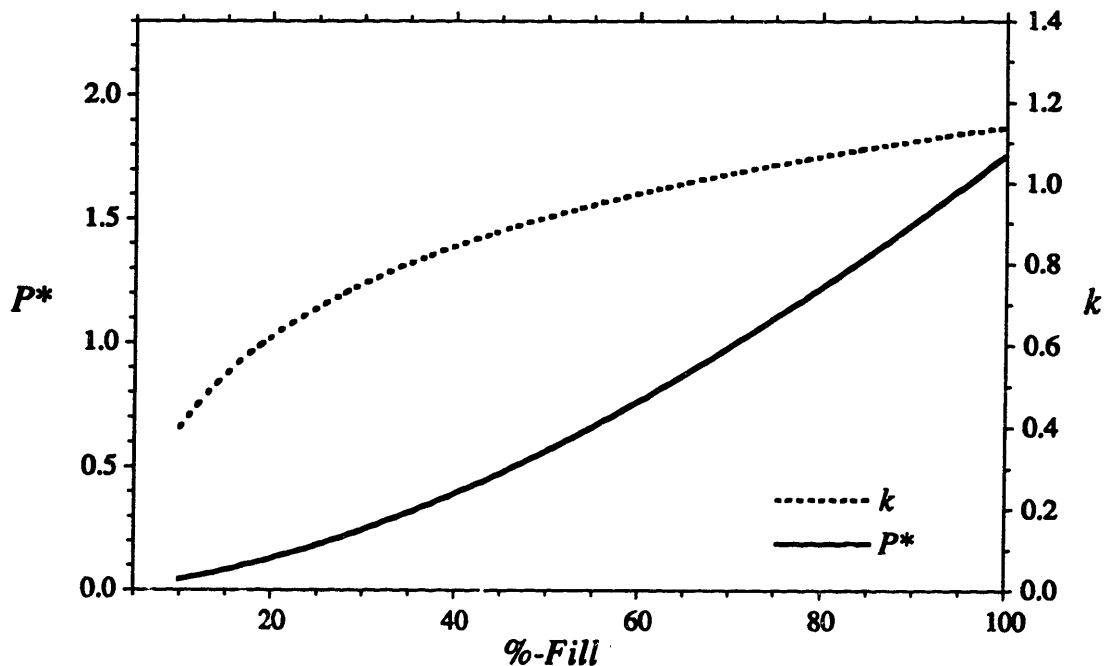


Figure 6-2. P^* and k variation with %-Fill, for fixed ω

An entire dimensionless performance map can be generated and used for making power dissipation estimates for actual machines. However, due to the highly complex and non-linear behavior of this device it is more accurate and useful to generate performance maps for particular machine designs. This has been done for the prototypes that are presented

later in the thesis. But first, the utility of the Dynamometer Code is further demonstrated by examining the effect of some parameter variations.

6.3 Parameter Variations & Sensitivity Analysis

The Dynamometer Code can also be used to study the effect of varying, and sensitivity to changes in, any input parameters. Thus, not only can the program be used to define a particular design, but variations of the design can be easily investigated as well. This is done below for three parameters; the blade thickness, number of blades, and the surface roughness. Again, in order to execute the program a machine must first be defined and a design point selected. For convenience the machine geometry of the hypothetical design presented in the previous section is used, with a design point rotor speed of *16,000 rpm* and fill level of *75%*.

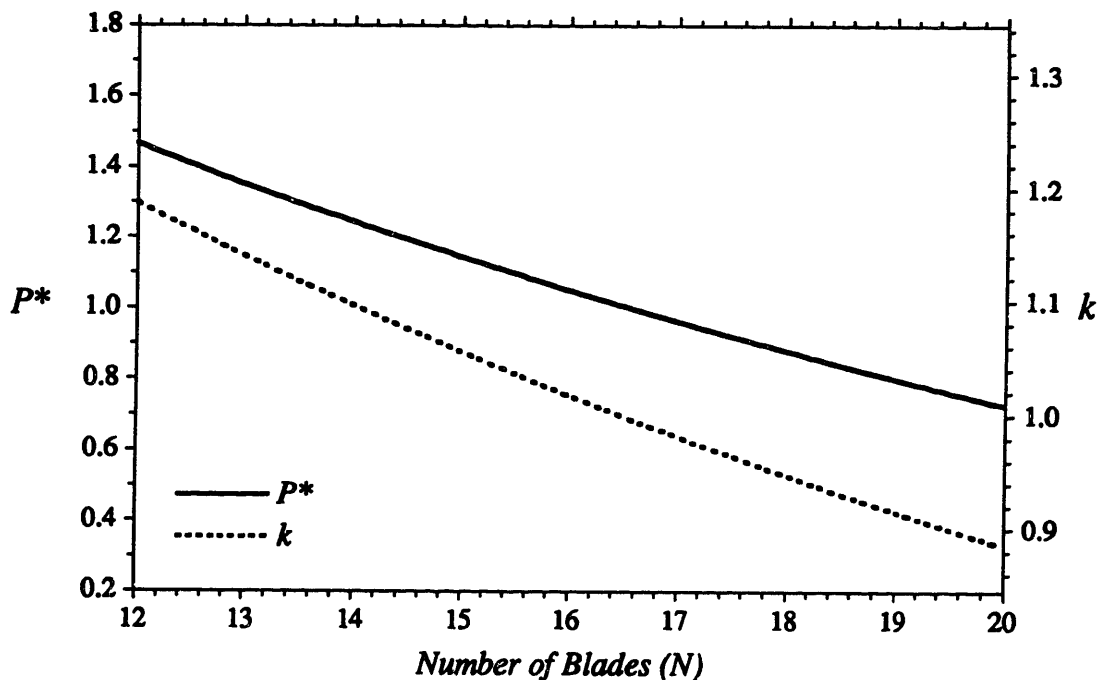


Figure 6-3. P^* and k variation with N , with all other parameters held constant

First consider a variation in the number of rotor and stator blades (N). By design the machine has 16 blades in each stage. Using the program the dimensionless power and

recirculation factor are determined to be 1.08 and 1.02 respectively. Figure 6-3 shows how these parameters change as the number of blades is changed. Clearly, adding more blades reduces the recirculation factor and power absorption. This is intuitive since the shear surface area is increased while the flow cross sectional area is reduced, resulting in more skin friction but less mass flow through the rotor per unit liquid mass. This causes the recirculation velocity to drop and thus the power to fall as well, which is a function of the recirculation velocity cubed.

Now consider the blade thickness, where the Blade Packing ($B.P.$) is defined to be equal to the blade thickness divided by the maximum blade thickness possible (which would result in the blades touching one another at the hub). From Figure 6-4 it is clear that the power and recirculation factor change dramatically as the Blade Packing is changed. Again this is to be expected since as the $B.P.$ increases the flow through the rotor is reduced, and therefore the power absorption is decreased. Conversely, thinner blades open the channels up allowing more liquid to flow through the rotor stage, which increases the power absorption.

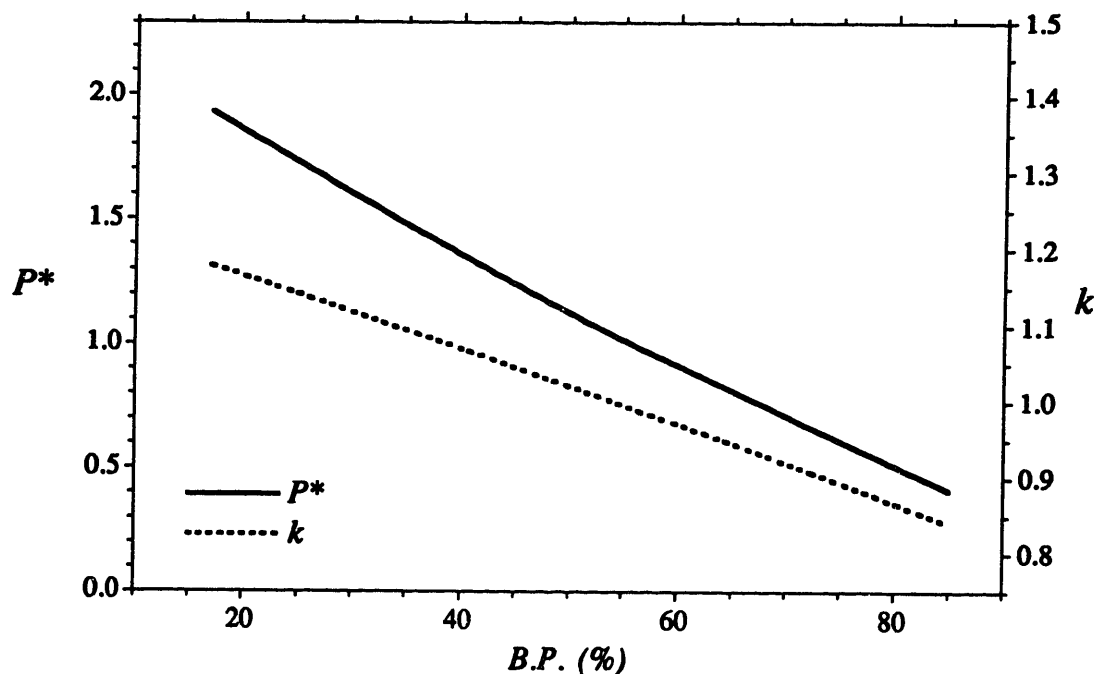


Figure 6-4. P^* and k variation with $B.P.$, with all other parameters held constant

Finally, consider the surface roughness (ε). Figure 6-5 shows how the dimensionless power and recirculation factor vary as the surface roughness is changed. This behavior is not intuitively obvious. At first, one might expect that the power absorption would increase as the surface roughness is increased since wall shear stress induced friction is the primary power dissipation mechanism. However, the power dissipation is a linear function of the friction factor but depends on the recirculation velocity to the third power. As the roughness is increased the liquid recirculation velocity decreases, due to the rougher surface, which reduced the power by the difference in k cubed. Therefore, as the surface roughness decreases the recirculation factor (k) increases and thus the power absorption also increases. This counter intuitive finding is a testimony to the very complex and non-linear behavior of the flow inside the dynamometer.

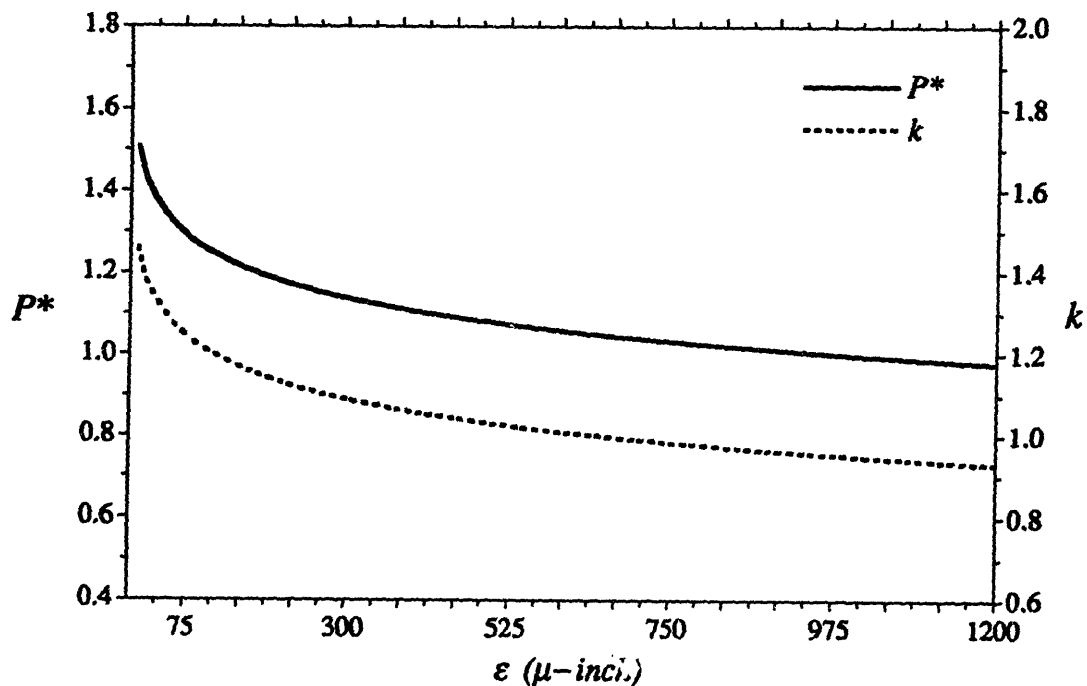


Figure 6-5. P^* and k variation with ε , with all other parameters held constant

Any parameter can be varied, as in the above examples, to determine the effect on dynamometer performance. The plots presented here are not intended to be globally

accurate for any machine, but rather their purpose is to show the trends that result from various parameter variations, and illustrate the utility of the Dynamometer Code. Clearly, the performance estimates generated from the code are only approximate at best, since the flow model (upon which it is based) is only approximate and the friction factors used are computed from correlations for fully wet conduit flow. Despite this, the general behavior and basic trends that are identified by using the code should be valid, and thus the code provides a reasonable foundation upon which to build a general dynamometer design algorithm.

CHAPTER 7

Synthesis of a Dynamometer Design Algorithm

7.1 Overview and the Design Starting Point

The Dynamometer Code, blade generation programs, as well as the knowledge gained from using the code and executing the flow visualization experiment, were used as a basis for a general dynamometer design algorithm. This algorithm was used to design a low-speed prototype which was later modified on the basis of the experimental results. The first step in the design process is the selection of a design operating point (defined by P and ω) and a machine configuration (defined by R , r , t , N , etc.). Then the surface finish, or roughness (ϵ), can be selected. From this information the design point liquid level (*%-Fill*) and recirculation factor (k) can be determined. Next, the outward pressure (p_{shell}) exerted on the torus wall must be determined, so that structural issues can be addressed. Once these parameters are defined the next task is to generate blades for the machine, after which water feed and steam ventilation schemes must be contrived. Finally, no design algorithm is complete without some scaling laws and a method for predicting performance. These issues are addressed below.

The dynamometer process starts by establishing the operating point and basic machine size. The operating point is generally known, or at least easily determined from the characteristics of the driving engine. Then, a basic machine size can be selected by picking upper and lower size limits, and iteratively converging on a rough size that meets the performance requirements using the Dynamometer Code. The machine surface roughness must be known, or selected as a design parameter. From the previous chapter it was shown that k and P are generally higher for smoother surfaces. The code can be readily used to determine ϵ , or range of values, that are suitable or desirable for the machine. Once this is done, the appropriate k can be determined. In general, it is desirable to have a recirculation factor greater than unity, but it can be less than this. However, the recirculation velocity should not be too high either or erosion might become a problem. To reduce the possibility of erosion the maximum recirculation speed should be kept below 165 m/s (based on liquid flow over a flat plate), although this is not a firm upper limit. Clearly, the high pressure resulting from the large centrifugal field acts to reduce the propensity for bubble nucleation, which tends to reduce erosion, but there is no known data for determining a precise upper limit for this highly complex flow.

There are some other criteria that must be met in selecting a design point recirculation factor (k). In order to minimize blade incidence the design point k (which defines β) should be selected so that the upper and lower extremities of the operational envelope are achieved with fluid k 's that result in a liquid flow to blade mismatch of no more than $\pm 15^\circ$ (for reasons discussed in Chapter 5). Although $\pm 15^\circ$ is desirable this range can be extended somewhat, particularly at the low end of the operational envelope.

A more important criterion is that the centrifugal force resulting from the recirculating liquid must be greater than or equal to the outward force imparted by the rotor, in the vicinity of the rotor hub, as represented by the following expression.

$$\frac{[kU(R)]^2}{r} \geq \frac{[U(R-r)]^2}{(R-r)} \quad (7.1)$$

This condition must be met over the entire operational envelope otherwise the liquid will not flow through the rotor stage but will instead get slung into the stator stage, thus preventing the evolution of an organized recirculating flow. Clearly, several iterations are required to converge on a satisfactory design point k .

To help ensure that Equation 7.1 is met, the minor radius (r) should be selected such that it is less than radius from the center of rotation to the hub ($R-r$), assuming that the velocities (or terms inside the square brackets) on both sides of the inequality are approximately the same. Once R is selected, then r can be chosen somewhat arbitrarily, but to be safe it is a good general rule to choose r so that it is at least 1.5 times smaller than the torus hub radius ($R-r$). Stated another way, once R has been selected then r should be chosen so that it satisfies the expression below.

$$r \leq \frac{R}{2.5} \quad (7.2)$$

Therefore, the radius ratio (r/R) should be no greater than 0.4 to ensure that the centrifugal force associated with the recirculating liquid is greater than the outward radial force imposed by the rotor. By examining this issue with the dynamometer code it was determined that performance improves as the radius ratio decreases. However, there are obvious limits to how far this can be taken, since as r decreases the overall volume inside

the torus decreases. Therefore, the total working volume of liquid is reduced, as well as the size of the blades, which may lead to manufacturing difficulties. Increasing R remedies this, but also makes the dynamometer outside diameter large which lowers the machine power density.

Another important issue that must be addressed is the outward pressure, acting on the torus shell, that results from the high speed recirculating liquid sheet. This can be estimated by integrating the radial pressure gradient across the liquid flow sheet, again using Euler's equation in streamline coordinates.

$$\int \frac{\partial p}{\partial r_i} = \int \rho \frac{V^2}{r_i} \quad (7.3)$$

In this flow the pressure gradients in the bi-normal and streamline directions are negligible compared to the radial component, and the velocity is assumed to be independent of r_i , so the partial differential in Equation 7.3 can be approximated as an ordinary differential, which enables the expression to be easily evaluated.

$$P_{shell} - P_{core} = \Delta p = \int_{r_i}^r dp \cong \int_{r_i}^r \rho \frac{V^2}{r_i} dr_i = \rho V^2 \ln\left(\frac{r}{r_i}\right) \quad (7.4)$$

Equation 7.4 can be used to estimate the outward pressure (p_{shell}) exerted on the torus shell

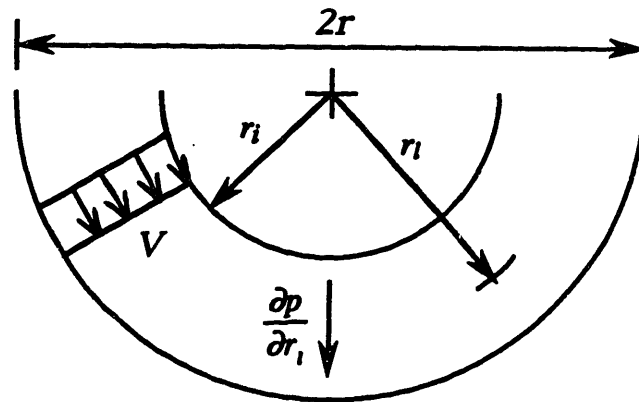


Figure 7-1. Radial pressure gradient across recirculating liquid flow

at any point around the flow circuit, where p_{core} is the vapor pressure in the torus core, r is the torus minor radius, r_l is the local radius inside the liquid sheet, and r_f is the radius to the free surface of the liquid sheet at the particular point (in the flow circuit) of interest, as shown in Figure 7-1 above.

7.2 Blade Generation, Water Supply and Steam Ventilation

The basic rotor and stator blade centerline profiles can be generated using the algorithm and programs developed in Chapter 4. The raw data produced from the programs must be modified to make actual blades. Solid body blade shapes must then be generated based on the modified raw data that are hydrodynamically appropriate and mechanically sound. Furthermore, the blades shapes must facilitate water feeding and steam ventilation by taking advantage of the centrifugally induced phase separation inside the working compartment.

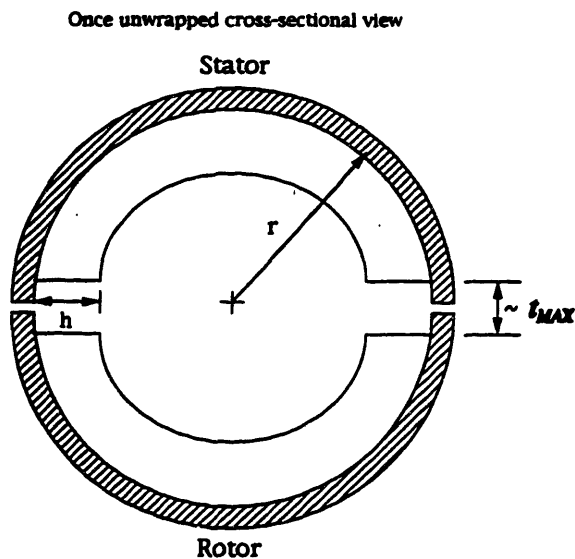


Figure 7-2. Rotor and stator blade cutback scheme

Once the machine geometry, blade height, and design operating point are established, the rotor and stator blades can be generated. To keep the amount of blade twisting at an acceptable level the blade height should be no greater than 70% of the minor radius. After the raw blade data is generated with the numerical programs, the first task (in making actual blades) is to trim back the leading and trailing edge to permit wake dissipation. Both rotor and stator blades should be trimmed back so that there is approximately one blade thickness in spacing between stages. It is best to distribute the spacing evenly between the rotor and

stator, such that both the rotor and stator blades are cut back by approximately $t_{max}/2$, as shown above in Figure 7-2. This gap should be sufficient since the large centrifugal field damps out disturbances quickly, as was seen in the Flow Visualization Experiment presented in Chapter 5.

Once this is done solid body blade shapes can be developed, in a way that produces blades that are fluid dynamically acceptable, functional, and mechanically rigid enough to withstand the large dynamic loading and centrifugal force. Consequently, the blades must be relatively thick, but with sharp leading and trailing edges like the propeller blades of a ship. This can be accomplished by tapering the first and last thirds of the blades (measured relative to both the Base and Inner curves) from the maximum thickness to a sharp edge, as shown in Figure 7-3. Also, holes can be bored through the blades, as shown in the sectional view, that are ideal for steam ventilation and make-up water supply.

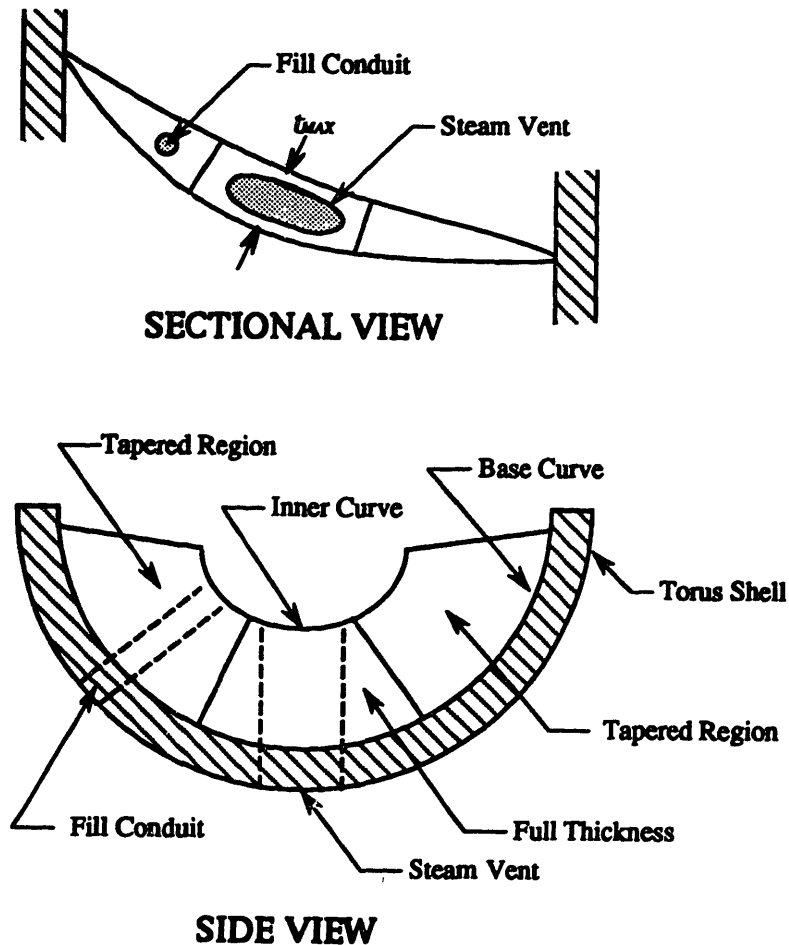


Figure 7-3. Solid body blade shapes and tapering scheme

Recall that a vapor region is set-up inside the torus, surrounded by the recirculating liquid flow. High quality (nearly pure) steam can be effectively removed through holes in the blades, which cuts down the amount of liquid effluent and thus reduces feed-water requirements. Exact calculation of the appropriate steam vent area is somewhat complex. However, one way to approximately determine the ventilation area (A) is by modeling the process as a compressible ideal gas flow through an orifice. This can be done by iteratively solving Equation 7.5, where (C) is a constant that can be evaluated with Equation 7.6, R_s and γ are properties of the steam, and \dot{m} is the steam

$$p_{core} = \dot{m} \sqrt{R_s T_{core}} / AC \quad (7.5)$$

$$C = \sqrt{\gamma(2/\gamma + 1)^{(\gamma+1)/2(\gamma-1)}} \quad (7.6)$$

mass flow rate. For a solution the stagnation temperature in the core (T_{core}) must correspond to the stagnation core pressure (p_{core}), which is equal to the saturation pressure of the steam in the torus at this temperature. Clearly, for a fixed ventilation area the only way to increase \dot{m} is to increase the stagnation core pressure. Of course, as p_{core} increases the liquid temperature also increases, which increases the propensity for erosion.

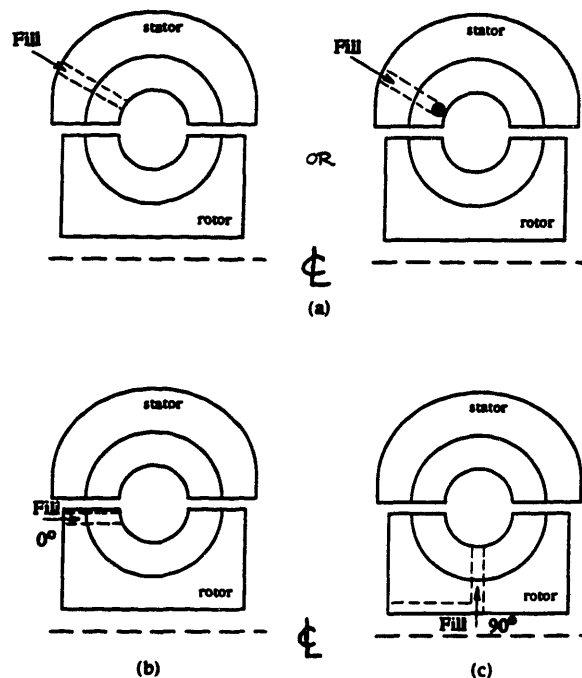


Figure 7-4. Some possible fill conduit locations

In addition to providing a means of steam ventilation the blades provide a means of pumping liquid water into the machine. Since the pressure rise across the liquid sheet is quite high it makes sense to inject liquid directly into the center of the torus where the pressure is minimal. Water can be fed in through the blades in a number of different ways. Figure 7-4 shows a few possible feed water conduit design schemes. The best scheme is represented in (a), because there are no complications due to rotating parts. The least desirable scheme is represented in (c), because of the possibility of flow instabilities due to the centrifugal pumping action produced by the spinning rotor. Furthermore, the conduits represented in (b) and (c) would require rotating seals to feed water in through the rotor. The fill conduit dimensions can be easily calculated from basic fluid mechanics, and thus will not be discussed here.

7.3 Performance Map, Scaling, and Other Design Issues

In order to make use of any dynamometer there must be a method of estimating performance over a wide range of conditions. Such a method is presented below as well as a technique for graphically representing this information. Then, other important design issues are addressed including, parameter trade-off, optimization, and off-design point estimation. Finally, some scaling laws are presented which provide a means of estimating how the size of the machine varies as other parameters are changed.

Every dynamometer selection process begins by considering the engine (or engines) to be tested. A primary requirement is that the operational envelope of the engine fall within the performance range of the dynamometer. Sizing the dynamometer for the design point was discussed above, but meeting the requirement of the design point is only part of the overall task. To be effective the dynamometer must be able to simulate load conditions over the entire performance envelope of the engine. This issue can be explored by using the Dynamometer Code to estimate performance over a wide range of conditions for a particular dynamometer, once a rough size has been determined. A performance map is a plot of power absorption versus rotor speed (ω) for different liquid levels (*%-Fill*). In other words, a performance map is a family of power-speed curves, where each curve corresponds to a particular volume of liquid in the dynamometer. Consider again the machine that was defined in Chapter 6 for the purpose of illustration. Using the

Dynamometer Code a performance map can be generated for this machine, and graphically represented as in Figure 7-5.

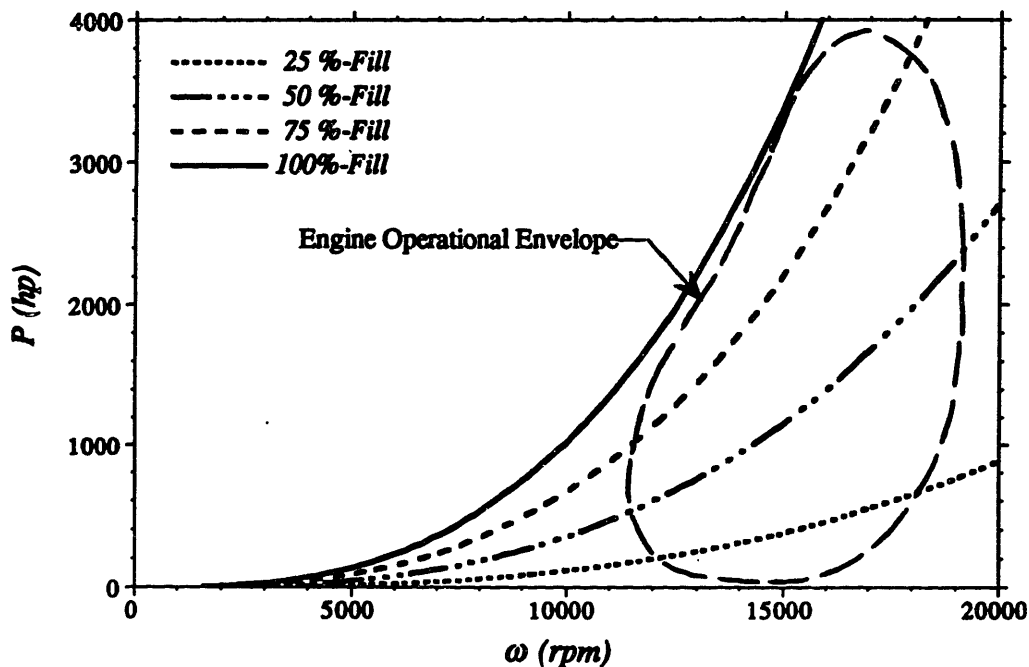


Figure 7-5. Performance map of dynamometer

The objective is to have an engine operational envelope, indicated by the closed dashed line, that falls within this region as shown in the Figure. If not, then the dynamometer design may need to be refined. Of course, these curves are rough estimates which only represent the power dissipated by solely turbulent and molecular viscous drag. There are clearly other loss mechanisms (e.g., incidence) that become significant in the low speed region of the performance map. These losses must be factored in to evaluate performance at lower (or way off-design point) operating speeds, the estimation of which can be carried out by traditional techniques. However, these other loss mechanisms are (by design) negligible over most of the performance map, and are therefore not discussed here.

There are often other issues that an engineer may want to address while designing a dynamometer, such as off-design point estimation, parameter trade-off, and optimization. The Dynamometer Code is particularly well suited to assist in these tasks. Clearly, off-design point estimations can easily be made directly from the performance map. In effect,

the dynamometer will be operating off-design most of the time, and only one point on the performance map corresponds exactly to the design point. Parameter trade-off is another task that is facilitated by the code, using the same technique introduced in Chapter 6 to study the effect of parameter variations. That is, simply change one parameter, while holding all others constant, and evaluate the outcome. Conversely, design optimization is somewhat more difficult to implement, particularly in an automated global search context (or algorithm) because of the iterative nature of the code. A reasonable approach would be to first decide what parameters are to be optimized, and define upper and lower constraints. Then, the program can be used to evaluate the performance as the particular parameter is varied between these constraints. Single or multiple variable optimization can be carried out by traditional methods. However, automation of this process, or integration with canned optimization programs, would be complicated due to the iterative nature of the Dynamometer Code, but a clever design engineer can surely resolve these difficulties.

Finally, it is often very useful to be able to estimate how one parameter will scale as another parameter is varied. Two approximate scaling laws (or trends) are presented here that were developed using the code. The first one can be used to estimate how power absorption (P) changes as the size of a geometrically similar machine is changed from (1) to (2), at a fixed rotor speed (ω). The size is represented by the outside diameter (D) of the torus (equal to $2 \cdot (R + r)$). A change in the diameter corresponds to a proportional change in other dimensions, as if the machine was being magnified, or reduced, by a certain percentage. Thus, from Equation 7.7 it is clear that the power scales directly with diameter to the fifth power. In other words, at a fixed rotor speed, the power varies with size (outside diameter) raised to the fifth power. This may seem unusual at first, but from Equation 3.7 it is clear that the power dissipation in the dynamometer is a function of the surface area (A_s), which is proportional to D^2 , and rotor blade tip speed cubed (U^3), which is proportional to D^3 . Therefore, the product is proportional to D^5 . Also, from inspecting Equation 6.1 it is clear that the power is appropriately non-dimensionalized by ρ , ω^3 , and a size term to the fifth power, which is the reason that P^* approaches a constant value as Re increases (for any fixed liquid level) as shown in Figure 6.1.

$$\frac{P_2}{P_1} \approx \left(\frac{D_2}{D_1} \right)^5 \quad (7.7)$$

The second scaling law estimates how the size (D) changes as the rotor speed is changed from (1) to (2), for a fixed power absorption level (P). From Equation 7.8 it is clear that for a fixed power, the size scales inversely with the square root of the rotor speed (ω).

$$\frac{D_2}{D_1} \approx \sqrt{\frac{\omega_1}{\omega_2}} \quad (7.8)$$

These scaling laws were developed using the Dynamometer Code, and other scaling laws can be easily developed to assist in the rapid evaluation of design changes. Clearly, these scaling laws are only valid if the physical behavior and general trends that are predicted by the flow model (upon which the code is developed) actually occur in a real dynamometer, which of course can only be verified experimentally. This is the subject of the following chapter.

CHAPTER 8

Low-Speed Prototype — Experimental Verification of Dynamometer Flow

8.1 Objectives and Overview

To investigate the behavior of the helically recirculating liquid flow an experimental low-speed prototype was designed, constructed, and tested. The prototype was developed using the general dynamometer design algorithm and programs developed previously in the thesis. The toroidal sections (rotor and stator) of the low-speed prototype are made of epoxy-resin which were produced by Stereo Lithography, in the same manner that the Test Sections for the Flow Visualization Experiment were made. The primary objectives were to verify the basic flow and general trends, obtain empirical data to compare with theoretical predictions, and explore the question of dynamic stability. Water was used as the working fluid in this experiment. There was no attempt to generate steam here due to material limitations, but instead cold liquid water was put into the working compartment and as power was absorbed the temperature of the water increased. When the temperature exceeded an acceptable limit the hot water was replaced with cold water, and the testing resumed. This technique is quite reasonable since the primary objective here was to investigate the dominant characteristics of the recirculating liquid flow.

First, a prototype was designed to meet the load requirements of a driver (i.e., an engine or motor) as presented in the previous chapter. The driver for this experiment was a direct current motor, with a maximum rated continuous shaft power output of 3 hp (2,237 Watts) at 3,000 rpm. The design point was chosen to be approximately 1 hp at 1,400 rpm. Then, a low-speed prototype performance map was generated using the Dynamometer Code. Following this, test plans were formulated, and the dynamometer and experimental apparatus constructed. Then the experiment was executed, generating data (e.g., P , ω , P_{shell} , etc.) from a multiplicity of tests. Finally, the empirical data was analyzed and compared to theoretical predictions, and some conclusions drawn.

8.2 Low-Speed Prototype Design and Performance Estimation

The general algorithm presented in Chapter 7 was used to design a low-speed prototype. After several iterations a final design was converged on, the defining parameters of which are presented below. The turning angle of the blades (approximately 29°), which is represented by k_{geo} , corresponds to the design point (1 hp at $1,400\text{ rpm}$).

Major Radius (R): 2.15"

Minor Radius (r): 0.85"

Blade Height (h): 0.50"

Blade Maximum Thickness (t_{max}): 0.1875"

Number of Blades (N): 16

Surface Roughness (ϵ): 1200 micro-inch

Geometric Recirculation Factor (k_{geo}): 1.75

Design Point Liquid Level ($\% \text{-Fill}$): 50%

The design point liquid level ($\% \text{-Fill}$) was chosen to be 50% in order to provide a wide range of power absorption levels around the design point. If the driver was an engine, then the design point $\% \text{-Fill}$ would need to be more carefully selected, such that the upper and lower regions of the engine's operating envelope fall within the dynamometer's working $\% \text{-Fill}$ range at the corresponding shaft speeds. However, this is not a concern here since the speed controlled direct current motor draws whatever power is required to maintain the set speed, as long as the load is below the motor's maximum rated power.

To estimate the low-speed prototype power absorption capabilities the Dynamometer Code was used to generate a performance map, presented in Figure 8-1. Recall that a performance map is a plot of several power-speed curves, where each curve corresponds to a different liquid level (or $\% \text{-Fill}$). This is a *predicted* performance map since it was numerically generated. This distinction is made here so that there is no confusion with the empirical performance map presented later in the chapter.

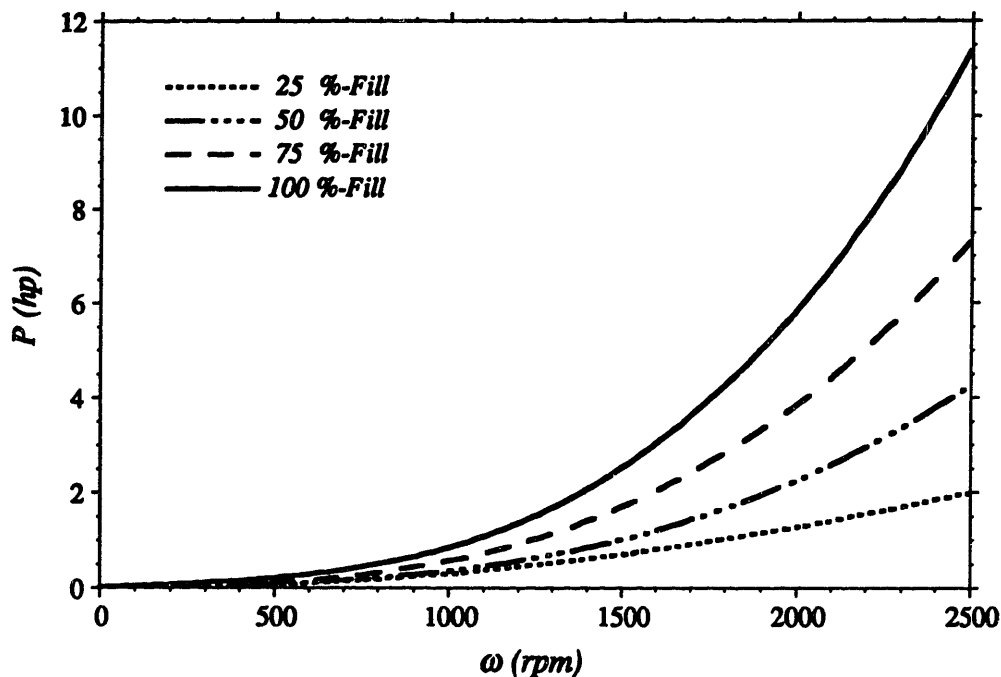


Figure 8-1. Low-speed prototype *predicted* performance map

The blading algorithm and programs, described in Chapter 4, were used to generate raw rotor and stator blade data based on the specifications listed above. The raw blade data was fed into a CAD system and used to form Base and Inner curves for the blades. Each blade was cut back and shaped as described in Chapter 7. Then, N (equal to 16 here) blades are set, equally spaced, inside a toroidal shell that is broken into two parts, where the inner part is the rotor and the outer part is the stator. The rotor shell is 1/4 of an inch thick and the stator shell is 3/8 of an inch thick, strong enough to withstand the anticipated stress levels. A small hole was designed into the stator blades, that run approximately radially through each blade, for exploratory purposes. The completed CAD model is shown in Figure 8-2. This computer model was used to drive a Stereo Lithography system, which produced an epoxy-resin rotor and stator. These epoxy-resin models are used as the working parts of the low-speed prototype. The epoxy-resin is translucent, making it possible to directly observed the flow in the dynamometer. The remainder of the prototype was constructed out of metal, a sectional view of which is shown in Figure 8-3.

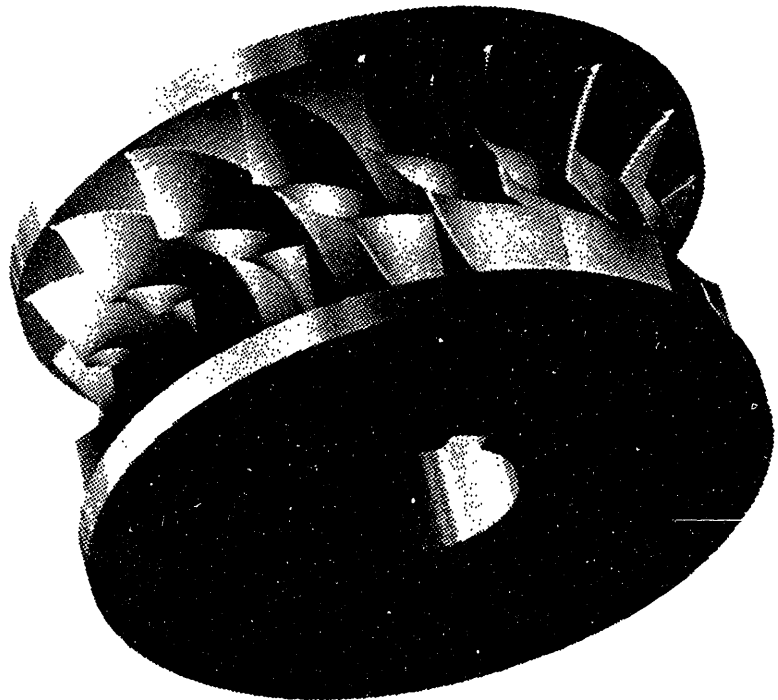
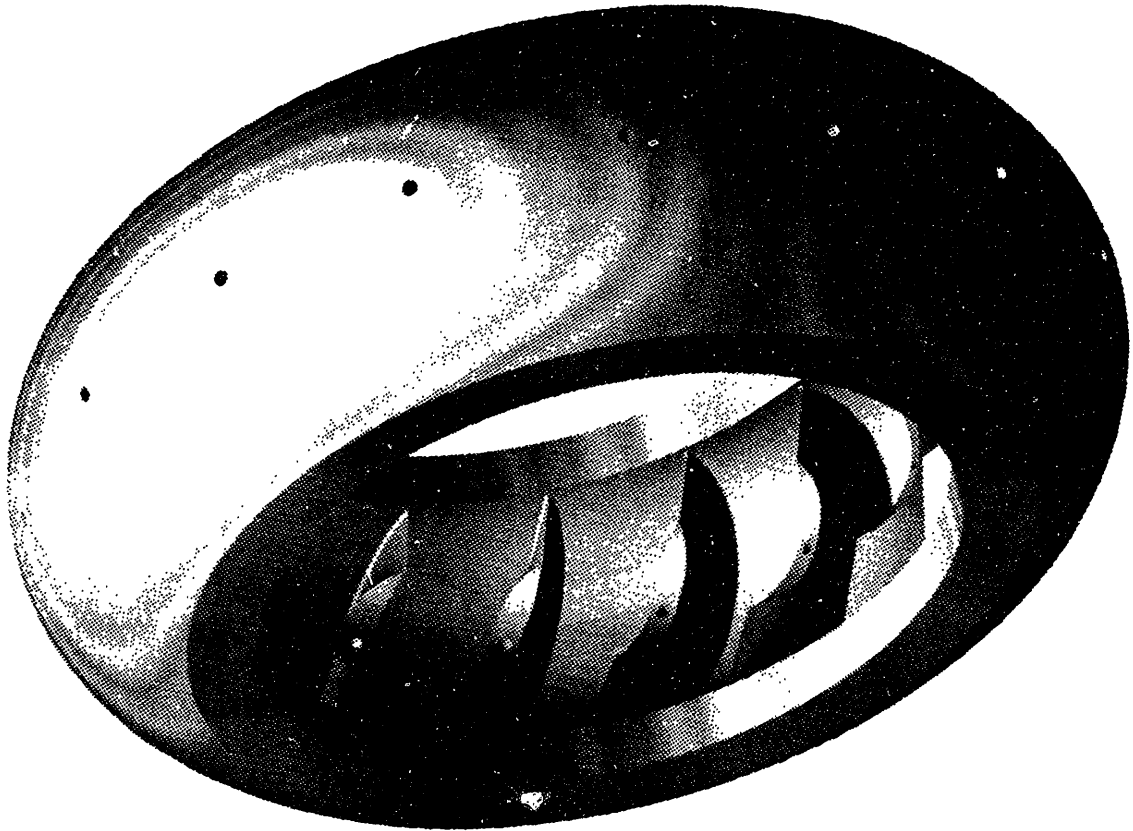


Figure 8-2. CAD image of the rotor and stator

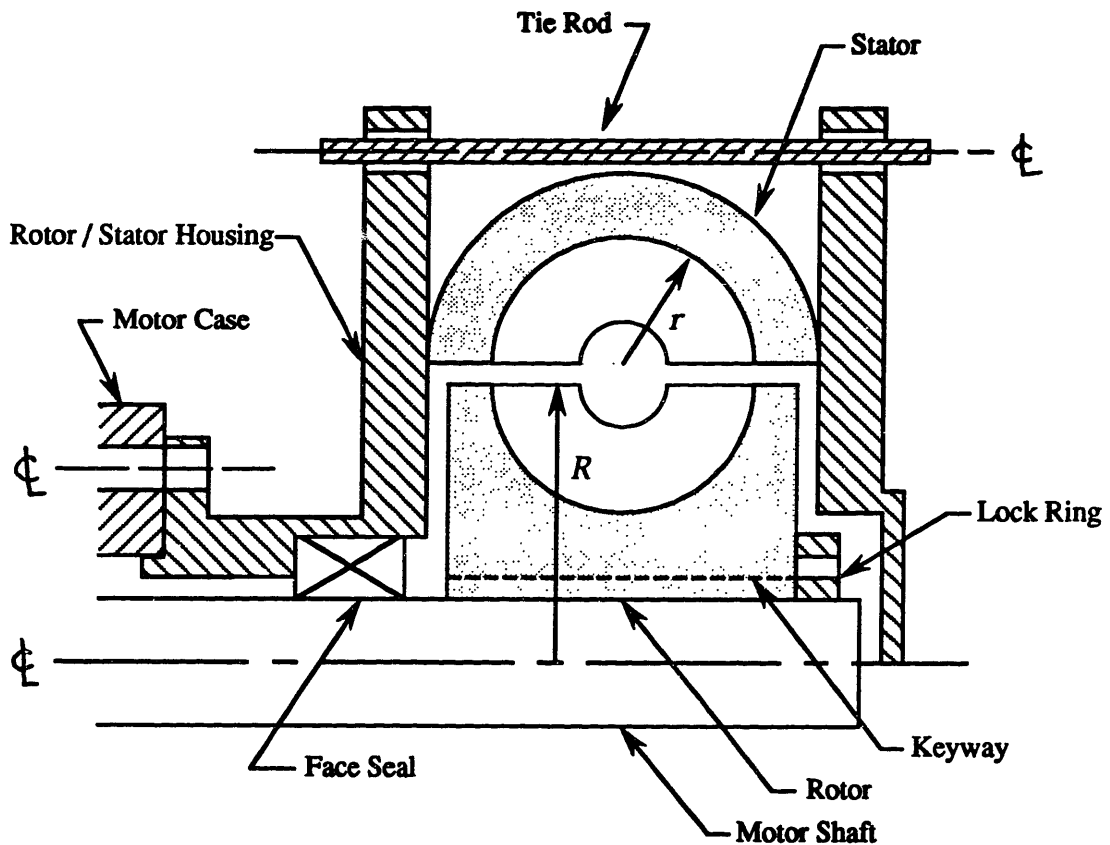


Figure 8-3. Sectional sketch of the low-speed prototype

The prototype was designed to be directly mounted on the motor, which helps insure alignment. The outer casing, which holds the stator in place, is mounted to the face of the motor, and the rotor is mounted on its keyed shaft. The liquid compartment is separated from the motor by a Face Seal. The stator shell has several holes in it. Some of the holes are used simply for filling and draining water, while others are used for pressure taps and thermocouple leads. The experimental instrumentation that was used is described in more detail in the following section.

8.3 Experimental Set-up & Test Procedures

To test the low-speed dynamometer prototype an experimental Test Set was constructed. Some of the parts from the Flow Visualization Experiment were reused here, while other parts, instrumentation, and probes were constructed or adapted exclusively for this experiment.

The Test Set consists of a wood frame and test platform (Test Bed), direct current motor, variable voltage power supply, instrumentation, and a data acquisition system. The motor is mounted to the test platform and is excited by the power supply, which is wired into a three-phase power source. The motor speed was controlled by adjusting the power supply auto transformer, and was measured with a tachometer. The *dc* voltage and current being supplied to the motor was measured using a voltage bridge and a current probe. The temperature of the water in the prototype was measured with a thermocouple, and the shell pressure (resulting from the recirculating liquid) was measured with a pressure transducer. These analog signals were fed into a data acquisition system, converted to digital signals, and recorded by a computer. Also, a translating pitot tube was constructed to determine the radial velocity gradient across the recirculating liquid flow. Furthermore, a strobe light was used to investigate the flow consistency. The experimental set-up is shown below in Figure 8-4.

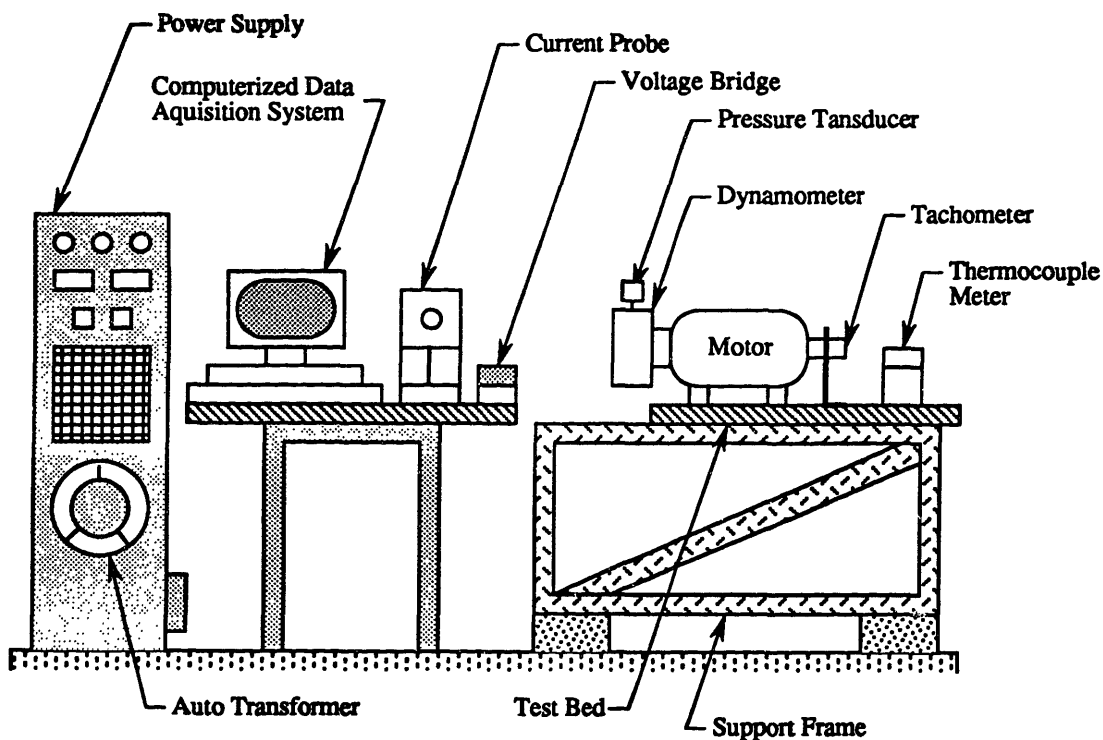


Figure 8-4. Low-speed prototype experimental set-up

Three basic types of tests were conducted — steady, quasi-steady, and transient. In a steady test the rotor speed is fixed, while power and pressure information are recorded. In a typical quasi-steady test run the rotor speed is slowly varied over a wide range. The rate

of variation is slow enough that transient effects are negligible. Therefore, at corresponding speeds the steady and quasi-steady power absorption is approximately equal. The objectives of the steady and quasi-steady tests were to confirm the basic flow trends and generate an experimental low-speed performance map. In transient tests the rotor speed is varied as fast as possible to maximize the dynamic effects. The transient tests were intended to provide insight into the dynamic nature and stability of the flow in the dynamometer.

Test runs were conducted with the dynamometer empty (unloaded) and filled (loaded) with various amounts of liquid (*%-Fill*). The power absorbed by the dynamometer at any speed is simply the difference between corresponding loaded and unloaded test runs. This technique is much more accurate than using an effective (or average) motor efficiency. The low-speed experimental results are presented in the following section.

8.4 Empirical Results

There were over 100 different low-speed dynamometer tests executed using the experimental apparatus described above. Several tests, including all of the quasi-steady test runs, were conducted at least twice to ensure repeatability and accuracy. The instrumentation readings were checked before and after each test run to reduce the systematic error. Much of the experimental error can be attributed to inexact amounts of liquid fill, and variations in fluid properties resulting from temperature changes.

During testing the dynamometer would leak a small amount of water, especially at high rotor speeds (high pressures), but the amount was small compared to the liquid working volume. Each test was conducted in under a few minutes, after which the water was too hot and needed to be drained and replaced with fresh cold water. After the hot water was drained dry nitrogen gas was used to purge the dynamometer and absorb moisture, minimizing the amount of water left in the dynamometer. This was important, since the amount of liquid (*%-Fill*) was measured in a container before being dumped into the dynamometer. Any residual liquid, from the previous run, introduced error in the *%-Fill*. However, since the repeated tests agreed very well it is reasonable to conclude that this source of error was small.

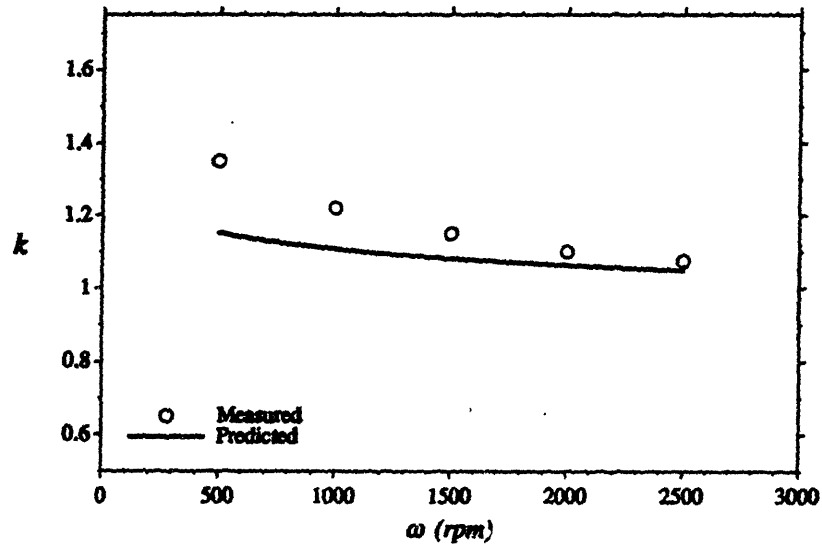
8.4.1 Verification of Basic Flow and Power Absorption

The first tests to be executed were the steady and quasi-steady tests, starting with the no-load (empty dynamometer) runs to determine the motor and frictional losses over the rotor speed range of interest (500-2,500 rpm). Then the same test runs were repeated for several different liquid levels (%-Fill). The primary objectives here were to confirm the basic flow and behavioral trends, as well as to empirically generate a performance map.

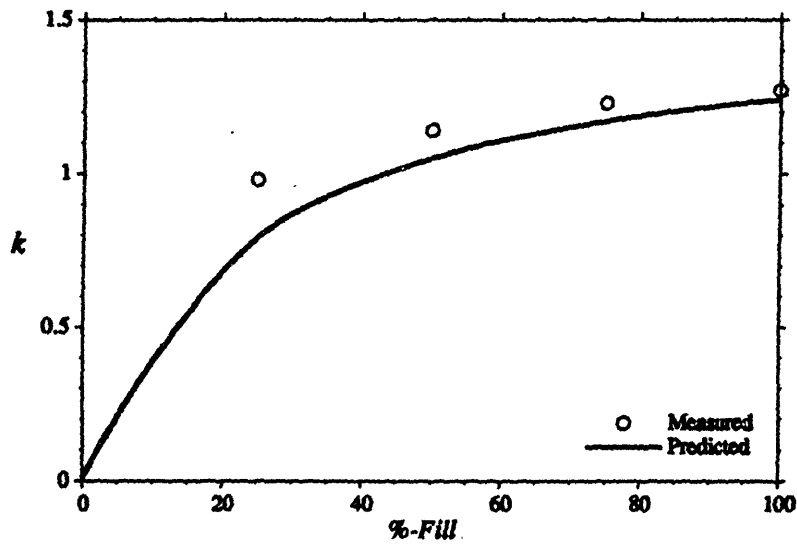
It was immediately apparent (from the first test run) that the helically recirculating free surface flow was indeed being developed in the dynamometer. Above a critical velocity (when the local centrifugal acceleration surpassed gravity) the flow began to recirculate in an organized manner as predicted. This was directly observed by looking through the highly translucent epoxy-resin stator. The integrity of the recirculating dynamometer flow was very good over a wide range of rotor speeds.

Once the basic nature of the flow was confirmed the behavioral trends were investigated and compared to theoretical predictions. The design point recirculation factor was determined to be approximately 1.2, which is close to the estimated value of 1.15 that was calculated using the Dynamometer Code. The low-speed prototype was designed using an old (cruder) version of the program which estimated the design point recirculation factor to be 1.75, which is why the *geometric* recirculation factor (defining the blade turning angle) is so high. It is clear from the experiment that the flow enters the stator stage at an angle that more closely corresponds to a recirculation factor of 1.15 instead of 1.75. The difference is approximately 10° which is not enough to de-stabilize the flow (as determined from the Flow Visualization Experiment). Despite this, the measured recirculation factor trends agree very well with the predicted trends, as can be seen in Figure 8-5.

The friction factor also exhibits trends similar to those predicted. That is, as the Reynolds number of the flow increases (with rotor speed) the friction factor decreases slightly. Also, the friction factor decreases slightly with increasing percentage of fill as expected. However, the magnitude of the friction factor is approximately 25% of the estimated value, as can be seen in Figure 8-6 which compares the measured data with various friction correlations. The bottom curve in the figure is the ITTC correlation line [7] that curiously approaches the measured data if it is multiplied by the same factor used to modify the Moody pipe flow friction. However, this is probably just a coincidence since the ITTC correlation is for smooth flat plates, and is typically used to model ship hulls.



(a)



(b)

Figure 8-5. Recirculation factor trends, (a) k vs. ω , (b) k vs. %-Fill

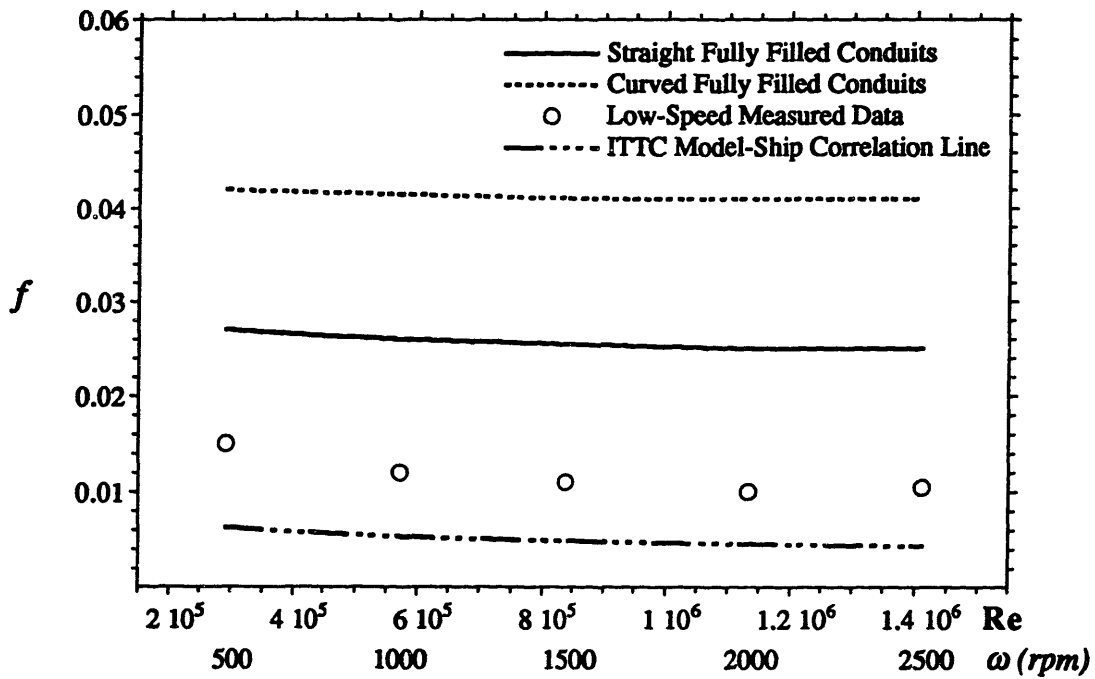


Figure 8-6. Friction factor variation with Reynolds number

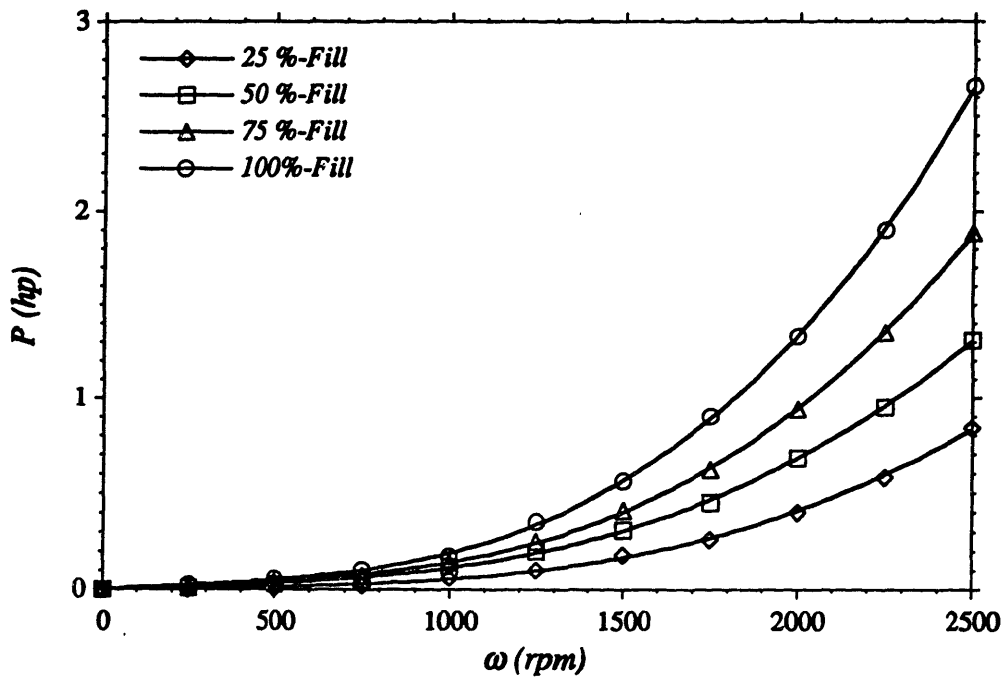


Figure 8-7. Low-speed prototype empirical performance map

The most significant finding here is that the dynamometer power absorption varies with the rotor speed and percentage fill in the same way as theoretically predicted. That is, the dissipated power is proportional to the rotor speed cubed (at a fixed %-Fill), and increases nearly linearly with increasing percentage fill (at a fixed ω) above a threshold of approximately 15-20%. The experimentally measured power absorption data was used to generate an empirical performance map, presented in Figure 8-7 above.

While the general power absorption trends agree well with theoretical predictions, the measured power dissipation is lower than predicted. This is primarily due to the difference between predicted and measured friction factors, and also to the discrepancy in recirculation factors. If the predicted power absorption is modified by multiplying it by the ratio of the measured friction factor to the predicted factor (equal to about 0.25) then the results are much more agreeable as can be seen in Figure 8-8 below. Furthermore, since the power absorption is a function of the recirculation factor cubed, even small differences can account for discrepancies between measured and predicted values. Thus, the results would be improved even more by accounting for differences in the recirculation factors.

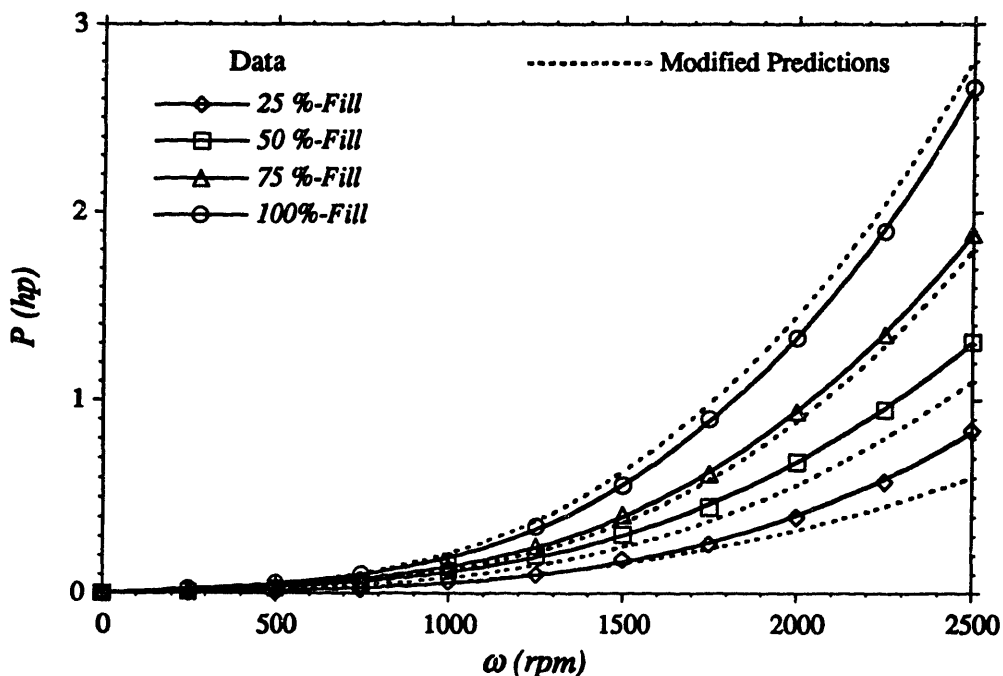


Figure 8-8. Comparison between measured power absorption and *modified predictions*

This information can be represented in dimensionless terms by plotting P^* against Reynolds number, as in Figure 8-9 below. Notice that the dimensionless power (at any particular %-Fill) rapidly approaches a constant value as the Reynolds number increases, as anticipated. This confirms that the power and rotor blade tangential velocity have been appropriately non-dimensionalized (see Chapter 6).

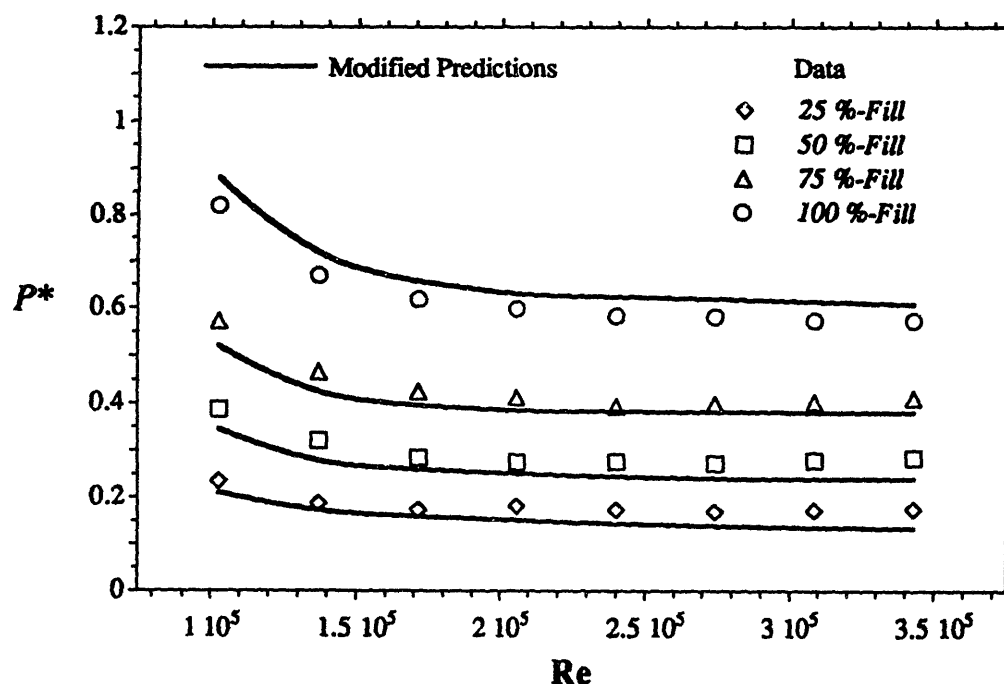


Figure 8-9. Non-dimensional performance map

It is no surprise that the measured friction factors (f) are so far off the predicted values. The discrepancy can be attributed to both inaccuracies in the prediction method and in the estimation of the surface roughness. The friction factor prediction method is clearly only approximate at best, since it is based on fully wet pipe flow correlations. Furthermore, the surface roughness which is used to determine f is unknown. A rough estimate was made based on the materials and finishing technique, but it is very difficult to determine what the actual surface roughness is of the experimental prototype because of its toroidal geometry. Another possible explanation for the friction factor and/or power absorption discrepancy is explored in the following section.

8.4.2 Radial Velocity Distribution, Flow Consistency, and Stability

Several other steady, quasi-steady, and transient tests were conducted to determine the radial velocity gradient and provide insight into the flow consistency and dynamic stability. The radial pressure gradient was measured using a translating pitot tube from which the velocity profile was determined. Following this, the flow was further explored using a strobe light, to help characterize the flow consistency. Finally, transient tests were conducted to study the dynamometer (particularly the recirculating liquid) dynamics.

The recirculating liquid exerts a pressure on the torus shell, which increases as the rotor speed increases. This pressure can be estimated with Equation 7.4, which assumes that there is a slug velocity profile. The slug approximation is also used in the flow model, and consequently the Dynamometer Code, so it was important to determine the actual velocity profile. From Figure 8-10, it is clear that the estimated and measured static pressure agree quite well, which supports the slug flow model. If the recirculating flow did not have a slug type profile, then the pressure calculated based on the slug flow approximation would not have agreed so well with the empirical data.

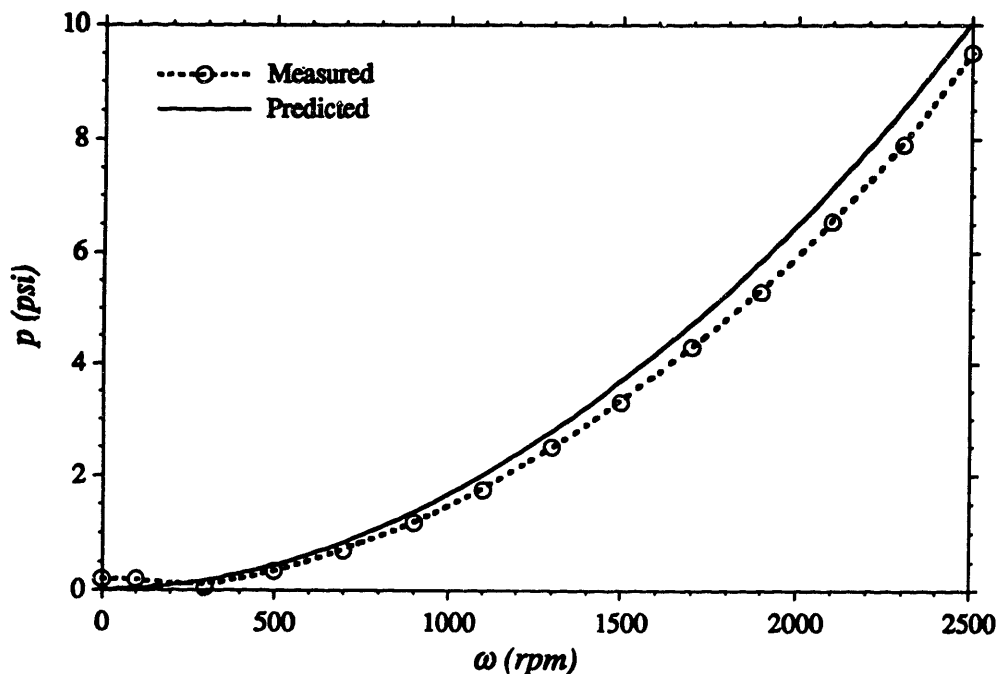


Figure 8-10. Comparison of predicted and measured static pressure rise with ω

To corroborate this claim a translating pitot tube was constructed and used to determine the radial velocity profile for several rotor speeds and liquid levels. From Figure 8-11 it is clear that the velocity profile is nearly flat, therefore the slug flow approximation is reasonable.

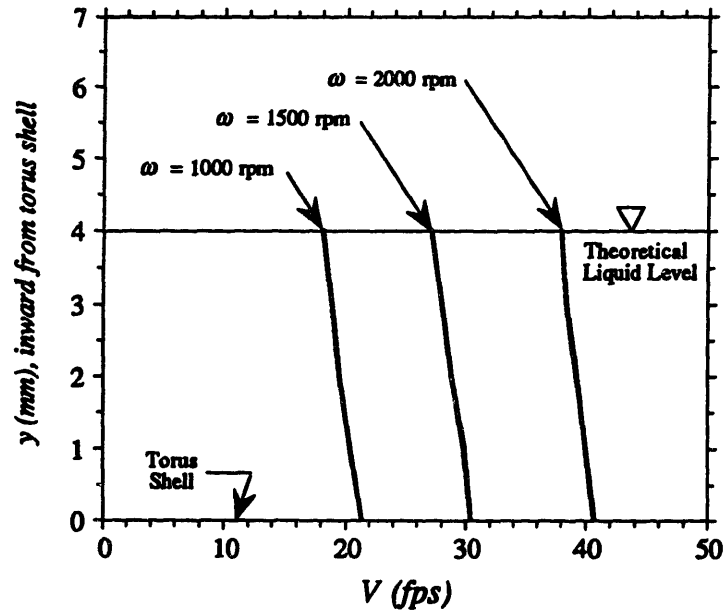


Figure 8-11. Radial velocity profile at different speeds, for 100 %-Fill

Next, the flow consistency is discussed. As the rotor speed is increased bubbles develop in the flow, and at high speeds cause the flow to appear frothy and white. Due to the highly turbulent nature of the flow, and blade leading edge interaction with the liquid, the free surface is extremely chopped up. It is the authors belief that the white appearance of the flow is caused by air bubbles that enter the flow predominantly through the free surface, and rotor-stator interface, which are quickly mixed into the recirculating liquid. To determine if cavitation was a significant source of bubbles the dynamometer was filled with as much water as possible (about 98% full), and run over the full range of rotor speeds. There were much fewer bubbles and the flow appeared significantly clearer, which indicates that cavitation does not play a major role in the production of these bubbles. Regardless of the source, these bubbles clearly lower the effective density of the liquid sheet, and thus increase the flow sheet thickness in (or wetted height of) the channels. In other words, instead of having a fully liquid recirculating flow there is an air-liquid mixture that occupies more volume. The translating pitot tube was used to determine the true flow

sheet thickness in the stator (for several speeds and liquid levels) and compared to the fully liquid flow sheet thickness, which is calculated based on the volume of liquid in the dynamometer. For four different liquid levels (or *%-Fill*) the following was observed. At very low rotor speeds the sheet thickness was approximately equal to the calculated values. However, as the rotor speed increased the sheet thickness grew, which means that more air was being mixed into the liquid. This clearly reduces the effective density and friction factor, which accounts (to some degree) for the lower than expected power dissipation.

To explore this further a variable frequency strobe light was employed. By adjusting the strobe light frequency the bubbles in the liquid sheet could be more closely examined. The main findings can be summarized as follows. At a rotor speed of approximately *500 rpm* bubbles begin to appear, with a diameter of about 1-2 mm. The bubbles are more abundant near the free surface of the flow. As ω increases the number of bubbles increase, but their size decreases (to less than 1 mm in diameter). At high speeds the bubbles are well mixed into the liquid by the turbulence churning and secondary flow effects, which makes the flow appear white to the naked eye. However, as the rotor speed increases the pressure gradient also grows which in turn compresses the bubbles. This explains why the size of the bubbles decrease with increasing recirculation speed.

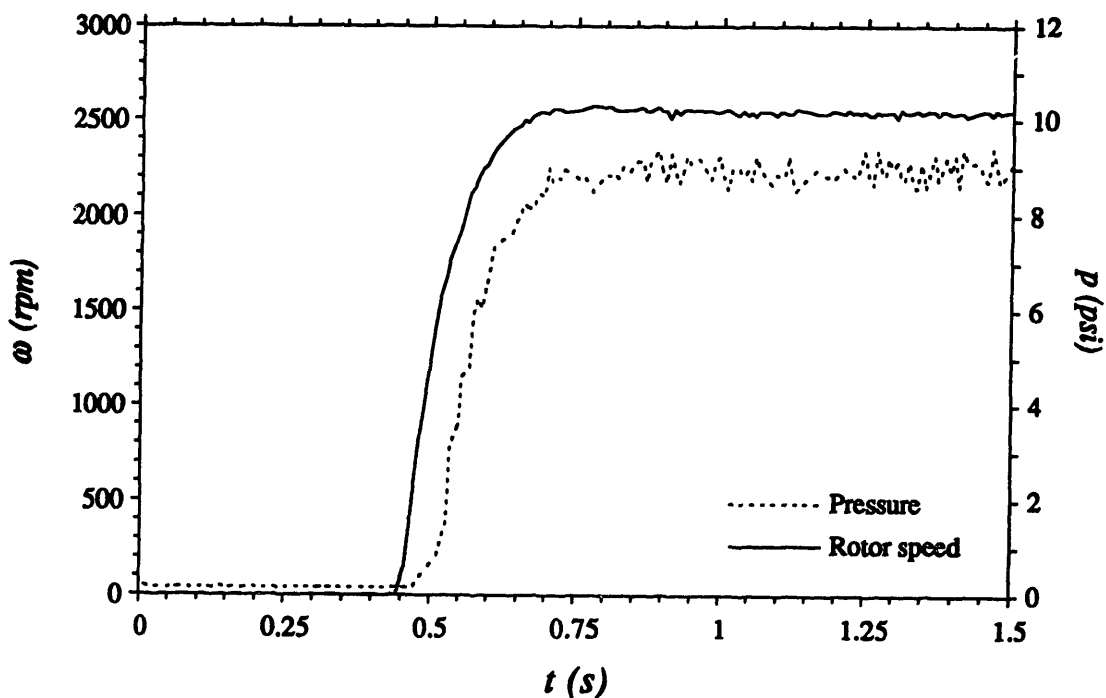


Figure 8-12. Power supply step on test

Finally, to investigate the stability of the flow, and characterize its dynamic behavior, transient tests were conducted. The most important issue addressed was flow response to rapid changes in rotor speed. Several different types of tests were conducted including, instantaneously stepping the power on and off, ramp changes around operating points, and rapid aperiodic rotor speed oscillations around operating points. The most surprising and significant finding was that the recirculating flow in the dynamometer responded very quickly to changes in ω . Since the static pressure (p) or dynamometer shell pressure is directly linked to the recirculating flow velocity, it is a good parameter to gauge the flow with. Figure 8-12 (above) shows the results of a power supply step on test, where the auto transformer is pre-set (corresponding to a steady state rotor speed) before switching the power supply on. As expected the rotor quickly accelerates to the steady state set speed. Surprisingly, the recirculating flow follows the rotor speed very closely, with a small lag time (approximately 25 ms).

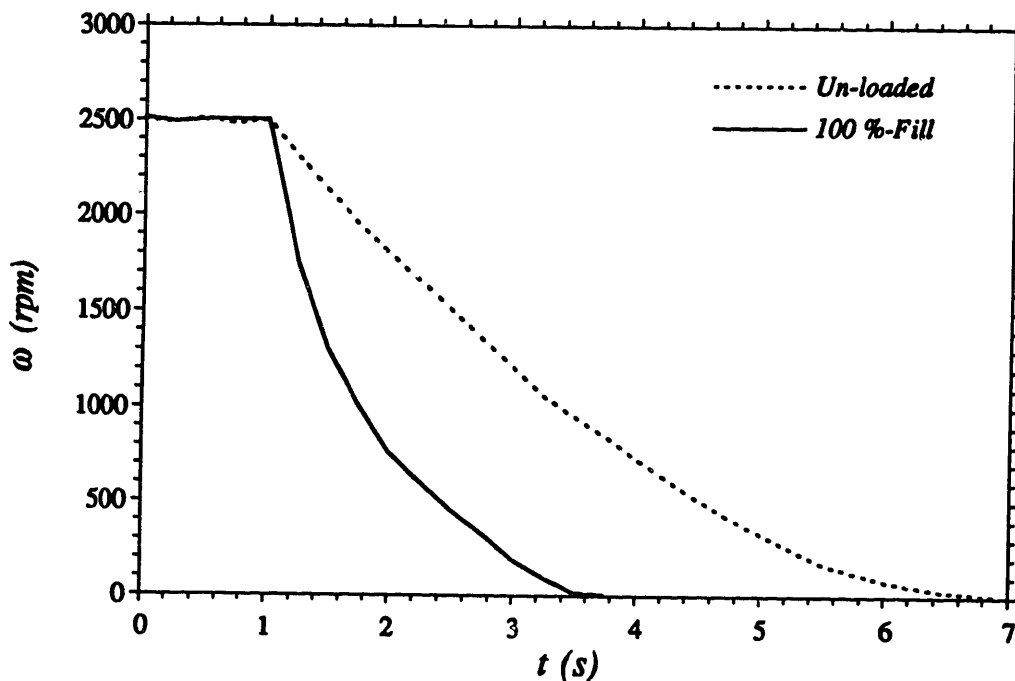


Figure 8-13. Power supply step off, with unloaded and fully loaded dynamometer

Figure 8-13 shows the results of power supply step off tests for a fully loaded (100 %-Fill) and unloaded dynamometer. Notice the difference between the unloaded and fully loaded

test runs. After the point where the power is shut off, the local braking (or damping) torque can be computed from the slope of the curve. Clearly, a steeper slope corresponds to a larger braking torque.

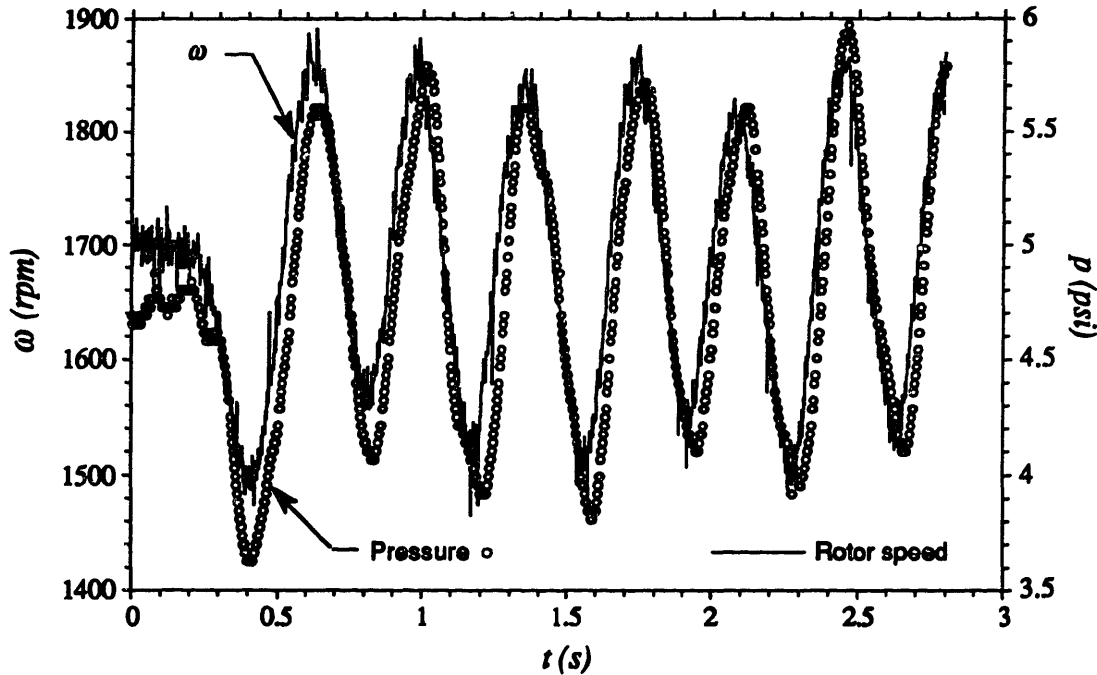


Figure 8-14. Rapid aperiodic rotor speed oscillation test

Figure 8-14 shows the results of a rapid aperiodic rotor speed oscillation test, which is conducted by turning the power supply auto transformer back and forth as fast as possible. Again, the recirculation velocity follows the rotor speed changes very well, with minimal time lag (*approximately 20 ms*). There were many other tests conducted, but these were the most revealing. Some other tests are discussed in Chapter 10 as they apply more to characterizing the system for control purposes. However, the general conclusion from these transient tests is that the dynamometer flow is quite stable and robust with regard to disturbances in ω . Of course, in a fully operational dynamometer evaporation is present, therefore the %Fill and thus power absorption can change rapidly, affecting the overall system dynamics. This issue is discussed further in Chapter 10.

8.5 Additional Remarks

The experimental results are very promising. Not only did they confirm the theories about the basic nature of the flow in the dynamometer, but they revealed that the flow is quite stable. Also, the flow is very definitely self starting, which was a concern prior to this experiment. In other words, it was not clear if the asymmetry of the blading would be sufficient enough to initiate unidirectional liquid recirculation from a stationary pool. Fortunately, it was immediately apparent that the flow was indeed self starting.

The friction factors and recirculating fluid density were lower than anticipated which directly impacts the power absorption. This appears to be linked to the bubbles in the flow. However, the pressure gradients in the low-speed prototype are not nearly as high as they would be in a high speed full-scale dynamometer. From the behavior observed here it is reasonable to assume that the bubbles will be much less prevalent in a high-speed full-scale machine, since the pressure gradients will be quite substantial. Therefore, there should be higher power absorption, and better agreement with the predictive tools developed in the thesis. Also, the low-speed blading is approximately 10° off design point (for previously discussed reasons) which degrades performance. Also, there is a significant amount of uncertainty regarding the true surface roughness. Therefore, using the correct blade turning angles and more precise surface roughness information would improve the agreement between observed power absorption and that predicted by the code.

CHAPTER 9

Full-Scale Steam Generating Prototype Design

The general design algorithm presented in Chapter 7 has been applied to the development of a high speed full-scale steam generating prototype. This is very similar to the design process followed to develop the low-speed prototype, presented in Chapter 8, and thus will not be reiterated here. The low-speed experimental results have been incorporated, and used to improve the power absorption estimates generated from the Dynamometer Code. Results are presented below in summary form with a brief discussion of the key issues.

The full-scale prototype has been designed to meet the load requirements of a series of gas fueled turboshaft engines that are manufactured by Textron-Lycoming (namely the T55-L-712/714 series engines). The power output of these engines range from 2,000-5,000 hp, at rotor shaft speeds of 14,000-20,000 rpm. A typical steady operating load is approximately 3,500 hp at 16,000 rpm. Therefore, the dynamometer design point was selected to correspond to this load and rotor speed. Recall that the major dynamometer design task is selecting a size and configuration that results in a machine that can accommodate the full power range (or operational envelope) of the engines to be tested. This usually requires iteration, but can generally be accomplished easily with the aid of the numerical programs and information previously presented. This was done, and the parameters that define the full-scale prototype are listed below.

Major Radius (R): 2.5"

Minor Radius (r): 1.0"

Blade Height (h): 0.6"

Maximum Blade Thickness (t_{max}): 0.325"

Blade Packing ($B.P.$): 0.5517

Number of Rotor Blades: 16

Number of Stator Blades: 19

Recirculation Factor (k): 1.2

Design Point Liquid Level (%-Fill): 58%

Surface Roughness (ϵ): 600 micro-inch

Water fill conduits, 1 per blade, 0.25" circular diameter

Steam Vent Area (A): 7.85 sq.in, 0.41 sq.in per stator blade

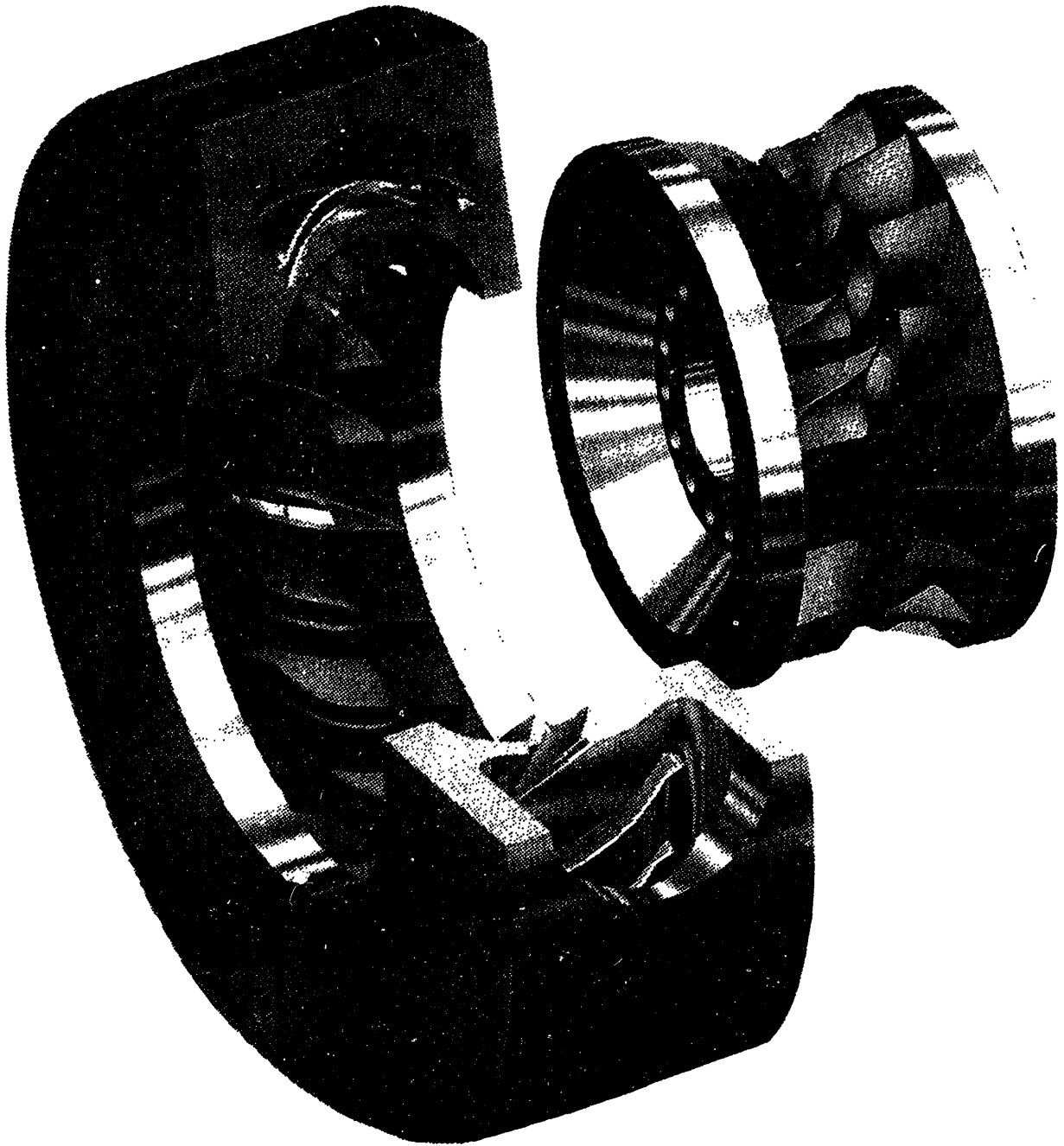


Figure 9-1. CAD representation of full-scale prototype

The make-up flow rate (or water supply) required at the design point is approximately 20 gallons per minute. At steady operation, the equivalent mass flow must exit the working compartment in the form of vapor (or steam). The steam vent area was calculated using the technique presented in Chapter 7 which results in a core pressure that is roughly one atmosphere above the steam outlet manifold pressure (assumed here to be near atmospheric). Therefore, the core pressure is approximately two atmospheres.

The pressure rise across the recirculating liquid flow varies depending on the particular point in the flow circuit and has been estimated using Equation 7.4 at three points of interest, which are listed below.

Maximum torus shell pressure (hub region @ 16,000 rpm), $p_{max} \approx 110 \text{ atm}$

Rotor/Stator interface pressure (split pressure @ 16,000 rpm), $p_{split} \approx 75 \text{ atm}$

Minimum torus shell pressure (stator outside @ 16,000 rpm), $p_{min} \approx 45 \text{ atm}$

Figure 9-1 is a CAD representation of the full-scale prototype. Large steam vents in the stator blades are clearly visible. Water fill conduits can also be seen in the rotor blades. This is not the best location for fill conduits as was discussed previously. However, the intended manufacturer of this dynamometer, Textron-Lycoming, found this to be a reasonable location in terms of manufacturing requirements.

The flow modeling (Dynamometer Code) was used to make performance predictions for this machine, as was done for the low-speed prototype, which is shown in Figure 9-2.

The extremities of the performance envelope can be easily determined. The dynamometer is predicted to be capable of absorbing 2,000 hp at 14,000 rpm and 80%-Fill, 4,400 hp at 16,000 rpm and 100%-Fill, and 5,000 hp at 20,000 rpm and 73%-Fill, which is sufficient. Engine curves, or the operating envelope, can be superimposed over the dynamometer performance map making it easy to identify the appropriate %-Fill for a particular engine set-point. Of course in an actual test scenario, fluid level selection and adjustment would be best handled by a computer. This subject is addressed in greater detail in Chapter 10.

The predicted performance map presented in Figure 9-2 is optimistic, because of the previously discussed inaccuracies associated with the flow model. The estimated friction factors (used to determine the predicted power dissipation) are probably somewhat higher

than actual, as was observed in the low-speed experiment, which has a direct impact on power absorption. Therefore, an attempt is made here to improve the predicted performance map based on the results of the low-speed prototype experiment.

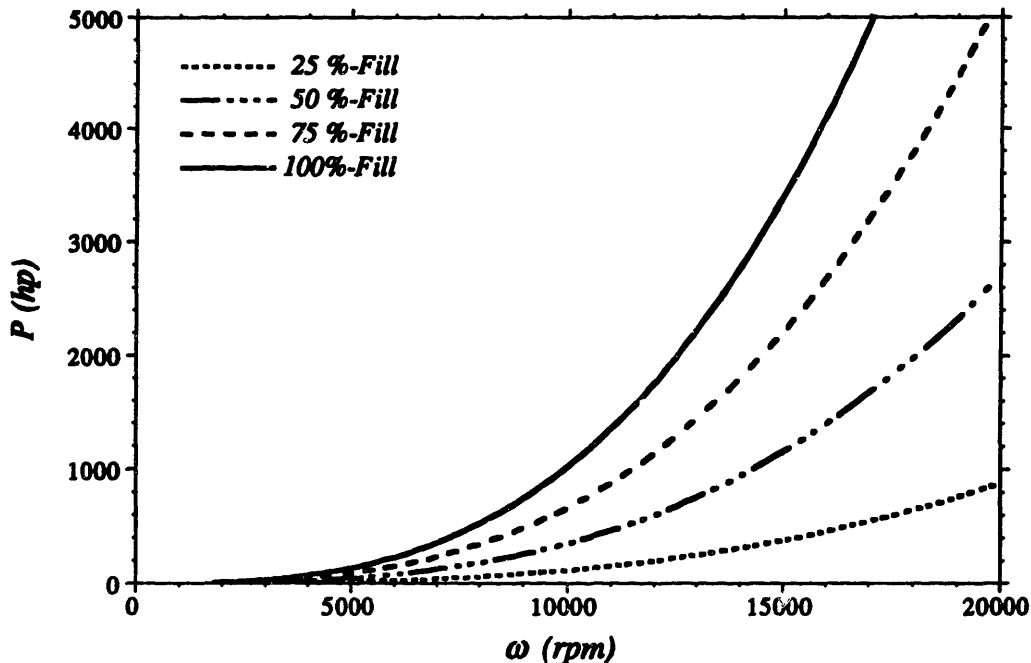


Figure 9-2. Predicted full-scale performance map

The actual low-speed prototype friction factors were 25% of the predicted values, which is the primary reason that the actual power absorption was lower than estimated. If the same behavior holds true for the high speed full-scale prototype, then the observed power absorption will be proportionately less than predicted. Therefore, the predicted full-scale power absorption can be modified (based on the low-speed experiment) by multiplying the predicted value by the ratio of the observed to predicted low-speed friction factors ($f_{observed}/f_{predicted}$, equal to roughly 0.25). This has been done and the results plotted in Figure 9-3.

From Figure 9-3 it is clear that the maximum power absorption at 16,000 rpm is just over 1,100 hp. If this modified estimated power is close to the actual power dissipation, then the full-scale prototype is too small to meet the full operational requirements of the engines. This can be remedied by either adding three dynamometers, or increasing the size.

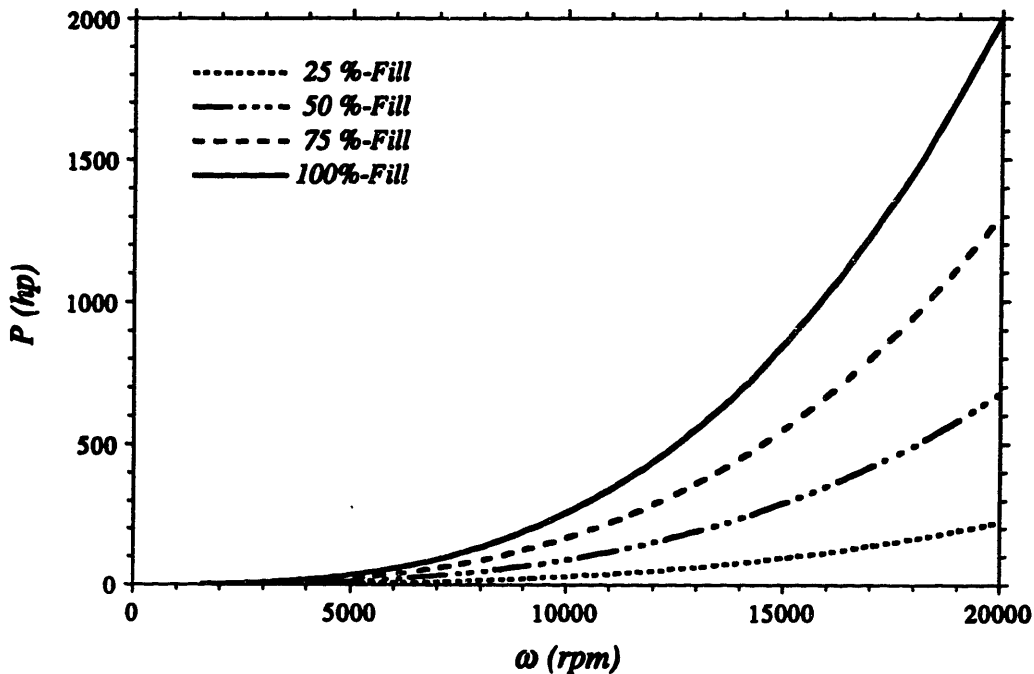


Figure 9-3. Modified estimated full-scale performance map

Adjusting the size is the better option, since the scaling laws (discussed in Chapter 7) showed that the power dissipation increases with the outside diameter (D) raised to the fifth power. That is, instead of having several 7" outside diameter machines it is better to have one 9.4" outside diameter dynamometer that can absorb up to 5,000 hp at 16,000 rpm. Of course, these corrective measures would only need to be invoked if the observed friction factor is 75% less than predicted, as in the low-speed experiment.

However, the air bubbles that were observed in the low-speed experiment (which reduce the power absorption) are anticipated to be less significant in a high speed full-scale machine because of the large pressure gradients that are anticipated. Thus, the actual friction factors and power absorption should be higher than suggested by the low-speed results. Therefore, the true power dissipation lies somewhere between the *modified estimated* and the predicted absorption, where Figures 9-2 and 9-3 can be thought of as upper and lower limits for the *true* performance map. Eventually the predicted performance will converge with the *true* (or actual) data as the body of knowledge grows from modeling improvements and increasing amounts of experimental data.

CHAPTER 10

Fundamental Dynamics and Control Issues

10.1 Overview

The primary function of any dynamometer is to produce a load on the engine being tested, or a torque that acts on the output shaft in a direction opposite to rotation. In other words, the dynamometer can be thought of as a rotational damper. Different loads, or torque levels, must be applied for different test scenarios. For some types of engines it is desirable to be able to produce rapidly varying torque conditions for transient testing. To accomplish this an effective dynamometer control scheme must be devised, and the appropriate control parameters identified.

As in many other dynamometers the torque (T) developed can be described in terms of an inertia and a damping term, neglecting any rotational compliance, as in Equation 10.1 where J is the rotational inertia, B is the damping coefficient, ω is the angular velocity, and α is the angular acceleration.

$$T = J\alpha + B\omega = J\dot{\omega} + B\omega \quad (10.1)$$

However, in this dynamometer the fluid inertia is a function of the amount of liquid water (*%-Fill*) in the working compartment, and the damping coefficient is a function of both the *%-Fill* and angular speed (ω), which makes Equation 10.1 highly non-linear. This complicates the control problem since torque is the main dynamometer output variable of interest. Furthermore, because of this non-linear behavior it would be very difficult to develop a global (over the entire performance envelope) linear Transfer Function for dynamometer torque control.

As aforementioned, the dynamometer torque can be varied in two ways. One way is to change the rotor speed. From the flow model and experimental results it was shown that the steady state power is a function of rotor speed (ω) cubed and thus the torque is a function of ω squared, for a fixed liquid level (*or %-Fill*) in the working compartment. But since this dynamometer is intended to be used with speed controlled engines, the only dynamometer input parameter that can be independently adjusted is the *%-Fill*. In other words, with the speed set by the engine controller (throttle position) the only way to vary

the torque or load is to change the amount of liquid in the dynamometer, which is done by adjusting the feed water mass flow rate. This can be accomplished in a variety of ways, ranging from manual control (someone physically operating valves), to a fully automated computer controlled process. Of course, to take full advantage of the dynamic capabilities of the dynamometer requires at least partial automated control, including fluid level (*%-Fill*) control. Furthermore, with automated controls it is a simple matter to carry out variable load tests (e.g., a "Wave-off" test), by executing a preprogrammed computer sequence. However, the first step in developing an automated control scheme is understanding the dynamometer dynamics and estimating key parameters.

10.2 Dynamic Behavior of the Dynamometer

Before a control scheme can be developed the dynamic behavior of the dynamometer system must be understood. This system consists of a dynamometer, water flow supply, an inlet flow control valve, and possibly an outlet flow valve. An outlet flow valve would be desired if the rate of change of liquid volume (*%-Fill*) in the dynamometer needs to be very fast, where the rate of change results from evaporation, liquid inflow, and liquid efflux (if an outlet valve is used).

The most important issue is whether the overall plant (consisting of an engine, dynamometer system, flywheel, and other components) is stable or not. One major criterion for stability of an engine-dynamometer system is that the rate of change of the dynamometer torque (T) with respect to changes in ω must be greater than (or equal to) the engine, as expressed below.

$$\left. \frac{dT}{d\omega} \right|_{\text{dynamometer}} \geq \left. \frac{dT}{d\omega} \right|_{\text{engine}} \quad (10.2)$$

Of course, this is only a concern when ungoverned engines are used. Since the type of engines intended to be tested with this dynamometer are speed controlled, and engine torque is an output parameter determined by the dynamometer load, Equation 10.2 will be satisfied at all points inside the engine's operating envelope.

In this dynamometer the T rate of change, at either fixed or variable ω , is a function of how fast the recirculating liquid in the dynamometer responds to shaft speed changes, as well as

how fast the liquid level (*%-Fill*) is changed. From the low-speed prototype transient tests the response time (lag time) of the recirculating liquid was found to be quite short, on the order of *10 milliseconds*. The recirculating fluid tracked the rotor very closely even for *step-on* and *rapid aperiodic variation* tests, the results of which were plotted in Figure 8-12 and 8-14. In fact, the response time was comparatively shorter at higher rotor speeds. Therefore, it is reasonable to assume that the response time will be shorter for a full-scale high speed machine than was observed in the low-speed experiment. However, in addition to the recirculating fluid lag time, the dynamometer system response is also a function of the feed conduit lag time and inlet (outlet) control valve response time. At a fixed rotor speed the rate of change of torque is limited by the rate of change of liquid inside the working compartment of the dynamometer. In other words, the response time depends largely on how fast the volume of liquid (V_{liq}) inside the dynamometer (*%-Fill*) can be changed, which is a function of the mass flow rate into and out of the machine. This can be expressed as follows where ρ is the mean density of the liquid (approximated as a constant here) in the working compartment.

$$\frac{dT}{dt} \propto \frac{d(\% - Fill)}{dt} \propto \frac{dV_{liq}}{dt} = \frac{1}{\rho} (\dot{m}_{in} - \dot{m}_{out} - \dot{m}_{evap}) \quad (10.3)$$

This equation is non-linear since the evaporation mass flow rate is a function of the *%-Fill*. Furthermore, the liquid influx and efflux may be temporally changing which makes the equation difficult to solve analytically. Therefore, it is desirable to evaluate Equation 10.3 numerically, using real-time feedback. This is discussed in the last section of this chapter.

However, Equation 10.3 can be used to make response estimations for small volume changes around an operating point. Consider the case where the liquid water supply and bleed (outlet) are shut off. Now the rate of change in volume can be determined from the power dissipation rate (P) as in Equation 10.4, where Δh_{fg} is the latent heat of vaporization, and the sensible heat required to increase the temperature of the liquid feed water is neglected.

$$\frac{dV_{liq}}{dt} = \frac{-1}{\rho} \frac{P}{\Delta h_{fg}} \quad (10.4)$$

However, Equation 10.4 is also non-linear since the power dissipation is a function of the amount of liquid (*%-Fill*) in the dynamometer, but it can be used to make approximations

for small changes around an operating point. The time required to change the liquid level (around an operating point) in the dynamometer can easily be computed for these small changes. To estimate the time required for large changes Equation 10.4 can be numerically integrated, calculating P for each discrete *%-Fill* between the limits.

Other volume rate of change scenarios can be estimated starting with Equation 10.3, but numerical techniques are required for accurate results over large variations. The functional dependencies of the inlet and outlet mass flow rate terms can be estimated with manufacturer correlations and factors, while the evaporation rate can be estimated using the programs developed in this thesis. Of course, since the dynamometer system is highly non-linear, the best way to get accurate dynamic information is to build and test a fully functional prototype. The experimental data can then be used generate empirical relations for future use. In many cases the desired dynamic information can be quickly generated, once an engine-dynamometer system is assembled, by simply executing some preliminary transient tests and measuring response times.

10.3 Key Dynamometer Parameters

Key parameters must be identified to design a control scheme. From Equation 10.1 it is clear that inertia (J) and damping coefficient (B) are two important parameters. Also, the response characteristics of the flow control valve(s) and liquid inlet (outlet) conduits are very important, since this determines how fast the *%-Fill* can be changed. However, since there are numerous possible flow control valves and conduit design schemes no further attempt is made here to model these components or estimate their dynamic behavior. Instead, the focus is on the dynamometer.

The dynamometer rotational inertia is a function of the rotor mass and mass of liquid inside the rotor stage of the working compartment. These values can be calculated, but require numerical techniques because of the complex toroidal geometry. However, since the liquid mass is small compared to the rotor mass (metal), it can usually be safely neglected. In fact, since the dynamometer rotor mass is typically much smaller than the engine rotor assembly and flywheel mass, it to can usually be neglected as well.

Since the main function of a dynamometer is to act as a rotational damper the most important parameter is B , the damping coefficient. As aforementioned, B is a function of

the $\%Fill$ and ω , which complicates the control task somewhat. The dynamometer performance prediction code developed in Chapter 6 can be used to estimate the damping (or developed torque) for any $\%Fill$ and ω . However, it is better to use either empirical performance data, or actual feedback signals. Since the later choice is the most accurate and practical it will be explored in greater detail in the following section.

10.4 Dynamometer Control Schemes and Engine Testing

With a basic understanding of the dynamometer dynamics, and techniques for estimating or measuring key parameters, an engine-dynamometer system (or plant) control scheme can be designed. The plant controller must be designed such that the desired engine testing conditions can be produced, particularly with regard to the transient tests. The selection of control variables is somewhat a matter of choice. Although, the set of variables selected must be sufficient to carry out the desired tests effectively.

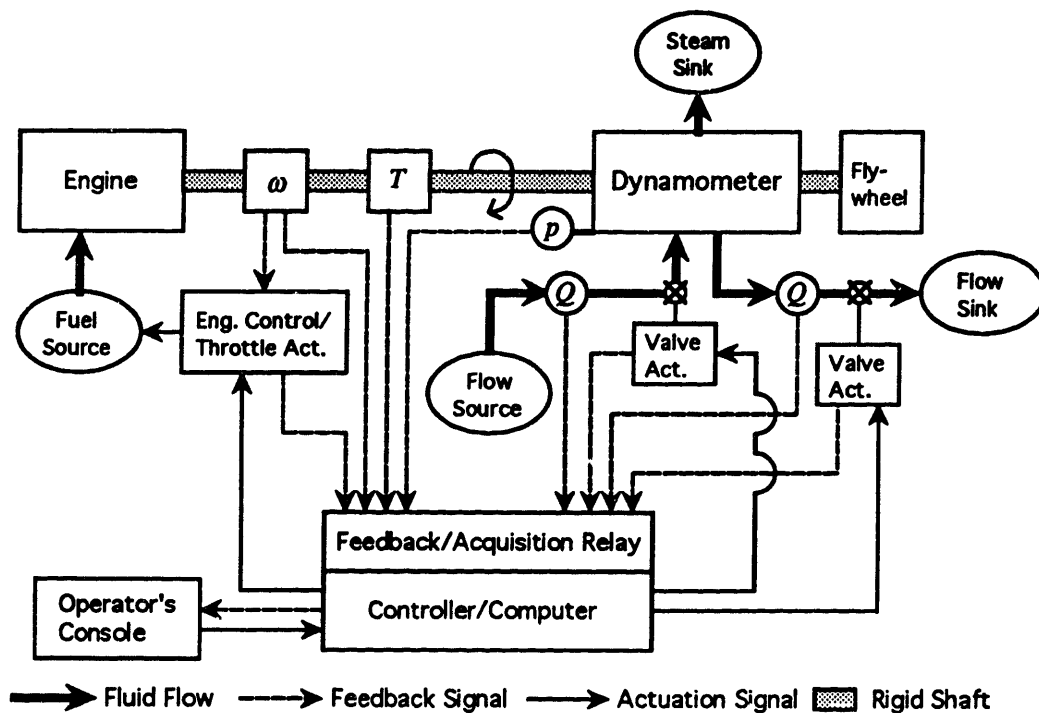


Figure 10-1. Engine-dynamometer system with several instruments

In any engine test scenario a desired torque, or time-dependent torque variation, must be developed by the dynamometer. At the very least there are two parameters (ω , and either T or $\% \text{-Fill}$) that must be determined or directly measured. It is desirable to measure T directly (using a gauge) from an accuracy and response time perspective, but it is not necessary since it can be determined from other parameters. Recall, that once ω is set the $\% \text{-Fill}$ defines T . Consider Figure 10-1, which is a functional diagram of a typical engine-dynamometer system with several possible information signals and component arrangements, where p represents pressure and Q represents a liquid flow rate.

The torque can be computed based on ω and $\% \text{-Fill}$, which can be determined from a tachometer and the dynamometer shell pressure (p) respectively once the system is properly calibrated. The relationship between p and $\% \text{-Fill}$ was discussed in Chapter 7 and 8. If a torque increase is desired at a fixed speed, then the dynamometer $\% \text{-Fill}$ must be increased. This is accomplished by opening the supply valve and increasing the liquid feed-water flow rate (Q). Conversely, to reduce torque the $\% \text{-Fill}$ must be decreased, by reducing the feed-water rate. To reduce T as fast as possible, the feed water is shut off entirely while the dynamometer quickly boils off the water in the working compartment. If this torque reduction rate is too slow, then a drainage valve can be used to dump liquid water into a sink.

Once the flow control valve(s) and pressure transducer are properly calibrated, programs can be written (and executed by a computer) for individual test scenarios, that interface with the engine controller and adjust the $\% \text{-Fill}$. The computer would produce the appropriate actuation signals based on the particular program, and/or information from the engine speed-controller and real-time data feedback/acquisition system, as conceptually represented in Figure 10-1. Any number of programs can be written that each carry out a different test scenario. For example a program can be written that slowly accelerates the engine to a typical operating speed and load. While another program requires the engine to go from idle to a condition of maximum speed and load in a very short time. The possible scenarios are unlimited. However, programs cannot be written until a particular engine-dynamometer system and control scheme are designed, which is outside the scope of this thesis.

CHAPTER 11

Conclusions

11.1 Summary of Results

The main contribution of the work presented in this thesis is the development of a new type of fluid dynamometer that functions by generating a high speed recirculating liquid flow in which shear stress induced dissipation is the primary power absorption mechanism. In addition to defining the conceptual framework for this new turbomachine, a flow model, blading algorithm, and numerical programs were developed that form the basis of a rigorous general algorithm that can be used to design dynamometers that function in this way, and to predict power absorption as a function of rotor speed (ω) and liquid level (*%-Fill*). Furthermore, the fundamental liquid flow features that characterize this device have been experimentally verified using linear blade cascades and a low-speed prototype. From this body of work a high-power-density full-scale dynamometer was designed that is more portable, has a wide operational range, and is expected to have a longer mechanical life, than conventional or commercially available machines.

The main features that characterize the operation of this dynamometer are summarized as follows. Through a unique blading scheme and working compartment configuration a high speed recirculating liquid flow is generated inside the dynamometer that absorbs a significant amount of power, primarily by viscous dissipation, while minimizing mechanical wear and erosion. The flow can be envisioned as a sheet of liquid that helically swirls around on the inside surface of a torus. The inside part of the torus is the rotor which acts to accelerate the flow, while the outside part is the stator which takes water from the rotor outlet and redirects it back into the inlet side of the rotor thus forming a closed loop. The flow accelerates to a point where shear stress induced viscous dissipation in the liquid flow matches (approximately) the rotor power input. As power is absorbed a portion of this high speed recirculating liquid flow boils off, which must be replaced by make-up feed-water to maintain steady flow conditions. However, since the fluid streamlines are highly twisted there is a significant centrifugal field imparted on the flow, which produces a strong radial pressure gradient. Thus, boiling is confined to a relatively thin layer near the free surface, and the vapor and liquid are self phase separating, resulting in the generation of a vapor core that is surrounded by a toroidal liquid sheet. The blades provide a means of

accessing the nearly pure vapor region, which is a significant design advantage because it reduces the amount of feed-water required.

A basic flow model and blading algorithm was developed to define (in terms of turning and rake angles) the appropriate blade shapes that generate the desired flow. Based on this, a numerical code (Dynamometer Code) was developed that can be used to make performance estimates for the dynamometer, and quantitatively analyze the effect of parameter variations. Furthermore, the blading algorithm was used to develop rotor and stator blade generation programs. The Dynamometer Code and blade generation programs form the basis of a rigorous general algorithm that can be used to design dynamometers that absorb power predominantly by viscous dissipation.

To test the validity of the general algorithm and programs a flow visualization experiment was conducted and a low-speed prototype was designed, built, and tested. The experimental results confirm the basic flow and agree quite well with the predicted behavioral trends, but actual power absorption levels were lower than anticipated. This is largely due to the fact that the observed friction factor was approximately 75% lower than predicted. Some possible reasons for this were identified, such as the inclusion of air bubbles in the liquid flow, uncertainty in the low-speed prototype's surface roughness, and of course the fact that the predicted friction factors are based on fully wet conduit flow. However, the measured non-dimensional performance data (presented in Figure 8-9) confirmed the hypothesis that P^* , defined in Chapter 6, rapidly approaches a constant value as Re increases (*for a fixed %-Fill*). In general, the experimental results are undeniably positive and supportive of the basic flow model and blading algorithm.

No attempt was made here to generate steam due to material limitations. However, since the radial pressure gradients across the liquid sheet are expected to be very large, boiling will occur predominantly in a relatively thin layer near the free surface, and thus should not significantly alter the basic fluid dynamics. Therefore, the algorithms and predictive tools developed in this thesis, as well as the experimental results, are applicable to the design of high-speed full-scale steam generating dynamometers such as the one presented in Chapter nine.

The full-scale dynamometer has a 7 inch outside diameter and is estimated to weigh less than 50 pounds. The maximum active volume, defined as the working volume of liquid inside the dynamometer (*at 100 %-Fill*), is approximately 28 cubic inches. The rotor and

stator blades have an approximate turning angle (β) of 32 degrees. The rotor blade rake angle (ψ) varies throughout the stage between approximately 35° at the inlet and 0° at the outlet, while the stator blade ψ varies between approximately 15° at the inlet and 0° at the outlet. It is typical for the rotor blades to be more twisted because of the toroidal geometry and acceleration terms associated with the angular motion of the rotor.

The full-scale maximum power absorption is estimated to be 4,400 hp at 16,000 rpm. The estimated dimensionless power P^* is 1.8 at this speed (*and 100 %-Fill*), as well as over a wide range of rotor speeds, because P^* changes very little with Re (at relatively high rotor speeds) as was shown in Figure 6-1 and 8-9. The power absorption can also be expressed in terms of various parameters. In terms of a power to weight ratio, the dynamometer can absorb 88 hp/lb at 16,000 rpm (through purely viscous dissipation). In terms of the active volume (defined above) the dynamometer can absorb 157 hp/in³ at 16,000 rpm. These values were calculated based on the estimated power absorption generated from the Dynamometer Code, which should be thought of as an upper limit. A good lower limit can be defined by applying the results of the low-speed experiment, or modifying the estimated power as done in Chapter 9. Recall that the measured friction factor was 25% of the estimated values. Applying this to the estimated power absorption results in a *modified estimated* absorption of 1,100 hp at 16,000 rpm, or a P^* of 0.45. Thus, the corresponding modified estimated power to weight ratio and power to active volume ratio is 22 hp/lb and 39 hp/in³, respectively. Of course, the actual power absorption will be somewhere between the lower and upper limits depending on what the actual full-scale friction factor turns out to be.

Even if the actual high-speed full-scale power absorption is close to the lower limit, the power density is still quite high in comparison to other typical hydraulic dynamometers. For example, a typical cavitating disc type machine can absorb approximately 16 hp/in³, a typical Froude type dynamometer can absorb approximately 24 hp/in³, and the prototype tested by Textron-Lycoming can absorb approximately 31 hp/in³ at the same rotor speed (where the values presented here are extrapolations based on information obtained in the literature and from Textron-Lycoming, and are used here solely for making rough comparisons). Clearly, the dynamometer developed here has a higher power density than other similar devices. What is more, this machine has lower feed-water requirements than these other hydraulic dynamometers (for reasons cited above) which contributes to its portability. Also, since the dissipation mechanism in this device is distributed over the

entire wetted surface area, the dynamometer is expected to have a longer mechanical life than other comparable machines.

11.2 Future Work

Since this dynamometer, particularly the blading and resulting liquid flow inside, is new and quite unique there is the opportunity for significant future, experimental, theoretical, and computational work. There is a real challenge to figure out how to computationally model this complex 3-D flow since there are several physical elements that must be included. The most important of which are the strong centrifugal field, localized boiling, secondary flow, free surface, and blade waves and wakes. On the experimental front the next task is to build and test a full-scale prototype, to ensure that the flow maintains its integrity at high rotor speeds (on the order of *10,000 rpm*) while generating steam. Then several different experimental dynamometers should be constructed to generate a broad spectrum of data, from which accurate correlations can be developed, particularly for the friction factor which is the parameter that has the most uncertainty. Other issues such as design optimization and rapid torque control strategies can be addressed theoretically, or numerically, which would produce additional useful information and increase the utility of this device. Of course, to advance any new technology requires an iterative process involving theoretical and numerical development, as well as experimentation.

This thesis provides a basis, and the motivation, to generate interest and continued work in this area. Although the thesis develops a turbomachine for use as a dynamometer, this type of device and theory can be easily adapted for other applications. For example, the device could be modified and used as a compact steam generator, or as a high pressure water supply. Furthermore, the blading algorithm can perhaps be used to develop a new generation of torque converters or fluid couplings that operate more efficiently by adjusting liquid level. Many other applications can be envisioned.

References / Bibliography

1. Courtney, W.J., "Water Brake Status (Considering Cavitation)", ASME Fluids Engineering Division, Oak Park, Illinois (1989)
2. Raine, J.K., "General Theory and Computer Simulation for F-type Dynamometer Performance", Froude Engineering Ltd. Technical Note 168, England (1979)
3. Shute, A.C., "Water Brake Converter: A Simple Device to Convert Mechanical Energy into Heat Energy", DoE Final Report/R1/10354-T1, April (1984)
4. Patki, G.S., and Gill, B.S., "The Effect of Number of Blades on the Performance of Hydrodynamic Couplings and Dynamometers", Central Mechanical Engineering Research Institute, vol. 7, No 3, (1976)
5. Raine, J.K., and Hodgson, P.G., "Computer Simulation of a Variable Fill Hydraulic Dynamometer, Part 1", Proc Instn Mech Engrs, vol. 205, (1991)
6. Rohsenow, W.M., and Choi, H.Y., "Heat, Mass, and Momentum Transfer", Ch. 4, Pg. 57-61, Prentice-Hall, Englewood Cliffs, NJ, (1961)
7. Lewis, E.V. (Editor), "Principles of Naval Architecture Second Revision", vol. II, The Society of Naval Architects and Marine Engineers, Pg. 12-13 (ITTC model-ship correlation), Jersey City, NJ, circa (1980)
8. Froude, W., "On a New Dynamometer for Measuring the Power Delivered to the Screws of Large Ships", Proc. Instn. Mech. Engrs., July (1877)
9. Wallace, F.J., Whitfield, A., and Sivalingam, R., "A theoretical Model for the Performance Prediction of Fully Filled Fluid Couplings", Univ. of Bath, (1977)
10. Cravalho, E.G. and Smith. J.L., Jr., "Engineering Thermodynamics", E.G. Cravalho and J.L. Smith, Jr., (1992)
11. Potter, M.C. and Foss, J.F., "Fluid Mechanics", Grate Lakes Press, Okemos, MI, (1982)
12. White, F.M., "Viscous Fluid Flow", McGraw-Hill, New York, NY, (1991)

Biographical Note

In secondary school Edward J. Ognibene was most interested in art — painting, illustration and drafting. In fact, he thought he wanted to study art at perhaps Pratt School of Design or Cooper Union. However, towards the end of High School he began to wonder if art was really what he wanted to do for a career. To be prudent he decided to enter a more general university instead of an art school.

In September of 1983 he began his college career in the Liberal Arts program at the University of Bridgeport, in Connecticut. Over the course of several semesters he dabbled in different areas, such as Graphic Arts and Industrial design, to see what he was good at and enjoyed enough to make a career out of. Finally, he arrived at Mechanical Engineering, an area that requires creativity and is also in demand by industry. After making up the prerequisite math and science courses he was accepted into the Mechanical Engineering Department at UB. He soon realized that engineering was not one of the universities long suits. However, he knew of a great engineering school across the Long Island Sound, so he applied to the ME department there.

In September of 1986 he enrolled in the ME Department at the State University of New York at Stony Brook, and focused his efforts on engineering. In Spring of 1987 he was recognized as an outstanding engineering student and was honored by being elected into *Tau Beta Pi*, the National Engineering Honor Society. Then in Fall 1988 he was honored again when he was presented the *Grumman Award* for academic excellence. Finally, in May 1989 he graduated *Magna Cum Laude* with a Bachelor of Engineering in Mechanical Engineering.

He enrolled in the Mechanical Engineering Department at MIT, as a Graduate Student, in September 1989. He received his Master of Science in Mechanical Engineering in 1991, after which he took a leave of absence to acquire some industrial experience. He returned to MIT in the Fall of 1992 and was admitted into the doctoral program in the Spring of 1993. In 1994 he was honored by being elected into *Sigma Xi*, the Scientific Research Honor Society. Finally, in 1995 he received his Doctor of Philosophy after satisfying all of the institute requirements and successfully defending his thesis work.

APPENDICES

APPENDIX A

Flow Visualization — Procedures & Raw Data

Experimental Procedures.

The flow visualization experiment was broken up into nine procedures. Each procedure focused on a specific part of the experiment, in which either the *2U* or *3U Test Section* was exclusively used. Further, in an attempt to minimize confusion, the photographs and video tape have been organized in the same way. The nine procedures are listed below, followed by a short paragraph explaining the experimental procedure and configuration.

PROCEDURE 1. Jet velocity variation at short range. With the *3U Test Section* mounted flush against the Nozzle, with 0° relative angle, the jet speed was varied (from low to high) to determine the flow behavior and dependence on speed. Further, the Test Section was translated back and forth to determine how the blunt blades performed in comparison to the sharp blades.

PROCEDURE 2. Jet velocity variation at short range. With the *2U Test Section* mounted flush against the Nozzle, with 0° relative angle, the jet speed was varied (from low to high) to determine the flow behavior and dependence on speed. Further, the Test Section was translated back and forth to determine how the blunt blades performed in comparison to the sharp blades.

PROCEDURE 3. Jet velocity variation at long range. With the *3U Test Section* mounted 9 cm away from the Nozzle, with 0° relative angle, the jet speed was varied (from low to high) to determine the flow behavior and dependence on speed. Pitot tube measurements were made to validate the Nozzles pressure gage. Further, the Test Section was translated back and forth to determine how the blunt blades performed in comparison to the sharp blades.

PROCEDURE 4. Jet velocity variation at long range. With the *2U Test Section* mounted 9 cm away from the Nozzle, with 0° relative angle, the jet speed was varied (from low to high) to determine the flow behavior and dependence on speed. Further, the Test Section was translated back and forth to determine how the blunt blades performed in comparison to the sharp blades.

PROCEDURE 5. Jet velocity and positive angular variation at medium range. With the *3U Test Section* mounted 4 cm away from the Nozzle the relative angle was varied, from 0° to 40° , to determine the effect on flow behavior. At angular positions of 0° , 15° , 25° , and 40° , the jet speed was varied to determine the dependence on flow speed. Further, the Test Section was translated back and forth to determine how the blunt blades performed in comparison to the sharp blades.

PROCEDURE 6. Jet velocity and positive angular variation at medium range. With the *2U Test Section* mounted 4 cm away from the Nozzle the relative angle was varied, from 0° to 40° , to determine the effect on flow behavior. At angular positions of 0° , 15° , 25° , and 40° , the jet speed was varied to determine the dependence on flow speed. Further, the Test Section was translated back and forth to determine how the blunt blades performed in comparison to the sharp blades.

PROCEDURE 7. Jet velocity and negative angular variation at medium range. With the *3U Test Section* mounted 4 cm away from the Nozzle the relative angle was varied, from 0° to -40° , to determine the effect on flow behavior. At angular positions of 0° , -13° , -23° , and -40° , the jet speed was varied to determine the dependence on flow speed. Further, the Test Section was translated back and forth to determine how the blunt blades performed in comparison to the sharp blades.

PROCEDURE 8. Jet velocity and negative angular variation at medium range. With the *2U Test Section* mounted 4 cm away from the Nozzle the relative angle was varied, from 0° to -40° , to determine the effect on flow behavior. At angular positions of 0° , -13° , -22° , and -40° , the jet speed was varied to determine the dependence on flow speed. Further, the Test Section was translated back and forth to determine how the blunt blades performed in comparison to the sharp blades.

PROCEDURE 9. Multi-parameter variation at short range. With the *2U Test Section* mounted 3 cm away from the Nozzle, a variety of parameters were varied. The Test Section angular position was varied from -35° to $+35^\circ$. At angular positions of -15° , 0° , and $+15^\circ$, the jet speed was varied over the full range to observe the effect. Further, at low, medium, and high jet speeds, dye was injected into the flow to determine the mixing behavior caused by, among other things, secondary flow. The Test Section was also translated to explore the effect of sharp blades. Pitot tube measurements were made to validate the nozzle's pressure gage, so that accurate velocity calculations can be made.

Experimental Data

Procedure #	Nozzle Offset (cm)	Nozzle Angle	Free Surface Angle	Nozzle Pressure (psi)	Pitot tube Pressure (psi)	Recirculation Factor, k	Comments
1	1 Flush	0°	0°	1-11	-	3	No destabilization of flow over full velocity range.
2	1 Flush	0°	0°	1-10	-	2	No destabilization of flow over full velocity range.
3	10 Long	0°	0°	1-10	1-10	3	Jet begins to expand but then re-collapses in the Test Section
4	10 Long	0°	0°	1-10	1-9	2	Same behavior observed in procedure 3. Jet reorganizes in vanes
5	5 Med.	0°-15° 15°-25° 25°-40°	0°-25° 25°-40° 40°-55°	1-10	1-11	3	Very well behaved up to 15° with no overflow. Mid-range -- some overflow. Near 40° -- more overflow.
6	5 Med.	0°-15° 15°-25° 25°-40°	0°-25° 25°-40° 40°-55°	1-10	1-10	2	Very well behaved up to 15° with no overflow. Mid-range -- some overflow. Near 40° -- more overflow.
7	5 Med.	0°--13° -13°--23° -23°--40°	0°--25° -25°--40° -40°--55°	1-11	1-10	3	Very well behaved up to -13° with no overflow. Mid-range -- some overflow. Near -40° -- more overflow.
8	5 Med.	0°--13° -13°--22° -22°--40°	0°--25° -25°--40° -40°--55°	1-10	1-10	2	Very well behaved up to -13° with no overflow. Mid-range -- some overflow. Near -40° -- more overflow.
9	4 Short	-35°--35°	-	2.5-9 Peak 13	3-10 Peak 14	2	Very well behaved btwn -15° to 15°. Flow behavior in T.S. is invariant with jet velocity. Flow is robust with respect to Nozzle gap, jet velocity, moderate angle change. Dye mixed well all speeds, l=3cm.

APPENDIX B

Appendix B.1 **Base Curve Generation (FORTRAN)**

ROTOR BLADE BASE CURVE DEVELOPMENT

- c Created by Edward J. Ognibene
- c Output is x=x', y', and z'
- c Will get (N+1) data points out of this program.

```
real*8 R1,Rt,Rm,x,y,z,s,b,a,arg,l,pi,alpha,angle,g,dg,r
real*8 v(1:2),h(1:2),theta
integer i,j,N
```

```
open(10, file='t_rot.out')
```

```
pi = 3.141592654
```

```
write(*,*) 'x ','y ','z '
write(*,*) 'enter torus minor radius, R1:'
read(*,*) R1
write(*,*) 'enter torus major radius, Rm:'
read(*,*) Rm
write(*,*) 'enter N (even numbers only)'
read(*,*) N
write(*,*) 'enter beta (deg)'
```

- c alpha=beta
- ```
read(*,*) alpha
write(10,*) ' N = ',N
write(10,*) ' alpha = ',alpha,' deg'
```

```
Rt = Rm - R1
```

```
write(10,*) ' minor radius, R1 = ',R1
write(10,*) ' major radius, Rm = ',Rm
write(10,*) ' x ','y ','z '
write(*,*) ' x ','y ','z '
```

```
alpha = alpha*pi/180.0
```

```
s = pi*R1
a = s/dsin(alpha)
b = a
l = a*dcos(alpha)
write(*,*) ' l=',l
dg = pi/DBLE(N)
g = 0.0
x = 0.0
y = 0.0
z = a-l
```

- c \*\*\* Transformation Block, cylindrical to toroidal, begins here \*\*\*\*\*
 

```

r = Rt + R1 - y
angle = datan(z/Rt)
y = y + r*(1.0-dcos(angle))
z = R*dsin(angle)

```
- c \*\*\* End of transformation block \*\*\*\*\*

```

write(*,*) ' z=',z
PAUSE 'to continue --> press <enter>'
write(*,*) x,-y,z
write(10,*) x,-y,z

do 10 i = 1, N/2
 g = g + dg
 s = g*R1
 x = R1*(1.0-dcos(g))
 y = R1*dsin(g)
 z = ((a**2)*(1.0-(s/b)**2))**0.5
 z = z - l
c *** Transformation Block, cylindrical to toroidal, begins here *****
 r = Rt + R1 - y
 angle = datan(z/Rt)
 y = y + r*(1.0-dcos(angle))
 z = R*dsin(angle)
c *** End of transformation block *****
 write(*,*) x,-y,z
 write(10,*) x,-y,z
10 continue
do 20 i = 1, N/2
 g = g + dg
 s = g*R1
 x = R1*(1.0-dcos(g))
 y = R1*dsin(g)
 z = ((a**2)*(1.0-(s/b)**2))**0.5
 z = z - l
c *** Transformation Block, cylindrical to toroidal, begins here *****
 r = Rt + R1 - y
 angle = datan(z/Rt)
 y = y + r*(1.0-dcos(angle))
 z = R*dsin(angle)
c *** End of transformation block *****
 if(i.eq.((N/2)-1)) then
 v(1) = y
 h(1) = z
 end if
 if(i.eq.((N/2))) then
 v(2) = y
 h(2) = z
 theta = datan((h(1)-h(2)) / (v(1)-v(2)))
 end if
 write(*,*) x,-y,z
 write(10,*) x,-y,z
20 continue
theta = 180.0*theta/pi
write(*,*) ' theta = ',theta,' deg'
write(10,*) ' theta = ',theta,' deg'
write(10,*) 'done...'

stop 'program finished'
end

```



## STATOR BLADE BASE CURVE DEVELOPMENT

- c Created by Edward J. Ognibene.
- c Output is  $x=x'$ ,  $y'$ , and  $z'$
- c Will get  $(2N+1)$  data points out of this program.

```
real*8 R1,R2,x,y,z,s,b,a,arg,pi,theta,alpha,g,dg,r,angle
real*8 v(1:2),h(1:2),beta
integer i,j,N
```

```
open(10, file='t_stat.out')
```

```
pi = 3.141592654
```

```
write(*,*) 'enter torus minor radius, R1:'
read(*,*) R1
write(*,*) 'enter torus major radius, Rm:'
read(*,*) Rm
write(*,*) 'enter N (even numbers only):'
read(*,*) N
write(*,*) 'enter beta (deg)'
```

- c alpha=beta
- ```
read(*,*) alpha
write(10,*) ' N = ',N
write(10,*) ' alpha = ',alpha,' deg'
```

```
Rt = Rm - R1
```

```
write(10,*) ' minor radius, R1 = ',R1
write(10,*) ' major radius, Rm = ',Rm
write(10,*) ' x ',' y ',' z '
write(*,*) ' x ',' y ',' z '
```

```
alpha = alpha*pi/180.0
```

```
s = pi*R1
a = s/dsin(alpha)
b = s
dg = pi/DBLE(N)
g = 0.0
x = 0.0
y = 0.0
z = a*(1-dcos(alpha))
```

- c ***** Transformation Block, cylindrical to toroidal, begins here *******
- ```
r = Rm + y
angle = datan(z/Rt)
y = -y + r*(1.0-dcos(angle))
z = r*dsin(angle)
```
- c **\*\*\* End of transformation block \*\*\*\*\***

```
v(1) = -y
```

```

h(1) = z

beta = -datan(z/(-Rm-v(1)))
beta = 180.0*beta/pi

write(*,*) ' z=' ,z
PAUSE 'to continue --> press <enter>'
write(*,*) x,-y,z
write(10,*) x,-y,z

do 10 i = 1, N/2
 g = g + dg
 s = g*R1
 x = R1*(1.0-dcos(g))
 y = R1*dsin(g)
 z = a-((a**2)-(s-b)**2)**0.5
c *** Transformation Block, cylindrical to toroidal, begins here *****
 r = Rm + y
 angle = datan(z/Rt)
 y = -y + r*(1.0-dcos(angle))
 z = r*dsin(angle)
c *** End of transformation block *****
 if(i.eq.1) then
 v(2) = -y
 h(2) = z
 theta = datan((h(2)-h(1)) / (v(2)-v(1)))
 end if
 write(*,*) x,-y,z
 write(10,*) x,-y,z
10 continue
do 20 i = 1, N/2
 g = g + dg
 s = g*R1
 x = R1*(1.0-dcos(g))
 y = R1*dsin(g)
 z = a-((a**2)-(s-b)**2)**0.5
c *** Transformation Block, cylindrical to toroidal, begins here *****
 r = Rm + y
 angle = datan(z/Rt)
 y = -y + r*(1.0-dcos(angle))
 z = r*dsin(angle)
c *** End of transformation block *****
 write(*,*) x,-y,z
 write(10,*) x,-y,z
20 continue
theta = 180.0*theta/pi
write(*,*) ' theta = ',-theta+beta,' deg'
write(10,*) ' theta = ',-theta+beta,' deg'
write(10,*) 'done...'

stop 'program finished'
end

```

**Appendix B.2**  
**Inner Curve Generation (Math Cad)**



"v) - is a vector to a point on the base curve"

$$v(a) := \begin{bmatrix} x_a \\ y_a \\ z_a \end{bmatrix}$$

$$v(1) = \begin{pmatrix} 0 \\ -0.293 \\ 1.174 \end{pmatrix}$$

$$v(2) = \begin{pmatrix} 0.001 \\ -0.339 \\ 1.149 \end{pmatrix}$$

$$v(3) = \begin{pmatrix} 0.005 \\ -0.385 \\ 1.124 \end{pmatrix}$$

$$b := 1..N - 1$$

$$d(b) := v(b) - v(b + 1)$$

$$d(1) = \begin{pmatrix} -0.001 \\ 0.046 \\ 0.025 \end{pmatrix}$$

$$d(2) = \begin{pmatrix} -0.004 \\ 0.046 \\ 0.025 \end{pmatrix}$$

$$Du(b) := \frac{d(b)}{|d(b)|}$$

$$Du(1) = \begin{pmatrix} -0.026 \\ 0.88 \\ 0.474 \end{pmatrix} \text{ Unit vector}$$

$$Vrel(b) := (k \cdot Rm \cdot w) \cdot Du(b)$$

$$Vrel(1) = \begin{bmatrix} -205.042 \\ 6.895 \cdot 10^3 \\ 3.712 \cdot 10^3 \end{bmatrix}$$

Velocities are in (in/s)

$$\phi(b) := \arccos\left(1 - \frac{x_b}{R}\right)$$

$$\phi(2) = 0.052$$

$$y1(b) := R \cdot \sin(\phi(b))$$

$$\phi(1) = 0$$

$$y1(1) = 0$$

$$y1(2) = 0.052$$

$$r2(b) := Rm - y1(b) \text{ inches}$$

$$r2(1) = 2.5$$

$$r2(2) = 2.448$$

$$xi_b := 0.0$$

$$yi_b := -Rm - y_b$$

$$zi_b := -z_b$$

$$io(b) := \begin{bmatrix} xi_b \\ zi_b \\ (-yi)_b \end{bmatrix}$$

$$xi_2 = 0$$

$$yi_2 = -2.161$$

$$zi_2 = -1.149$$

$$io(2) = \begin{pmatrix} 0 \\ -1.149 \\ 2.161 \end{pmatrix}$$

$$io(b) := \frac{io(b)}{|io(b)|}$$

$$io(2) = \begin{pmatrix} 0 \\ -0.47 \\ 0.883 \end{pmatrix} \text{ unit vector}$$

$$Vabs(b) := Vrel(b) + (r2(b) \cdot w) \cdot io(b)$$

$$Vabs(2) = \begin{bmatrix} -614.504 \\ 4.914 \cdot 10^3 \\ 7.39 \cdot 10^3 \end{bmatrix}$$

$$Vmag(b) := |Vabs(b)|$$

$$Vmag(2) = 8.895 \cdot 10^3$$

$$Vunit(b) := \frac{Vabs(b)}{|Vabs(b)|}$$

$$Vunit(2) = \begin{pmatrix} -0.069 \\ 0.552 \\ 0.831 \end{pmatrix}$$

$$c := 1..N - 2$$

$$Vave(c) := 0.5 \cdot (Vmag(c) + Vmag(c + 1))$$

$$Dtot(c) := |d(c)| + |d(c + 1)|$$

$$\Delta t(c) := \frac{Dtot(c)}{Vave(c)}$$

$$Vave(1) = 8.898 \cdot 10^3$$

$$Dtot(1) = 0.105$$

$$\Delta t(1) = 1.177 \cdot 10^{-5}$$

$$A1(c) := \left( \frac{Vmag(c) - Vmag(c + 1)}{\Delta t(c)} \right) \cdot Vunit(c)$$

$$A2(c) := \left( \frac{Vmag(c)}{\Delta t(c)} \right) \cdot (Vunit(c) - Vunit(c + 1))$$

$$A(c) := A1(c) + A2(c)$$

$$Au(c) := \frac{A(c)}{|A(c)|}$$

$$Au(1) = \begin{pmatrix} 0.998 \\ 0.033 \\ 0.05 \end{pmatrix}$$

$$Au(2) = \begin{pmatrix} 0.994 \\ 0.073 \\ 0.085 \end{pmatrix}$$

$$A(1) = \begin{bmatrix} 3.482 \cdot 10^7 \\ 1.163 \cdot 10^6 \\ 1.755 \cdot 10^6 \end{bmatrix}$$

$$A(2) = \begin{bmatrix} 3.454 \cdot 10^7 \\ 2.56 \cdot 10^6 \\ 2.952 \cdot 10^6 \end{bmatrix}$$

Components of the Total derivative

$$m = 0.8$$

$$Ci(c) := m \cdot Au(c)$$

$$zi(c) := v(c + 1) + Ci(c)$$

$$Ci(1) = \begin{pmatrix} 0.799 \\ 0.027 \\ 0.04 \end{pmatrix}$$

$$zi(1) = \begin{pmatrix} 0.8 \\ -0.312 \\ 1.189 \end{pmatrix}$$

"zi" - is a vector to a point on the inner curve, from (0,0,0)"

"It is oriented along the principle curvature vector and has a magnitude equal to m, calculated above."

$$xi(c) := zi(c)_1$$

$$xi(1) = 0.8$$

$$yi(c) := zi(c)_2$$

$$yi(1) = -0.312$$

$$zzi(c) := zi(c)_3$$

$$zzi(1) = 1.189$$

xi(c)<sub>1</sub>

|       |
|-------|
| 0.8   |
| 0.8   |
| 0.802 |
| 0.803 |
| 0.805 |
| 0.808 |
| 0.812 |
| 0.816 |
| 0.821 |

zi(c)<sub>2</sub>

|        |
|--------|
| -0.312 |
| -0.326 |
| -0.339 |
| -0.352 |
| -0.364 |
| -0.375 |
| -0.385 |
| -0.395 |
| -0.404 |

zi(c)<sub>3</sub>

|       |
|-------|
| 1.189 |
| 1.192 |
| 1.193 |
| 1.193 |
| 1.192 |
| 1.19  |
| 1.187 |
| 1.182 |
| 1.177 |

|       |
|-------|
| 0.833 |
| 0.839 |
| 0.846 |
| 0.854 |
| 0.862 |
| 0.87  |
| 0.878 |
| 0.887 |
| 0.896 |
| 0.904 |
| 0.912 |
| 0.921 |
| 0.928 |
| 0.936 |
| 0.943 |
| 0.949 |
| 0.955 |
| 0.961 |
| 0.966 |
| 0.971 |
| 0.976 |
| 0.981 |
| 0.986 |
| 0.991 |
| 0.997 |
| 1.004 |
| 1.012 |
| 1.021 |
| 1.032 |
| 1.044 |
| 1.059 |
| 1.075 |
| 1.093 |
| 1.114 |
| 1.136 |
| 1.16  |
| 1.185 |
| 1.212 |
| 1.24  |
| 1.269 |

|        |
|--------|
| -0.418 |
| -0.423 |
| -0.427 |
| -0.43  |
| -0.432 |
| -0.432 |
| -0.431 |
| -0.429 |
| -0.425 |
| -0.42  |
| -0.414 |
| -0.407 |
| -0.399 |
| -0.39  |
| -0.38  |
| -0.37  |
| -0.36  |
| -0.349 |
| -0.339 |
| -0.33  |
| -0.321 |
| -0.313 |
| -0.307 |
| -0.303 |
| -0.3   |
| -0.299 |
| -0.301 |
| -0.304 |
| -0.31  |
| -0.317 |
| -0.326 |
| -0.337 |
| -0.349 |
| -0.361 |
| -0.375 |
| -0.388 |
| -0.401 |
| -0.413 |
| -0.425 |
| -0.435 |

|        |
|--------|
| 1.162  |
| 1.153  |
| 1.143  |
| 1.132  |
| 1.119  |
| 1.105  |
| 1.09   |
| 1.074  |
| 1.056  |
| 1.036  |
| 1.015  |
| 0.992  |
| 0.968  |
| 0.941  |
| 0.913  |
| 0.882  |
| 0.849  |
| 0.814  |
| 0.777  |
| 0.738  |
| 0.696  |
| 0.652  |
| 0.607  |
| 0.56   |
| 0.511  |
| 0.461  |
| 0.409  |
| 0.358  |
| 0.306  |
| 0.255  |
| 0.204  |
| 0.154  |
| 0.105  |
| 0.057  |
| 0.012  |
| -0.032 |
| -0.074 |
| -0.114 |
| -0.152 |
| -0.189 |

WRITEPRN(rotor) := zi(c)<sub>1</sub>

APPENDPRN(rotor) := zi(c)<sub>2</sub>

APPENDPRN(rotor) := zi(c)<sub>3</sub>

# STATOR BLADE INNER CURVE DEVELOPMENT

ORIGIN := 1      PRNCOLWIDTH := 17      PRNPRECISION := 15.      STATOR.MCD

N := 61      R := 1.00    minor radius (in)      a := 1..N      m := 0.90-R

$x_a := \text{READ}(xs)$

$y_a := \text{READ}(ys)$

$z_a := \text{READ}(zs)$

| $x_a$ | $y_a$  | $z_a$ |
|-------|--------|-------|
| 0     | -0.293 | 1.174 |
| 0.001 | -0.229 | 1.165 |
| 0.005 | -0.166 | 1.155 |
| 0.012 | -0.102 | 1.143 |
| 0.022 | -0.039 | 1.13  |
| 0.034 | 0.023  | 1.116 |
| 0.049 | 0.085  | 1.099 |
| 0.066 | 0.146  | 1.082 |
| 0.086 | 0.205  | 1.063 |
| 0.109 | 0.264  | 1.043 |
| 0.134 | 0.321  | 1.021 |
| 0.161 | 0.376  | 0.998 |
| 0.191 | 0.43   | 0.974 |
| 0.223 | 0.482  | 0.949 |
| 0.257 | 0.532  | 0.922 |
| 0.293 | 0.58   | 0.895 |
| 0.331 | 0.625  | 0.867 |
| 0.371 | 0.668  | 0.838 |
| 0.412 | 0.709  | 0.809 |
| 0.455 | 0.747  | 0.779 |
| 0.5   | 0.782  | 0.748 |
| 0.546 | 0.814  | 0.717 |
| 0.593 | 0.844  | 0.686 |
| 0.642 | 0.871  | 0.655 |
| 0.691 | 0.894  | 0.624 |
| 0.741 | 0.915  | 0.592 |
| 0.792 | 0.933  | 0.561 |
| 0.844 | 0.947  | 0.53  |
| 0.895 | 0.959  | 0.5   |
| 0.948 | 0.967  | 0.47  |
| 1     | 0.972  | 0.44  |
| 1.052 | 0.974  | 0.411 |
| 1.105 | 0.973  | 0.383 |
| 1.156 | 0.97   | 0.355 |
| 1.208 | 0.963  | 0.328 |
| 1.259 | 0.953  | 0.303 |
| 1.309 | 0.94   | 0.278 |
| 1.358 | 0.924  | 0.254 |
| 1.407 | 0.906  | 0.231 |
| 1.454 | 0.885  | 0.209 |
| 1.5   | 0.861  | 0.188 |
| 1.545 | 0.834  | 0.168 |
| 1.588 | 0.806  | 0.149 |
| 1.629 | 0.774  | 0.132 |
| 1.669 | 0.741  | 0.116 |
| 1.707 | 0.706  | 0.1   |
| 1.743 | 0.668  | 0.086 |
| 1.777 | 0.628  | 0.074 |
| 1.809 | 0.587  | 0.062 |
| 1.839 | 0.544  | 0.051 |



"v() - is a vector to a point on the base curve"

$$v(a) := \begin{bmatrix} x_a \\ y_a \\ z_a \end{bmatrix}$$

$$v(1) = \begin{pmatrix} 0 \\ -0.293 \\ 1.174 \end{pmatrix}$$

$$v(2) = \begin{pmatrix} 0.001 \\ -0.229 \\ 1.165 \end{pmatrix}$$

$$v(3) = \begin{pmatrix} 0.005 \\ -0.166 \\ 1.155 \end{pmatrix}$$

$$b := 1..N - 1$$

$$d(b) := v(b + 1) - v(b)$$

$$d(1) = \begin{pmatrix} 0.001 \\ 0.064 \\ -0.009 \end{pmatrix}$$

$$d(2) = \begin{pmatrix} 0.004 \\ 0.064 \\ -0.01 \end{pmatrix}$$

$$Dmag(b) := |d(b)|$$

$$Dmag(b) := \frac{1.0}{Dmag(b)}$$

$$Du(b) := Dmag(b) \cdot d(b)$$

$$Du(1) = \begin{pmatrix} 0.021 \\ 0.99 \\ -0.136 \end{pmatrix}$$

$$c := 1..N - 2$$

$$Cv(c) := Du(c + 1) - Du(c)$$

"curvature vector"

$$Cv(1) = \begin{pmatrix} 0.042 \\ -0.005 \\ -0.022 \end{pmatrix}$$

$$mag(c) := |Cv(c)|$$

$$mag(1) = 0.048$$

$$magI(c) := \frac{1.0}{mag(c)}$$

$$magI(1) = 20.85i$$

$$Cu(c) := magI(c) \cdot Cv(c)$$

$$m = 0.8 \text{ inches}$$

$$Cu(1) = \begin{pmatrix} 0.882 \\ -0.106 \\ -0.458 \end{pmatrix}$$

$$Ci(c) := m \cdot Cu(c)$$

$$zi(c) := v(c + 1) + Ci(c)$$

$$Ci(1) = \begin{pmatrix} 0.706 \\ -0.085 \\ -0.367 \end{pmatrix}$$

$$zi(1) = \begin{pmatrix} 0.707 \\ -0.314 \\ 0.799 \end{pmatrix}$$

"zi() - is a vector to a point on the inner curve, from (0,0,0)"

"It is oriented along the principle curvature vector and has a magnitude equal to m, calculated above."

$$xi(c) := zi(c)_1$$

$$yi(c) := zi(c)_2$$

$$zzi(c) := zi(c)_3$$

$$xi(1) = 0.707$$

$$yi(1) = -0.314$$

$$zzi(1) = 0.799$$

$z_i(c)_1$   
 0.707  
 0.704  
 0.702  
 0.703  
 0.705  
 0.709  
 0.714  
 0.722  
 0.731  
 0.741  
 0.754  
 0.767  
 0.782  
 0.798  
 0.815  
 0.834  
 0.852  
 0.872  
 0.892  
 0.912  
 0.933  
 0.954  
 0.975  
 0.995  
 1.015  
 1.035  
 1.054  
 1.073  
 1.091  
 1.108  
 1.124  
 1.139  
 1.153  
 1.167  
 1.179  
 1.19  
 1.199  
 1.208  
 1.216  
 1.223  
 1.228  
 1.233  
 1.237  
 1.24  
 1.242  
 1.244  
 1.245  
 1.245  
 1.245  
 1.244

$z_i(c)_2$   
 -0.314  
 -0.289  
 -0.264  
 -0.239  
 -0.214  
 -0.188  
 -0.163  
 -0.138  
 -0.113  
 -0.089  
 -0.065  
 -0.042  
 -0.019  
 0.002  
 0.023  
 0.042  
 0.061  
 0.078  
 0.094  
 0.109  
 0.123  
 0.135  
 0.146  
 0.155  
 0.164  
 0.17  
 0.176  
 0.18  
 0.183  
 0.185  
 0.186  
 0.185  
 0.184  
 0.182  
 0.179  
 0.175  
 0.171  
 0.166  
 0.16  
 0.154  
 0.148  
 0.142  
 0.135  
 0.128  
 0.121  
 0.114  
 0.106  
 0.099  
 0.091  
 0.084

$z_i(c)_3$   
 0.799  
 0.785  
 0.773  
 0.761  
 0.75  
 0.739  
 0.728  
 0.719  
 0.709  
 0.7  
 0.691  
 0.682  
 0.673  
 0.665  
 0.657  
 0.648  
 0.64  
 0.632  
 0.624  
 0.616  
 0.608  
 0.6  
 0.591  
 0.583  
 0.575  
 0.567  
 0.559  
 0.55  
 0.542  
 0.533  
 0.525  
 0.516  
 0.507  
 0.498  
 0.489  
 0.48  
 0.47  
 0.461  
 0.451  
 0.441  
 0.431  
 0.42  
 0.409  
 0.398  
 0.386  
 0.375  
 0.363  
 0.35  
 0.338  
 0.325

WRITEPRN(stator) :=  $z_i(c)_1$

APPENDPRN(stator) :=  $z_i(c)_2$

APPENDPRN(stator) :=  $z_i(c)_3$

# APPENDIX C

## **Appendix C.1** **Dynamometer Code (FORTRAN)**

## DYNAMOMETER CODE

- C Program created on 8/18/93, by Edward J. Ognibene.  
C Last modified on 11/01/94, ".

```
real*8 Rmin,Rt,Rmaj,x,y,z,s,b,a,arg,l,pi,alpha,angle,g,dg,r
real*8 vv(1:2),hh(1:2),theta,R2,beta,nu,rho,mfrr,mfre,Atot
real*8 omega,c,cl,cIII,h,hII,hIII,AsI,AsII,AsIII,SA,t,tmp,Kgeo
real*8 Xo,Yo,Zo,dl,Lr,Ls,Ltot,NoB,sI,sII,sIII,chord,Af,bh,tmax
real*8 epsilon,E,f,fl,fII,fIII,Re,Dh,Pd,U,ratio,Pin,torque,ssl
real*8 rhos,AeI,AeII,AeIII,Ae,Qs,Vs,w,SolRot,SolStat,ReAve
```

- C Next is the eight dimensionless variables of interest

```
real*8 Sol,rR,hb,pf,k,ReMod,Pwr,fave
integer i,j,N,m
```

- C open(10, file='POWER.OUT')

```
pi = 3.141592654
nu = 0.290e-6
rho = 957.2
rhos = 0.59883825
```

- C Note: Kinematic viscosity and rho are in SI units, for 1 Atm, 100 C water.

```
write(*,*) 'enter torus major radius, Rmaj (in):'
read(*,*) Rmaj
write(*,*) 'enter torus minor radius, Rmin (in):'
read(*,*) Rmin
write(*,*) 'enter the machine rpm:'
read(*,*) omega
write(*,*) 'enter the blade heighth (in):'
read(*,*) h
write(*,*) 'enter the surface roughness (ft):'
read(*,*) epsilon
write(*,*) 'enter geometric k (else 0):'
read(*,*) Kgeo
```

```
bh = h
hb = h/Rmin
omega = omega*(2.0*pi/60.0)
U = (Rmaj/12.0)*omega
```

```
write(*,*) 'rotor blade tip speed = ',U,'(fps)'
```

```
U = 0.3048*U
epsilon = epsilon*0.3048
```

```
N = 100
```

- C write(10,\*) ' N = ',N

```
Rt = Rmaj - Rmin
```

```
C write(10,*) ' minor radius, Rmin = ',Rmin
C write(10,*) ' major radius, Rmaj = ',Rmaj
```

```
5 write(*,*) ''
write(*,*) '***** UPDATABLE PARAMETERS *****'
write(*,*) ''
write(*,*) 'enter the number of blades:'
read(*,*) NoB
tmax = 2.0*pi*(Rmaj-Rmin)/DBLE(NoB)
write(*,*) 'enter the average blade thickness (in):'
write(*,*) 'NOTE: This must be less than ',tmax,'(in)'
read(*,*) t
write(*,*) 'enter the recirculation factor, k:'
read(*,*) k
write(*,*) 'enter the percentage of fill (%):'
read(*,*) pf
```

```
pf = pf/100.0
```

```
ReAve = 0.0
```

```
if(Kgeo .eq. 0) Kgeo = k
```

```
alpha = datan(1.0/Kgeo)
```

```
write(*,*) ' alpha = ',alpha*180.0/pi,' deg'
```

```
h = pf*h
```

```
C Rotor side length calculation -----
```

```
Lr = 0.0
```

```
s = pi*Rmin
```

```
a = s/dsin(alpha)
```

```
b = a
```

```
l = a*dcos(alpha)
```

```
C write(*,*) ' l=',l
```

```
dg = pi/DBLE(N)
```

```
g = 0.0
```

```
x = 0.0
```

```
y = 0.0
```

```
z = a-l
```

```
C *** Transformation Block, cylindrical to toroidal, begins here *****
```

```
r = Rt + Rmin - y
```

```
angle = datan(z/Rt)
```

```
y = y + r*(1.0-dcos(angle))
```

```
z = r*dsin(angle)
```

```
c *** End of transformation block *****
```

```
PAUSE 'to continue --> press <enter>'
```

```
Xo = x
```

```
Yo = y
```

```
Zo = z
```

```

do 10 i = 1, N/2
 g = g + dg
 s = g*Rmin
 x = Rmin*(1.0-dcos(g))
 y = Rmin*dsin(g)
 z = ((a**2)*(1.0-(s/b)**2))**0.5
 z = z - 1
c *** Transformation Block, cylindrical to toroidal, begins here *****
 r = Rt + Rmin - y
 angle = datan(z/Rt)
 y = y + r*(1.0-dcos(angle))
 z = r*dsin(angle)
c *** End of transformation block *****
 dl = DSQRT((x-Xo)**2 + (y-Yo)**2 + (z-Zo)**2)
 Lr = Lr + dl
 Xo = x
 Yo = y
 Zo = z
10 continue

do 20 i = 1, N/2
 g = g + dg
 s = g*Rmin
 x = Rmin*(1.0-dcos(g))
 y = Rmin*dsin(g)
 z = ((a**2)*(1.0-(s/b)**2))**0.5
 z = z - 1
c *** Transformation Block, cylindrical to toroidal, begins here *****
 r = Rt + Rmin - y
 angle = datan(z/Rt)
 y = y + r*(1.0-dcos(angle))
 z = r*dsin(angle)
c *** End of transformation block *****
 if(i.eq.(N/2)-1) then
 vv(1) = y
 hh(1) = z
 end if
 if(i.eq.(N/2)) then
 vv(2) = y
 hh(2) = z
 theta = datan((hh(1)-hh(2)) / (vv(1)-vv(2)))
 end if
 dl = DSQRT((x-Xo)**2 + (y-Yo)**2 + (z-Zo)**2)
 Lr = Lr + dl
 Xo = x
 Yo = y
 Zo = z
20 continue

write(*,*) ' rotor blade length = ',Lr,'(in)'
theta = 180.0*theta/pi
write(*,*) ' rotor beta = ',theta,' deg'
C write(10,*) ' rotor beta = ',theta,' deg'

```

C -----

C Stator side length calculations:

```
Ls = 0.0
s = pi*Rmin
a = s/dsin(alpha)
b = s
dg = pi/DBLE(N)
g = 0.0
x = 0.0
y = 0.0
z = a*(1-dcos(alpha))
```

c \*\*\* Transformation Block, cylindrical to toroidal, begins here \*\*\*\*\*

```
r = Rmaj + y
angle = datan(z/Rt)
y = -y + r*(1.0-dcos(angle))
z = r*dsin(angle)
```

c \*\*\* End of transformation block \*\*\*\*\*

```
vv(1) = -y
hh(1) = z
```

```
beta = -datan(z/(-Rmaj-vv(1)))
beta = 180.0*beta/pi
```

PAUSE 'to continue --> press <enter>'

```
Xo = x
Yo = y
Zo = z
```

```
do 30 i = 1, N/2
 g = g + dg
 s = g*Rmin
 x = Rmin*(1.0-dcos(g))
 y = Rmin*dsin(g)
 z = a-((a**2)-(s-b)**2)**0.5
```

c \*\*\* Transformation Block, cylindrical to toroidal, begins here \*\*\*\*\*

```
r = Rmaj + y
angle = datan(z/Rt)
y = -y + r*(1.0-dcos(angle))
z = r*dsin(angle)
```

c \*\*\* End of transformation block \*\*\*\*\*

```
if(i.eq.1) then
 vv(2) = -y
 hh(2) = z
 theta = datan((hh(2)-hh(1)) / (vv(2)-vv(1)))
end if
dl = DSQRT((x-Xo)**2 + (y-Yo)**2 + (z-Zo)**2)
Ls = Ls + dl
Xo = x
Yo = y
Zo = z
```

30 continue

```

do 40 i = 1, N/2
 g = g + dg
 s = g*Rmin
 x = Rmin*(1.0-dcos(g))
 y = Rmin*dsin(g)
 z = a-((a**2)-(s-b)**2)**0.5
c *** Transformation Block, cylindrical to toroidal, begins here *****
 r = Rmaj + y
 angle = datan(z/Rt)
 y = -y + r*(1.0-dcos(angle))
 z = r*dsin(angle)
c *** End of transformation block *****
 dl = DSQRT((x-Xo)**2 + (y-Yo)**2 + (z-Zo)**2)
 Ls = Ls + dl
 Xo = x
 Yo = y
 Zo = z
40 continue

theta = 180.0*theta/pi

write(*,*) ' stator blade length = ',Ls,'(in)'
write(*,*) ' stator beta = ',-theta+beta,' deg'
C write(10,*) ' stator beta = ',-theta+beta,' deg'

write(*,*) 'done with stator'
write(*,*) ''

Ltot = Lr + Ls

write(*,*) ' total fluid path length = ',Ltot,'(in)'

SA=(4.0*Rmaj*Rmin*pi**2)+(DBLE(NoB)*Ltot)*(2.0*bh-t)
write(*,*) ' total available surface area ',SA,'(sq.in)'

C Convert SA to metric units.
SA = SA*6.4516e-4
write(*,*) ''

C-----
if(pf .lt. 0.01) tmp=pf
if(pf .lt. 0.01) pf=500.0
C-----

C Section I calculations: At the Hub

cI = 2.0*pi*(Rmaj-Rmin)
sI = (cI/DBLE(NoB)) - t
ssI = ((2.0*pi*(Rmaj-Rmin+h))/DBLE(NoB)) - t
Af = sI*h + 0.5*(ssI-sI)*h
AsI = 0.6653*Lr*(2.0*h+sI)
AeI = 0.6653*Lr*(2.0*pi*(Rmaj+h-Rmin) - DBLE(NoB)*t)

```



```

if(pf .eq. 500.0) Af = 0.0
if(pf .eq. 500.0) AsI = 0.0
if(pf .eq. 500.0) AeI = 0.0

write(*,*) 'spacing at hub = ',sI,'(in)'
write(*,*) 'section I wetted heighth = ',h,'(in)'
write(*,*) 'Incompressible flow area = ',DBLE(NoB)*Af,'(sq.in)'
write(*,*) 'section I surface area = ',DBLE(NoB)*AsI,'(sq.in)'
write(*,*) 'section I core area = ',AeI,' (sq.in) '

```

**C Conversion from English to SI units.**

```

h = 0.0254*h
Af = Af*6.4516e-4
sI = 0.0254*sI
AsI = AsI*6.4516e-4
AeI = AeI*6.4516e-4

```

```

Dh = 4.0*Af/(2.0*h+sI)
Re = k*U*Dh/nu

```

```

ReAve = ReAve + Re

```

```

if(pf .ne. 500.0) E = epsilon/Dh
if(pf .eq. 500.0) E = 0.0

```

```

write(*,*) ' E = ',E
write(*,*) ' Dh = ',Dh/0.0254,' (in) '
write(*,*) ' Re = ',Re
write(*,*) 'input moody (64/Re scale) friction factor, f:'
read(*,*) f

```

```

ratio = Re*(Dh/(2.0*((Rmin*0.0254)-(h/2.0))))**2.0
write(*,*) ' good if ',ratio,' is > 6?'

```

```

fI = f*(ratio**(1.0/20.0))

```

```

if(ratio .lt. 6) fI = f

```

```

write(*,*) ' The section I modified friction factor is ',fI*4.0

```

```

if(pf .ne. 500.0) h = h/(pf*0.0254)
if(pf .eq. 500.0) h = bh

```

```

C-----
write(*,*) ' '

```

```

C-----
C Section II calculations: At the Meridinal

```

```

cII = 2.0*pi*Rmaj
sII = (cII/DBLE(NoB)) - t
hII = pf*(Af/6.4516e-4)/sII
AsII = 0.3347*Ltot*(2.0*hII+sII)
AeII = 0.3347*Ltot*(2.0*pi*Rmaj - DBLE(NoB)*t)

```

```

if(pf .eq. 500.0) AsII = 0.0
if(pf .eq. 500.0) AeII = 0.0

write(*,*) 'spacing at meridian = ',sII,'(in)'
write(*,*) 'wetted heighth = ',hII,'(in)'
write(*,*) 'Incompressible flow area = ',DBLE(NoB)*Af,'(sq.m)'
write(*,*) 'section II surface area = ',DBLE(NoB)*AsII,'(sq.in)'
write(*,*) 'section II core area = ',AeII,'(sq.in) '

```

### C Conversion from English to SI units.

```

hII = 0.0254*hI
sII = 0.0254*sI
AsII = AsI*6.4516e-4
AeII = AeI*6.4516e-4

Dh = 4.0*Af/(2.0*hII+sII)
Re = k*U*Dh/nu

ReAve = ReAve + Re

if(pf .ne. 500.0) E = epsilon/Dh
if(pf .eq. 500.0) E = 0.0

write(*,*) ' E = ',E
write(*,*) ' Dh = ',Dh/0.0254,' (in) '
write(*,*) ' Re = ',Re
write(*,*) 'input moody (64/Re scale) friction factor, f:'
read(*,*) f

ratio = Re*(Dh/(2.0*((0.0254*Rmin)-(hII/2.0))))**2.0
write(*,*) ' good if ',ratio,' is > 6?'

fII = f*(ratio**(1.0/20.0))

if(ratio .lt. 6) fII = f

write(*,*) ' The section II modified friction factor is ',fII*4.0
write(*,*) ''

```

### C----- C Section III calculations: At the Outside

```

cIII = 2.0*pi*(Rmaj+Rmin)
sIII = (cIII/DBLE(NoB)) - t
hIII = pf*(Af/6.4516e-4)/sIII
AsIII = 0.6653*Ls*(2.0*hIII+sIII)
AeIII = 0.6653*Ls*(2.0*pi*(Rmaj+Rmin-hIII) - DBLE(NoB)*t)

if(pf .eq. 500.0) AsIII = 0.0
if(pf .eq. 500.0) AeIII = 0.0

write(*,*) 'spacing at outside = ',sIII,'(in)'
write(*,*) 'wetted heighth = ',hIII,'(in)'

```

```

write(*,*) 'Incompressible flow area = ',DBLE(NoB)*Af,'(sq.m)'
write(*,*) 'section III surface area = ',DBLE(NoB)*AsIII,'(sq.in)'
write(*,*) 'section III core area = ',AeIII,'(sq.in)'

```

### C Conversion from English to SI units.

```

sIII = 0.0254*sIII
hIII = 0.0254*hIII
AsIII = AsIII*6.4516e-4
AeIII = AeIII*6.4516e-4

```

```

Dh = 4.0*Af/(2.0*hIII+sIII)
Re = k*U*Dh/nu

```

```

ReAve = ReAve + Re

```

```

if(pf .ne. 500.0) E = epsilon/Dh
if(pf .eq. 500.0) E = 0.0

```

```

write(*,*) ' E = ',E
write(*,*) ' Dh = ',Dh/0.0254,' (in)'
write(*,*) ' Re = ',Re
write(*,*) 'input moody (64/Re scale) friction factor, f:'
read(*,*) f

```

```

ratio = Re*(Dh/(2.0*((0.0254*Rmin)-(hIII/2.0))))**2.0
write(*,*) ' good if ',ratio,' is > 6?'

```

```

fIII = f*(ratio**(1.0/20.0))

```

```

if(ratio .lt. 6) fIII = f

```

```

write(*,*) ' The section III modified friction factor is ',fIII*4.0

```

```

C-----
if(pf .eq. 500.0) pf=tmp
write(*,*) ' ***** pf = ',pf

```

```

C-----
ReAve = ReAve/3.0

```

```

Ae = AeI+AeII+AeIII

```

```

Atot = DBLE(NoB)*(AsI+AsII+AsIII)

```

```

write(*,*) 'Is the wetted surface area ',Atot,' < ',SA
write(*,*) 'If not, then there is a problem !!!'
write(*,*) 'Total wet surface area = ',Atot/6.4516e-4,'(sq.in)'
write(*,*) 'Total surf. area available is ',SA/6.4516e-4,'(sq.in)'
write(*,*) 'Total core surf. area = ',Ae/6.4516e-4,'(sq.in)'
write(*,*) 'The wet/useful ratio = ',Atot*100/SA,' %'
write(*,*) 'The avearge Re = ',ReAve
write(*,*) 'The recirculation velocity = ',k*U/0.3048,' (fps)'
pause 'enter to continue'
write(*,*) ''

```

```

C-----
SolRot = 2.0*(0.0254*Lr)/(sI+sII)
SolStat = 2.0*(0.0254*Ls)/(sII+sIII)
write(*,*) 'Rotor Solidity = ',SolRot
write(*,*) 'Stator Solidity = ',SolStat
write(*,*) ''

C-----
C Power Dissipation Calculations:

Pd = 0.5*rho*DBLE(NoB)*(fI*AsI+fII*AsII+fIII*AsIII)*(k*U)**3.0
C The power dissipation, Pd, is in watts.

write(*,*) 'The total power dissipation is ',Pd/1000.0,' (KW) '
C write(10,*) 'The total power dissipation is ',Pd/1000.0,' (KW) '
write(*,*) 'or P = ',Pd/745.7,' (hp) '
write(*,*) 'with a recirculation factor of ',k
write(*,*) 'Rotor speed, omega = ',60.0*omega/(2.0*pi),' (rpm) '
write(*,*) ''

C-----
C Torque and power input.

mfrr = DBLE(NoB)*rho*(k*U)*Af
torque = mfrr*U*Rmaj*0.0254
Pin = torque*omega

write(*,*) 'The recirculating mfr = ',mfrr,' (kg/s) '
write(*,*) 'or = ',(mfrr/rho)/6.30902e-5,' (gpm) '
write(*,*) ''
write(*,*) 'The torque input = ',torque,' (N-m) '
write(*,*) 'The total Power input = ',Pin/1000.0,' (KW) '
write(*,*) 'or Pin = ',Pin/745.7,' (hp) '
if(Pin .eq. 0.0)then
write(*,*) 'Pdiss/Pin = ',0.0
else
write(*,*) 'Pdiss/Pin = ',(Pd/Pin)*100.0,' % '
write(*,*) 'Averaged Power = ',(Pd+Pin)/(2.0*745.7),'(hp) '
end if
write(*,*) ''

C-----

mfre = Pd/2257e+3
Qs = mfre/rhos
if(Ae .eq. 0.0)then
Vs = 0.0
else
Vs = Qs/Ae
end if
write(*,*) 'Required mfr (evaporation) = ',mfre,' (kg/s) '
write(*,*) 'or = ',(mfre/rho)/6.30902e-5,' (gpm) '
write(*,*) 'Evaporation flow rate = ',Qs,' (cu.m/s) '
C write(*,*) 'or = ',Qs/6.30902e-5,' (gpm) '
write(*,*) 'or = ',2117.25312*Qs,' (cfm) '
write(*,*) 'Evaporation Velocity = ',Vs,' (m/s) '
write(*,*) 'or = ',Vs*3.28,' (fps) '

```

```

if(mfre .eq. 0.0)then
 write(*,*) 'Recirculation/evaporation mfr = (N.A.) '
else
 write(*,*) 'Recirculation/evaporation mfr = ',mfr/mfre
end if
pause 'enter to continue'

```

C-----  
C Dimensionless Parameters:

```

Sol = (2.0*pi*(Rmin*0.0254))/sII
rR = Rmin/Rmaj
ReMod = U*(Rmin*0.0254)/nu
Pwr = Pd/(rho*(Rmaj*0.0254)*(Rmin*0.0254)*(U**3.0))
fave = (fI+fII+fIII)/3.0

```

```

write(*,*) ''
write(*,*) ' Effec. Solidity = ',Sol
write(*,*) ' Radius Ratio = ',rR
write(*,*) ' Blade heighth* = ',hb
write(*,*) ' Fill level(hub) = ',pf
write(*,*) ' Recirc. Vel, k = ',k
write(*,*) ' Reynolds No.* = ',ReMod
write(*,*) ' Power Diss., P* = ',Pwr
write(*,*) ' Fric. factor, f = ',fave,'(64/Re Scale)'
write(*,*) ''

```

C-----  
write(\*,\*) 'enter 1 to go again, 0 to quit '  
read(\*,\*) m

```

Af = Af/6.4516e-4

```

```

if(m .eq. 1) goto 5

```

C close(10)  
stop 'program finished'  
end

## **Appendix C.2**

### **Sample Run**

```

C:\USERS\OGNIBENE\FORTRAN)
C:\USERS\OGNIBENE\FORTRAN)pwf
enter torus major radius, Rmaj (in):
2.5
enter torus minor radius, Rmin (in):
1.0
enter the machine rpm:
16000.0
enter the blade heighth (in):
0.6
enter the surface roughness (ft):
.00001
enter geometric k (else 0):
1.8
rotor blade tip speed = 349.065860112508100(fps)

***** UPDATABLE PARAMETERS *****

enter the number of blades:
16
enter the average blade thickness (in):
NOTE: This must be less than 5.890486389398575E-001(in)
.325
enter the recirculation factor, k:
1.25
enter the percentage of fill (%):
100.
alpha = 29.054603290559150 deg
to continue --> press (enter)

rotor blade length = 3.353020423624889(in)
rotor beta = 42.103251628160140 deg
to continue --> press (enter)

stator blade length = 3.589970266731827(in)
stator beta = 35.959618516268820 deg
done with stator

total fluid path length = 6.942990690356717(in)
total available surface area 195.897919168823000(sq.in)

spacing at hub = 2.640486389398575E-001(in)
section I wetted heighth = 6.000000000000000E-001(in)
Incompressible flow area = 3.665840320587158(sq.in)
section I surface area = 52.255164309268050(sq.in)
section I core area = 17.834269767108900 (sq.in)
E = 1.917004863721040E-004
Dh = 6.259765178705448E-001 (in)
Re = 7291654.927086434000000
input moody (64/Re scale) friction factor, f:
.015
good if 1457760.305254730000000 is > 6?
The section I modified friction factor is 1.219931811721250E-001

spacing at meridian = 6.567477315664292E-001(in)
wetted heighth = 3.488630550580328E-001(in)
Incompressible flow area = 2.365053455291339E-003(sq.m)
section II surface area = 50.360830676842190(sq.in)
section II core area = 24.418604692825200 (sq.in)
E = 1.773529152807695E-004
Dh = 6.766170307565909E-001 (in)

```

Re = 7881538.308897389000000  
input moody (64/Re scale) friction factor, f:  
.014  
good if 1323520.433595516000000 is > 6 ....?  
The section II modified friction factor is 1.133116489356224E-001

spacing at outside = 1.049446824193001(in)  
wetted height = 2.183197993027243E-001(in)  
Incompressible flow area = 2.365053455291339E-003(sq.m)  
section III surface area = 56.790073624546570(sq.in)  
section III core area = 36.827819790600780 (sq.in)  
E = 1.945860830468938E-004  
Dh = 6.166936558581139E-001 (in)  
Re = 7183523.991503315000000  
input moody (64/Re scale) friction factor, f:  
.0145  
good if 860631.029645964500000 is > 6 ....?  
The section III modified friction factor is 1.148600083662331E-001  
\*\*\*\* pf = 1.000000000000000  
Is the wetted surface area 1.028424154878785E-001 ( 1.263854969385028E-001  
If not, then there is a problem !!!  
Total wet surface area = 159.406068610656800(sq.in)  
Total surf. area available is 195.897919168823000(sq.in)  
Total core surf. area = 79.080694250534880 (sq.in)  
The wet/useful ratio = 81.372007057043900 %  
The average Re = 7452239.075829045000000  
The recirculation velocity = 436.332325140635100 (fps)  
enter to continue

Rotor Solidity = 7.282870634647005  
Stator Solidity = 4.208160499180500

The total power dissipation is 3378.213139591506000 (KW)  
or P = 4530.257589232278000 (hp)  
with a recirculation factor of 1.250000000000000  
Rotor speed, omega = 16000.000000000000000 (rpm)

The recirculating mfr = 301.075913713858800 (kg/s)  
or = 4985.530948212860000 (gpm)

The torque input = 2034.098953893178000 (N-m)  
The total Power input = 3408.165604294441000 (KW)  
or Pin = 4570.424498462017000 (hp)  
P<sub>diss</sub>/Pin = 99.121155830421090 %  
Averaged Power = 4550.341043847148000 (hp)

Required mfr (evaporation) = 1.496771439783565 (kg/s)  
or = 24.785112310691590 (gpm)  
Evaporation flow rate = 2.499458560834892 (cu.m/s)  
or = 5291.986570779552000 (cfm)  
Evaporation Velocity = 48.990068879929230 (m/s)  
or = 160.687424524550800 (fps)  
Recirculation/evaporation mfr = 201.150226221175600  
enter to continue

Effec. Solidity = 9.567121712074936  
Radius Ratio = 4.000000000000000E-001  
Blade height\* = 6.000000000000000E-001  
Fill level(hub) = 1.000000000000000  
Recirc. Vel, k = 1.250000000000000  
Reynolds No.\* = 9318758.412077542000000  
Power Diss., P\* = 1.816811581817136  
Fric. factor, f = 2.918040320616504E-002(64/Re Scale)

enter 1 to go again, 0 to quit  
0  
program finished

C:\USERS\OGNIBENE\FORTRAN>  
C:\USERS\OGNIBENE\FORTRAN>